Models for Fluid-Structure Interaction in Liquefied Natural Gas Sloshing

Bos, R.W.

DOI
10.4233/uuid:683c061b-056d-41bd-811a-69d061add709

Publication date
2022

Document Version
Final published version

Citation (APA)
Bos, R. W. (2022). *Models for Fluid-Structure Interaction in Liquefied Natural Gas Sloshing*. [Dissertation (TU Delft), Delft University of Technology]. https://doi.org/10.4233/uuid:683c061b-056d-41bd-811a-69d061add709

Models for Fluid-Structure Interaction in Liquefied Natural Gas Sloshing

Proefschrift

ter verkrijging van de graad van doctor
aan de Technische Universiteit Delft,
op gezag van de Rector Magnificus prof. dr. ir. T.H.J.J. van der Hagen,
voorzitter van het College voor Promoties,
in het openbaar te verdedigen op woensdag 29 juni 2022 om 10 uur.

door

Reinier Walewein BOS

scheepsbouwkundig ingenieur,
Technische Universiteit Delft,
geboren te Spijkenisse, Nederland

Dit proefschrift is goedgekeurd door de promotoren.

Samenstelling promotiecommissie bestaat uit:

Rector magnificus	Voorzitter
Prof. dr. ir. M.L. Kaminski	Technische Universiteit Delft, promotor
Dr. ir. J.H. den Besten	Technische Universiteit Delft, copromotor
Dr. ir. P.R. Wellens	Technische Universiteit Delft, copromotor

Onafhankelijke leden:

Prof.dr. F. Dias	U. College Dublin, Ierland / ENSPS, Frankrijk
Prof.dr.ir. A.V. Metrikine	Technische Universiteit Delft
Prof.dr.ir. R.H.M. Huijsmans	Technische Universiteit Delft
Dr.ir. A.S. Tijsseling	Technische Universiteit Eindhoven
Prof.dr.ir. B.J. Boersma	Technische Universiteit Delft, Reservelid

This work is part of the research programme 'SLING' with project number P14-10 which is (partly) financed by the Netherlands Organisation for Scientific Research (NWO).

Druk: Ridderprint, www.ridderprint.nl
Omslag: 'Golven voor papa' door V.M. Bos, K.J. Bos; Stoepkrijt op Beton
Gemaakt met LaTeX

ISBN 978-94-6458-365-6
Electronic version of this dissertation is available at the TU Delft repository.

Contents

Preface

This thesis was written out of curiosity of the author for the subject of fluid-structure interaction. A curiosity that was shared by the project partners, in order to improve design, and colleagues at the university, to better understand fundamentals. The work in this thesis reflect these interests.

During the writing of this thesis the world changed, both big and small. Small things became big, and some big things again small. Things changed, then things unchanged.

And so it happened to this thesis. A small idea leads to many questions, all wanting to be answered, but only a few can be answered in time. I hope the reader can appreciate this compiled work, which reflects four years of research. And then almost two years of 'just finishing the last things'.

Abstract

The energy transition requires the maritime industry to shift to a different fuel. A long term solution is liquefied hydrogen, but there are many challenges to get there. On the short term liquefied natural gas (LNG) might be the most feasible option, because its use relies mostly on existing technologies. It is however not straighforward to take the design of an LNG tank used for cargo and implement it on a containership. The tank is not just a hold in the ship, but it is insulated with a specific cargo containment system (CCS). A CCS is typically made up of many layers, metal membranes to keep the LNG in, foam to provide insulation and plywood layers to provide enough strength.

When the cargo tanks are scaled to meet the size requirements of a fuel tank, the fluid will behave differently and physics of load and response inside the tank scale as well. This means that with scaling the dominant loading mechanism on the tank walls changes. Simply scaling the CCS along with the hold dimensions is therefore not a safe choice. The current strength assessment of the tanks uses tuning factors that are based on experience with a specific size of LNG tanks. Most uncertainty in scaling is about the validity of the method considering variablity of the impact, phase transition and fluid-structure interaction (FSI).

This thesis focusses on the fluid structure interaction of the CCS with the liquid within the cargo tank, both from a fundamental perspective and by looking at the wave impact on the tank walls.

The fundamental look on FSI was done by looking at wave impacts on a pendulum, which hangs close to the free surface of the towing tank. This is a straightforward and reproducible experiment for validation of FSI codes with a free surface, as well as general insight into the problem. One can think of the pendulum as a structural member which shows quite some deformation in interaction with a wave.

The properties of the pendulum are known, and waves with known periods are generated. At first the pendulum is dry, then the first waves start to excite it. The behaviour of the pendulum depends highly on whether the wave period is higher or lower than the dry natural period of the pendulum. A reduced order model was set up using a single degree of freedom pendulum with the Morison

equation. In order to account for the pendulum going from dry to wet and back, a wetness model is developed and presented. Good agreement was found between the experiment and the reduced order model. Furthermore, it was found with the experiment and model that the variability of the pendulum response is in all cases larger than the variability of the wave height.

The experimental setup was reused with a focussed wave instead of periodic waves. Here there was significant spread in pendulum response between different repetitions of the same wave, especially when there was aeration. Again it was found that the variability in the response is larger than in the wave that excites the pendulum. The reduced order model was updated, using wave components from a Fourier expansion of the wave height around the time of impact. Representative results were found using the same parameters as for the monochromatic wave without tuning.

Seeing how sensitive the fluid-structure interaction is to the variation of parameters is an encouragement to build low fidelity models for the fluid and structure, that can be used to screen the design space for interesting interactions. While current state of the art methods result in safe designs of LNG tanks, they are typically time consuming. Low fidelity methods could be more accessible to designers and developers of statistical models.

The first reduced order model is for the structure, the cargo containment system. In this model a 2D crossection of the CCS is modelled as composite structure, namely a beam on an elastic foundation. The model is tuned by choosing a displacement field over the height of the foam, in this case it is chosen so that it matches the first vibration mode of the CCS. By assuming that the beam on top is an Euler beam, the other vibration modes can be found as well. A finite element model was set up as a reference to validate the reduced order model under a number of artificial static loads as well as a measured impact load. Even though the level of detail over the height of the foam is limited, it turns out that it is sufficiently accurate to yield conservative results for stress in the CCS compared to the reference solution.

The reduced order model was extended to investigate the effect of loads that were applied slightly at an angle with respect to the 2D section. All natural frequencies of the reduced order plate foundation model were within 10% of the finite element solution. First it was noted that the effect of taking a perfectly aligned load or a load with a slope is not important for the maximum indentation for the plate. For the stresses, however, the angle does matter, causing for one case almost twice the stress in one case. Also point loads were investigated, at a number of different locations. Here the placement of the load can give a factor two difference in stress. For gaining understanding of the problem a 2D model is enough, but in order to come up with representative results a 3D model should be used.

Finally a model for the wave impact onto a wall is set up. The fluid is modelled as

a jet with a certain shape and velocity that impacts on the wall. By assuming a displacement field over the height of the jet a set of equations for the fluid flow and force on the wall is obtained. This model, compared to a high fidelity fluid solver and coupled to a structure model, predicts well the added mass experienced by the CCS and the total impact. The maximum impact force is not well predicted, likely due to the lack of resolution in the height of the fluid.

What is interesting is that both from the reduced order model and from the high fidelity fluid solver there is no clear trend for which cases FSI is important. It seems to have a lot to do with the time distributions of load and response and, therefore, it is expected that for each case FSI has to be taken into account separately, in order to be confident about the result.

Samenvatting

Om de energietransitie mogelijk te maken moet de maritieme industrie naar een andere brandstof overstappen. Een lange termijn oplossing is vloeibaar waterstof, maar er zijn nog veel uitdagingen om daartoe te komen. Op korte termijn is vloeibaar aardgas (LNG) mogelijk een haalbare optie, omdat het gebruik ervan mogelijk is met bestaande technologie. Het is echter niet eenvoudig om het ontwerp van een LNG ladingtank te pakken en het te gebruiken op een containerschip. De tank is een ruim in het schip, geïsoleerd met een specifiek ladingsysteem (CCS). Een CCS bestaat uit verschillende lagen, namelijk membranen van metaal om het LNG binnen te houden, schuim om de lading te isoleren en multiplex om voor genoeg sterkte te zorgen.

Als een ladingtank verschaald wordt naar de afmetingen van een brandstoftank, dan betekent dit dat de fysica van de belastingen en responsie ook verschalen. Dit betekent dat met verschaling ook het dominante belastingsmechanisme op de tankwanden verandert. Eenvoudigweg schalen van het CCS met de afmetingen van het ruim is dus geen veilige keus. De huidige methode om de sterkte van de tanks te analyseren gebruikt verschillende kalibratiefactoren die gebaseerd zijn op ervaring met een specifiek formaat LNG tanks. De grootste onzekerheid in de schaling zit in de validiteit van de schalingsmethode als het gaat om variabiliteit van de golfklap, fase overgang en interactie tussen vloeistof en constructie (FSI).

Deze thesis draait om de interactie tussen de vloeistof en constructie van inhoud van de tank met de tankwanden, zowel uit fundamenteel opzicht als door concreet te kijken naar een golfklap op de tankwand.

Een simpeler geval van FSI is een golfklap tegen een slinger die vlak boven het water van de sleeptank hangt. Dit is een eenvoudig en reproduceerbaar experiment voor de validatie van FSI codes met een vrij vloeistofoppervlak en geeft algemeen inzicht in dit soort problemen. Men kan de slinger voorstellen als een constructiedeel die veel vervormt tijdens de interactie met de golf.

De eigenschappen van de slinger zijn bekend en golven met een bekende periode worden gegenereerd. Eerst is de slinger droog, dan brengt de eerste golf hem in beweging. Het gedrag van de slinger hangt voor een groot deel af van de golfperiode, of deze langer of korter is dan de slingertijd van de droge slinger. Een

vereenvoudigd model is opgesteld door een slinger met een vrijheidsgraad te combineren met de Morison vergelijking. Om rekening te houden met de slinger die nat en droog wordt, is er een 'natheid' model opgesteld. Er is goede overeenkomst gevonden tussen de experimenten en het vereenvoudigde model. Verder is zowel met het experiment en het model gevonden dat de uitslag van de slinger een grotere variabiliteit heeft dan de variabiliteit van de golfhoogte.

De experimentele opstelling is opnieuw gebruikt, maar nu met gefocuste golven in plaats van periodieke golven. Er was een significante spreiding in uitslag van de slinger voor de verschillende herhalingen van dezelfde golf, zeker als er lucht in de golf zat. Ook hier bleek dat de variabiliteit in de uitslag van de slinger groter is dan in de hoogte van de golf die de slinger aanslaat. Het vereenvoudigde model is verbeterd met een Fourierreeks van de golfhoogte vlak voor de golfklap. Met dit model zijn representatieve resultaten gevonden, zonder de parameters te wijzigen ten opzichte van het vorige experiment.

De gevoeligheid van FSI voor de variatie van parameters was een aanmoediging om een vereenvoudigd model voor zowel de constructie als de golf te maken, die gebruikt kan worden om in de ontwerpruimte naar interessante interacties te zoeken. Moderne nauwkeurige rekenmethodes zorgen voor veilige LNG tanks, maar kosten veel tijd. Vereenvoudigde modellen kunnen dan toegankelijker zijn voor ontwerpers en ontwikkelaars van statistische modellen.

Het eerste vereenvoudigde model is dat van de constructie, namelijk het ladingsysteem. In dit model wordt een 2D doorsnede van het CCS gemodelleerd als een samengestelde constructie, namelijk een balk op een elastische ondersteuning. Het model gebruikt het verplaatsingsveld van de eerste trilvorm over de hoogte van het schuim. Door aan te nemen dat de ondersteuning meebeweegt met de balk, kunnen de andere trilvormen bepaald worden. Een eindige elementen model is gebruikt als referentie om het vereenvoudigde model mee te valideren, voor een aantal kunstmatige ladingcondities alsmede een gemeten dynamische golfklap. Het model is nauwkeurig genoeg om spanningen in het CCS conservatief te berekenen, ook al worden veel details niet meegenomen.

Het vereenvoudigde model is uitgebreid om belastingen die scheef zijn aangebracht te beoordelen, in vergelijking met het 2D model. Alle eigenfrequenties van het vereenvoudigde model zijn binnen 10% van de eindige elementen oplossing. Als eerste wordt opgemerkt dat het effect van een scheve belasting niet zorgt voor een grotere indrukking van het ladingsysteem. Voor de spanningen is de hoek waaronder de belasting wordt aangebracht wel van belang, in een geval geeft dit zelfs een factor twee hogere spanning. Ook geconcentreerde belastingen op verschillende locaties zijn onderzocht. De locatie van de geconcentreerde belasting kan ook een factor twee in spanning uitmaken. Om de aard van het probleem te begrijpen is het 2D model goed genoeg, maar voor representatieve resultaten moet men een 3D model gebruiken.

Als laatste is er een model gemaakt voor een golfklap op een wand. De vloeistof is gemodelleerd als een straal met een bepaalde doorsnede en snelheid, die tegen de wand aankomt. Een set vergelijkingen voor de stroming en kracht op de wand kan worden opgesteld door een verplaatsingsveld aan te nemen over de hoogte van de straal. Dit model, wat vergeleken wordt met een gedetailleerdere methode en gekoppeld met de constructie, is goed in staat om de toegevoegde massa en totale kracht van de golfklap te voorspellen. De maximale kracht wordt minder goed voorspeld, waarschijnlijk doordat er een verplaatsingsveld over de hoogte van de straal wordt aangenomen.

Het interessante is dat de koppeling van beide vereenvoudigde modellen en de gedetailleerde methode geen duidelijke trend laten zien voor wanneer FSI belangrijk is. Factoren die belangrijk zijn, zijn hoe de belasting en responsie veranderen in de tijd. De verwachting is dat voor elk individueel geval van een golfklap FSI bekeken moet worden, zodat men zeker kan zijn van de resultaten.

Chapter 1

Introduction

Energy storage and transportation is one of the key challenges in tackling climate change and enabling renewable resources. Ideally one would have an offshore wind park on the windiest location, but that might not be where most energy is consumed. Within countries energy is transported with electricity lines, but what about intercontinental energy transport, or getting energy to remote villages? Liquified Natural Gas (LNG) is a short term viable energy carrier, a role liquefied hydrogen can fulfill in the future.

It is also expected that ships with a high energy demand and few possibilities for recharging will not electrify any time soon. Here a short term solution could as well be LNG, as a fuel. This comes with its own challenges, although LNG is currently safely transported on board of LNG carriers. Fuel tanks are usually smaller than cargo tanks and have a different shape. Therefore different physics are responsible for the most extreme loads. One effect that comes into play for extreme loads is fluid-structure interaction, when the load and response are so tightly coupled that they must be considered jointly.

This thesis is a collection of papers, which report my research on the importance of fluid-structure interaction for sloshing in an LNG tank. The context of this thesis is given below, starting with wave impacts, then going to structural response and tying it together with the interaction between them. Finally, the research goal and outline of this thesis are given.

1.1 Wave loads

Ship and offshore structures are constantly loaded by a variety of loads, as for instance explained in [50, 76]. The ship structure and cargo are exposed to gravity. At the same time the ship displaces water, causing pressure variations along the plates of the hull, which load the stiffeners, progressing through the ship structure.

When the structure operates in waves the pressure changes constantly, inducing

bending moments over the hull. On a local level this means that parts of a ship that are normally dry are now wet, or vice versa. In larger waves the ship might dive into a crest and get water on deck, or it might exit the water and slam into the next wave. No two waves are the same, they are irregular, which makes the exact load experienced by the ship time dependent and stochastic.

Irregular waves can be seen as an addition of many regular components [77], interacting with each other if the resulting wave is sufficiently steep. For regular waves there are criteria when the wave starts to break based on the steepness of the wave. However, for irregular waves this is harder to determine, and this process is sensitive to initial disturbances in the fluid. Because these disturbances are not easily quantified, one generally turns to statistics to take stochastic effects into account.

LNG tankers carry liquid cargo and due to wave induced motion of the ship, the cargo moves as well. Waves form in the tank, and for some filling levels and excitation frequencies these waves can be such that they damage the tank insulation. For this reason the filling height of the tank is regulated by rules of the classification society [18].

The aforementioned shows that wave impacts take place on the outside and on the inside of a ship, and that they are hard to predict. Wave impact problems can be simplified by breaking them down in a number of subproblems, see for instance [59], or for slamming in [27].

Figure 1.1 shows an overview of stages of wave impacts as given in [13, 14]. The pendulum is seen as a simplified structure that interacts with the wave. Four phases are distinguished when the wave hits a structure:

1. Water entry: the wetted area increases
2. Wet vibration: the structure is submerged and vibrates
3. Water exit: the wetted area decreases
4. Dry vibration: only the structure vibrates

When the structure is wetted a body of water moves along with the structure. The surrounding water adds mass, but energy also goes away through the water. This is called added mass and added damping, because it is only there when the structure is submerged. Added mass and damping are reasonably well defined when the structure is submerged, but not during water entry and exit, because the wetted surface changes all the time.
Compare this to [33], which mentions phase 1 and 2 as structural inertia phase and free vibration phase respectively. In [33] is mentioned that pressure 'details' during the structural inertia phase are not important for the maximum response, but that total impulse is.

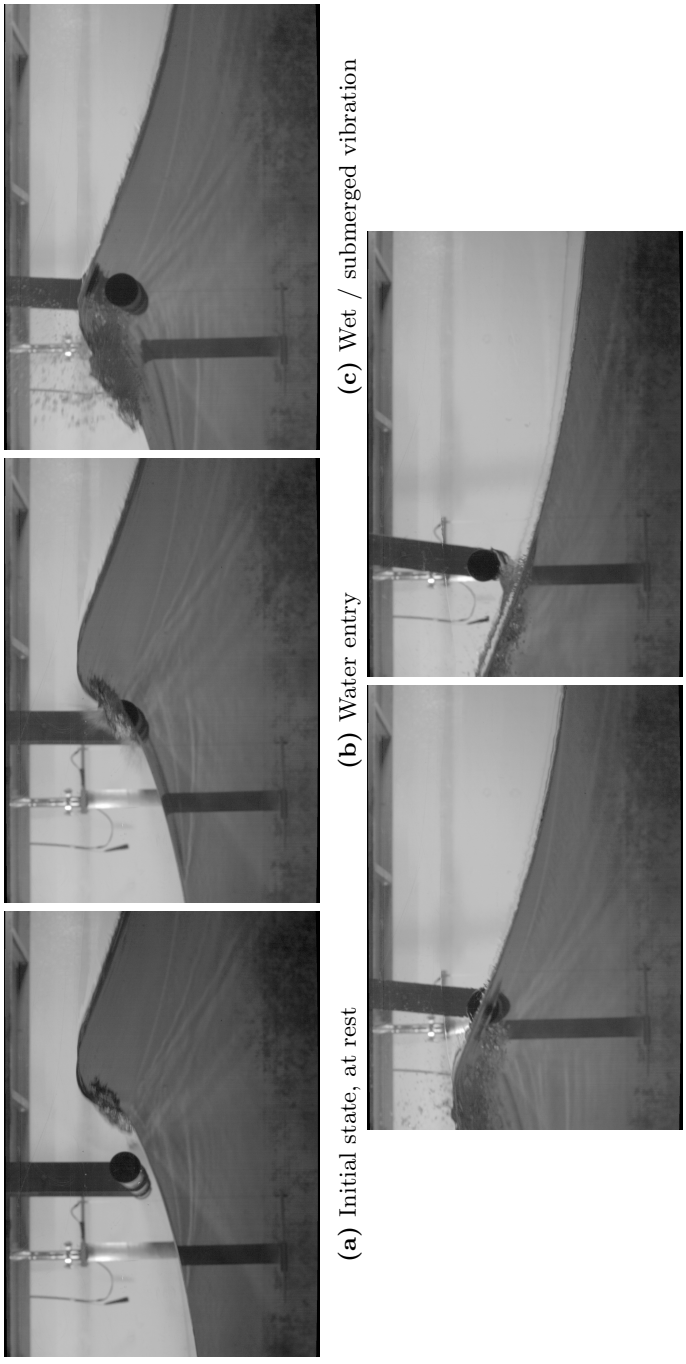

(a) Initial state, at rest **(b)** Water entry **(c)** Wet / submerged vibration

(d) Water exit **(e)** Free vibration

Figure 1.1: Initial state and four impact phases, from [14]. The pendulum represents a maritime structure interacting with waves.

Wave impacts for the LNG CCS are investigated in, for instance, the Sloshel project [16, 8]. The waves are generated in a flume such that an especially large wave is created at a certain distance in front of the wall. Of course, this is an idealization, especially created to make repeatable wave impacts of different nature. Even these controlled focused waves have a random component due to motion that is already in the water, or instabilities that grow in a random way. Looking at the wave impacts, some distinct loading phenomena were identified, called Elementary Loading Processes (ELP) [59]:

1. Direct impact
2. Building jet
3. Pulsating gas pocket

The magnitude of an ELP depends on the shape of the wave [59]. As mentioned before, LNG and liquid hydrogen are seen as fuels that could make the shipping industry more sustainable. When a different tank size or design is chosen, then the ELP's are likely to change as well. However, because all the ELP's depend on different physical phenomena and quantities, simply scaling a tank to a new size is likely to make another ELP dominant. This makes design of tanks of a completely different size challenging.

1.2 Ships and wave impacts

Traditional ship and offshore structures are made of steel, mostly plates reinforced with stiffeners, decks and girders. The mass, stiffness and strength of the ship are not homogeneous, being stiff at one point due to a stiffener and more compliant at another point where the plate is not supported. On average, the density of the ship is less than that of the surrouding water. Steel is an attractive material because it is easy to form and weld without a clean room or highly educated workers. Also it gives plenty of reserve strength after yield and can accommodate large strains before it ruptures, maintaining water tightness. The topology of the ship causes a large range of vibration frequencies to which the ship will react.

The important thing about breaking waves is that they should not damage the structure. There are different kinds of ships subject to wave impacts, such as:

- Conventional monohull ships, experiencing water on deck (green water)
- Multihull ships, where wave impacts between the hulls cause large loads
- Ships carrying liquid cargo, which can slosh inside the tank

Ship motions have typical periods in the order of of seconds, global bending tenths of seconds and local vibrations hundreths of seconds or even less. The exact pressure distribution is not important according to [33], at least not for steel and

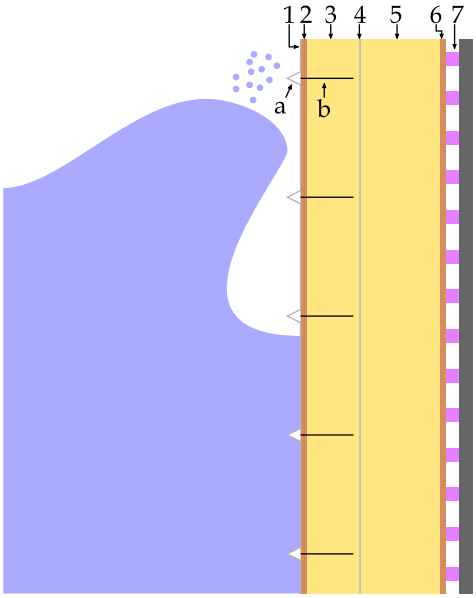

Figure 1.2: Sketch of the Mark III CCS designed by GTT.

aluminum structures. Only the total force impulse matters and the maximum strain is experienced during the free (wet) vibration phase. It is however not expected that this statement will hold in all cases, for instance if there is large motion during the impact.

As mentioned before, a way to reduce the environmental footprint of global transport is to use LNG or liquefied hydrogen as fuel. LNG is transported at atmospheric pressure at -162°C, the temperature at which LNG is a boiling liquid. A disadvantage of steel is that it becomes brittle at such temperatures, as a result of which additional insulation for liquefied natural gas (LNG) tankers is required. LNG tanks are therefore lined with a cargo containment system (CCS). The main goal of the CCS is to prevent heat transfer towards the steel and also to avoid losing cargo due to boiling off. Additionally, it keeps the LNG and boiled-off natural gas (NG) inside the tank by being gas and liquid tight. In this thesis the Mark III CCS designed by GTT is investigated because it is a commonly used CCS, see Figure 1.2 for a sketch.
The Mark III CCS is a sandwich structure made up of the following layers, from top (LNG side) to bottom (ship side) [49].

1. The primary barrier, a stainless steel membrane of 1.2 mm thick which is gas and liquid tight

2. Top plywood of 12 mm thick

3. Top layer of the foam, approximately 100 mm thick

4. The secondary barrier, which is liquid tight redundancy to the primary membrane
5. Bottom layer of foam, approximately 170 mm thick
6. Bottom plywood of 9 mm thick
7. Mastic ropes, running from the bottom of the tank to the top of the tank, of approximately 20 by 20 mm spaced 93 mm, exact dimensions differ per project.

The tank is constructed at room temperature, but the cryogenic cargo causes thermal strains. To avoid thermal strains from inducing large stresses two measures are taken. First, the primary barrier has corrugations, see *a* in Figure 1.2, that are partly stretched out when cooled down. Second, the top plywood and first foam layer are cut every 340 mm (in both directions) to create a stress relaxation groove, see *b* in Figure 1.2. The aforementioned corrugations are directly above the relaxation grooves, as shown in Figure 1.2. In [11] these repeating units of 340 by 340 mm are called subpanels. These units are mostly independent of each other, due to only being connected at the secondary barrier, bottom foam and plywood. The ship structure connects all the structural elements to each other.

From composites engineering the failure modes of such structures are known, such an overview can be found for instance in [19]. The CCS is loaded mostly in the out of plane direction, and due to the support and relaxation grooves will not be loaded in global bending. Two failure modes are commonly investigated for the Mark III CCS. First the crushing of the foam, second is shearing of the bottom plywood [49]. The idea is that if one of these failure modes is reached, the support of the primary membrane decreases to the level that it will not fail before the next inspection, but soon thereafter.

There are additional modes investigated, for instance plastic deformation of the corrugations of the primary membrane. During inspections of the tank these damages are visible, and indicate that a violent wave impacted on the structure. While not negatively influencing the safety of the tanks, these damages are used to tune the safety factors of CCS design [40].

The industry standard to predict failure of the CCS is to perform highly detailed FE analysis for a number of selected cases [26, 40, 18]. The focus is on the behavior of the foam, for which specialized non-linear materials are used [49, 25]. The foam first behaves elastically, then has a plateau in which it is crushed, before it stiffens again. However, these material models are isotropic as opposed to reality which is orthotropic due to the fibers which are only introduced in the in-plane direction. This can be modelled with advanced failure criteria [51].

Modeling the plywood is also a challenge, because it consists of many layers of wood glued on top of each other. Each layer has an orientation and is in some way heterogeneous. According to rules this can be simplified to a shell with isotropic

properties [26]. Another simplification is the general use of static calculations together with dynamic amplification factors [81].

A final difficulty are the stress concentrations due to the mastic ropes and relaxation grooves. There are singularities in the stress, which are by definition amplified if the mesh is refined. However, from in real life the structure does not fail there, and these stress concentrations can be disregarded. Another singularity is found at the edge of the foam, where the foam meets the top plywood.

Structures impacted by LNG sloshing are much lighter and have higher natural frequencies than 'traditional' steel ship and offshore structures. Also there are no local or global stiffeners, instead the structure rests on the ship inner hull. The strength comes, for the Mark III CCS from the foam and plywood, which can be regarded as a sandwich structure. This structure is optimized for insulation, to prevent the LNG from boiling off as much as possible. In order to do so the lightest insulation is most beneficial (it has lowest thermal conductivity). However, the light insulation has generally low strength and low stiffness, making the CCS vulnerable to failure due to violent wave loads.

1.3 Fluid-structure interaction and wave impacts

Most analysis of maritime structures involves two steps: first the load is predicted, then the response to these loads is determined. This is called one-way coupling, because the information travels only one way: from load to response. For extreme load cases the interaction between the fluid and structure is important in determining the final response of the structure. For instance, the rate with which the force of a water wedge impact increases in time is to the third power of the velocity [107]. A small change in relative velocity due to the structural motion can therefore have a large effect on the force and therefore response. This is called two-way coupling, because the information goes back and forth between load and response.

Three types of impact problems for which FSI is considered exist in maritime engineering, and they are all closely related. The first is green water, when water comes on deck due to large ship motions and large waves, and the water on deck subsequently hits a structure on deck. The second is slamming, when a ship comes out of the water and enters again with an impact. Third is sloshing, where a content of a tank forms breaking waves. Some of these problems are considered with two-way coupling: the characteristic time of the loading is close to the response period, for instance the rise time is close to the natural period. It also shows that the appropriate part of the structure should be chosen to respond to the loads.

What makes these problems unique compared to FSI problems in other fields, such as aerospace engineering or water hammer, is that it involves a free surface that changes in time. This means the structure is not fully submerged all the time, but 'wetness' is a function of time. For instance, if the bow of a ship comes out

of the water and then enters again there is a fast transition from dry to wet. This complicates the definition of added mass or damping, because those are closely tied to wetted area. Also, the fluid is relatively heavy, the mean density of the fluid and structure are the same (otherwise it would not float). This density ratio is important for the coupling scheme that can be used in numerical treatment of FSI. Which method is most suitable depends on a combination of factors, to be considered for each individual problem.

There are also commonalities between the different fields in which FSI is applied an the maritime application of FSI. For example large motions and the resulting grid deformations, such as encountered during slamming of small boats.

Another difficulty for FSI in the maritime environment is validation. Individual parts of FSI have been validated, such as wedge water entry or submerged behavior, but there are few experiments that have all impact phases and are straightforward to reproduce, or make numerical and analytical models for. Validation is important because the mathematical or numerical model that is used has inherent assumptions that change the kind of response one will get. Physics that is not known will not be observed, even though it might be important.

The benefits of taking FSI into account, or knowing when to take it into account can be reflected in safety margins. The size of safety margins reflects the degree of uncertainty, meaning if one is more certain about the structural stress in extreme cases, a more cost-efficient design can be made.

1.4 Research goal

The central problem in this thesis is sloshing in an LNG tank. Imagine a ship with several cargo tanks in its hold, all partially filled. The ship sails through calm and rough seas, and the ship moves in response of the wave forces. Because the cargo tanks are neither full nor empty, waves form on the free liquid surface. When the tank is excited at certain frequencies these waves become large enough that they will break on the CCS. This is called sloshing. Sloshing is one of the limiting load cases for the design of LNG tanks and tankers.

LNG tanks and the CCS are designed to withstand sloshing. The ship motions and response in the tank are stochastic and generally sensitive to input parameters such as exact fluid height and pre-existing perturbations of the free surface. This stochastic nature is taken into account by performing model tests, usually on a 1:40 scale, evaluating every tank design and filling height for the various sea states it might encounter. Instead of LNG water is used, with a heavy ullage gas that ensures the similarity in density ratio between gas and liquid. Such model tests are time consuming and raise many questions, related to two main points.

The first point is that not all physics scales in the same way, and by enforcing geometric similarity and Froude scaling other physics is not well scaled:

- Surface tension
- Gas and liquid compressibility
- Mass and stiffness of the structure
- Instabilities of the fluid
- Phase change

The second point is that extreme events are rare, and extrapolating extreme events is not straightforward. This means that even though many impacts are observed in the model tests and in real life, it could still be that the most critical one is not there. Hence, the fact that no two impacts are the same, which is related also to the scaling, causes additional challenges.

In the state of the art scaling and experience with incidents of the CCS are combined to yield a conservative assessment [40]. The results of the model tests are taken as basis, then calibrated to agree with the experience gained during operations with vessels. However, this works only when the new designs are similar to the existing designs. As mentioned before, it is currently not allowed to sail with half full tanks, to avoid the potentially severe consequences of sloshing. In the future, LNG will be used as fuel and then it will be necessary to allow intermediate filling levels. Also the tanks could have different sizes or shapes. This means the calibration procedure used now might not be valid anymore. Therefore the industry wants to move towards a first principle approach.

In the first principle approach the understanding of the physics is such that the designer knows which physics to take into account. Of similar importance is to know how the different aspects of sloshing scale, so that model tests can be better interpreted. The SLING programme has aimed to further the knowledge about the first principles, such that this approach can be used in the design of LNG tanks. Within SLING three points are investigated:

1. Phase change in an impact
2. Variability of the flow and impact pressure
3. Fluid-structure interaction

And within this thesis the focus is on fluid-structure interaction between the LNG and CCS. The approach in the industry is to create increasingly detailed models and model tests in order to better understand the behavior in specific situations. This is valuable when the critical load cases are know, such as in series of similar tanks, but fails when new designs at other scales or for other boiling liquids are considered. Hence, the leading thought in this thesis is to provide tools, thought experiments and models for the designer to understand and apply principles of fluid-structure interaction in the design of the CCS. With these tools the following question can be answered: *In which cases does Fluid-Structure Interaction*

influence failure of an LNG CCS due to wave impacts?

Ideally the results of this thesis would be implemented in a screening method, in which a large number of load cases are investigated using low fidelity methods, as shown in Figure 1.3. The drawn line is how a structure would respond to for instance different wave shapes. It is however not possible to make an exact solution, so some kind of approximation has to be made. The approximation is done by a low fidelity method, that samples almost all the possible wave shapes. The most critical cases are then selected for investigation with a detailed FE / CFD code, or model tests. Additionally, for the model tests, the low fidelity methods presented in this thesis indicate where in space and time the critical loads or stresses occur, guiding the use of the right pressure sensors and strain gauges.

1.5 Outline

This thesis is made up of five chapters, based on five papers, and one chapter with conclusions and recommendations. The first two chapters investigate FSI on a fundamental level through a series of experiments. In these experiments a pendulum suspended above the mean water surface in a towing tank is subject to the action of monochromatic and focussed waves. The experimental results are compared to a simplified model for fluid, structure and the interaction. With the results numerical models can be validated. Also, it provides insight into which parts of the four phases of FSI are important in this wave impact scenario.

The third chapter is a 2D reduced order model (ROM) for the CCS, which uses the first vibration mode over the height of the foam to predict the other vibration modes. The ROM is compared to FEM models with satisfactory results for both static and dynamic loading. The next chapter shows what the effect is of a load that applied at a slight angle. In those cases the 2D assumption does no longer hold, so a 3D model is used.

The fourth and final chapter presents a ROM for the interaction between a wave impact and the CCS. Here the ROM of the third paper is used for the structure and a new model for the impact is used. The results are compared to an in-house developed code giving a detailed prediction of the wave hitting the wall.

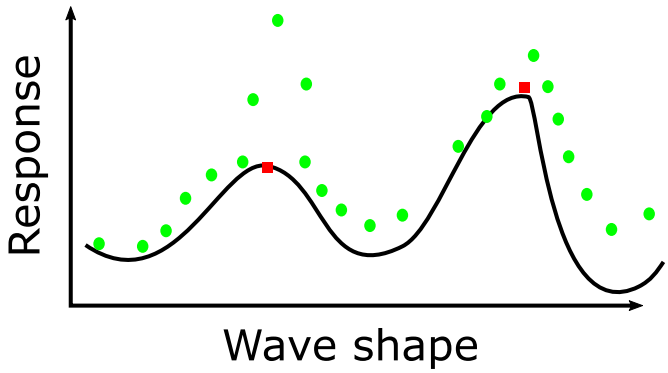

Figure 1.3: Sketch of a possible implementation of the tools developed in this thesis. First sample many points with low fidelity (green dots) in order to find the cases in which the CCS is critically loaded. Then use a high fidelity solver to investigate the most critical points (red squares). The continuous line is the actual value of the quantity of interest, but is not feasible to directly calculate.

Chapter 2

Fluid Structure Interaction Between a Pendulum and Monochromatic Waves

Based on R.W. Bos, P.R. Wellens. 'Fluid-structure interaction between a pendulum and monochromatic waves' (2021) Journal of Fluids and Structures, 100, art. no. 103191.

Ships and offshore structures are subject to waves, and being able to predict how the structure responds is important for safety and efficiency. A ship operates in the interface between water and air and undergoes motion as a result of the interaction with free surface waves. This fluid-structure interaction (FSI) commonly is modelled assuming small waves and taking the wetted surface of the ship constant, such as in added resistance [57, 34, 7]. Also when assessing the hydroelasticity of ice sheets in the ocean [82] or a multi-body wave energy harvester [108], the wetted surface is considered constant. We are however interested in the situation in which interaction with waves causes large variations of the wetted surface of the structure. Typical examples of these situations are the speed loss of ships sailing through large waves and the speed variations of a planing ship in initially calm water. Moreover the large change in wetted area and the interaction between the load and the structure has potentially a large effect on the load, as is described for sloshing model tests in [64]. Existing models to describe these effects are limited, and therefore numerical methods such as Computational Fluid Dynamics (CFD) need to be used to evaluate them. We focus on the interaction of water waves with maritime structures, which is characterized by the following three points:

1. The average density of the structure is approximately equal to the average density of the fluid (required for buoyancy, and in contrast to for instance an airplane, which is held in air by lift). Because of this, maritime structures generally have a large added mass. This is important because a small change in wetted area could give a large change in added mass.

2. The change in wetted area is large and varies constantly due to water waves and structure motion

3. The motion of the structure is large, oscillatory and originates primarily from the rigid body modes. The structure is increasingly stiff from global to local structural level.

It is a challenge to find validation cases for FSI codes which satisfy all aforementioned points. For instance [101], require FSI to consider the sound of a flapping airfoil, [85] study large-amplitude, vortex-induced vibration of an inverted flag. These are typical examples of FSI, but they do not satisfy our criteria 1 and 2. One validation experiment describes a sloshing tank with a continuously submerged beam that deforms in waves as the tank is rotated [15]; this study does not satisfy criterion 2. Another experiment is a dam break held back by an elastic flap [62] or a dam break on a vertical cylinder [54]. In the latter two, the structure transitions from wet to dry (criterion 2), but does not undergo the back-and-forth motion induced by free surface waves (criterion 3). An oscillating wave surge converter is investigated in [100, 99], where the structure is mainly submerged. A study of incipient motion of sea bed particles in waves is presented in [63]. Wave loadings on horizontal axis tidal turbines are considered in [30]. The experiment of [20] includes the variations of the wetted surface of a fixed wall with a parapet. The hydroelastic response of a vertical strut in waves is studied in [105], while [45, 46] deal with submerged plates and decks in waves. These references feature motion, sometimes large (criterion 3), but they do not account for large variations in wetted area (criterion 2). Summarizing, to our knowledge there are no existing benchmark problems that satisfy all our demands at the same time.

In order to fill this gap, we propose a fundamental benchmark problem to validate numerical codes for maritime FSI applications. The novelty with respect to existing literature is that we study a structure in the interface between water and air that undergoes motion as its surface changes from dry to wet in non-breaking waves. As a model for the structure we choose a pendulum. Earlier [71] studied the free decay of a pendulum that is always submerged, [2] studied the dynamics of a pendulum loaded by analytical models of wave profiles, [60, 61] studied a pendulum on a barge that is excited by waves. Ours is suspended above the mean free surface and then periodically loaded by monochromatic waves. Therefore this experiment satisfies all three criteria. With our experiment, we answer the following question: *How does an initially dry structure respond to monochromatic wave loading?* In other words, our objective is to use the pendulum to obtain a more fundamental understanding of the interaction of a maritime structure with free surface waves.

The experimental data and a description thereof are available as open data [102].

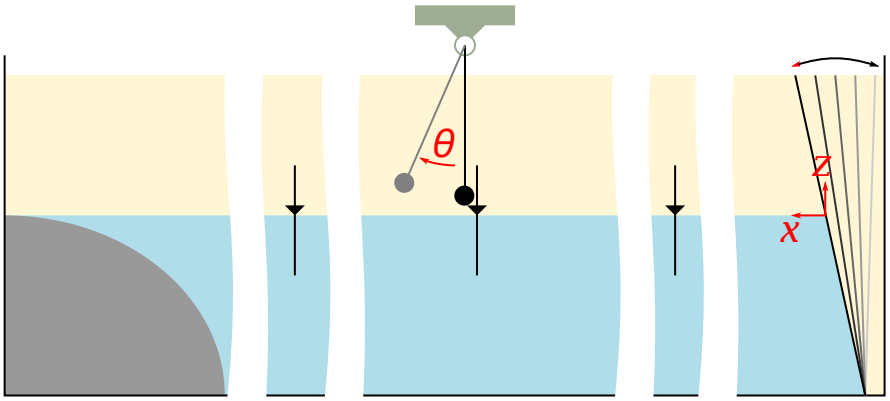

Figure 2.1: Schematic overview of the experimental setup. At the far left side the beach, at the far right the wave maker with the axis system. In between, the three wave gauges at 25.849 m, 29.880 m and 34.666 m from the wave maker, as well as the pendulum at 29.880 m from the wave maker.

2.1 Experiment

The experiment was conducted in the small towing tank of Delft University of Technology. A schematic overview of the pendulum above the towing tank is shown in Figure 2.1. It shows the pendulum together with three wave gauges. The left side of the overview shows the wave dissipating beach, the right side shows the wave maker. The axis system of the experiment is at the horizontal position of the wave maker at the vertical position of the mean free surface. We have chosen the positive x axis in the propagation direction of the waves, and the angle of the pendulum is positive when it moves along with the waves.

Figure 2.2 shows photos of the front and side view of the experimental setup. The front view shows the pendulum suspended from the towing carriage. It also shows that extra care was taken to rigidly fix the frame supporting the bearings by shoring it to the carriage with transverse braces. The right image shows the pendulum from the side of the tank with the wave gauge nearest to the pendulum in the background.

The pendulum consists of two parts: the frame and the tube. The frame is made of aluminum profiles and connected with two bearings to the towing carriage. Thin strips, which are assumed to be drag free, connect the frame to the tube. In this way only the tube experiences hydrodynamic loading and not the frame. The tube is positioned 10 mm above the mean free surface level, with the pendulum fulcrum at 1050 mm above the center of the tube. A PVC tube with a diameter of 50 mm and a length of 1500 mm was chosen.

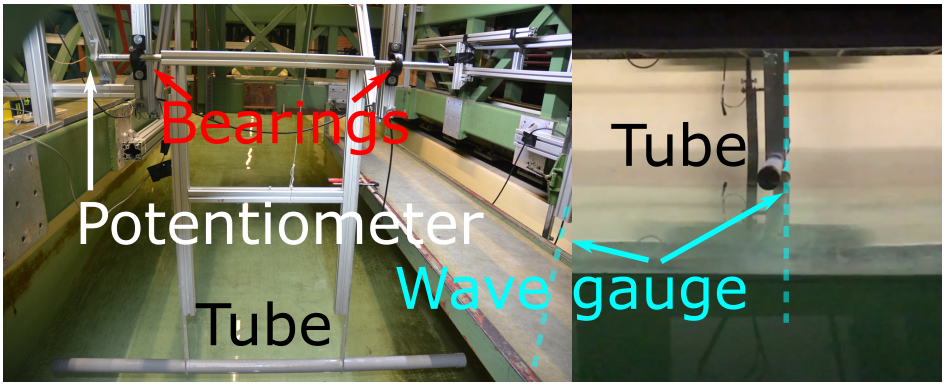

Figure 2.2: Photos from front (left) and side (right) of the experimental setup, showing the frame, bearings, potentiometer and wave gauge nearest to the pendulum. These photos are a close-up of Figure 2.1.

It is taken nearly as long as the tank is wide to make 3D wave interaction effects negligible compared to the overall loading, yielding essentially a 2D experiment. We chose a tube because the shape does not change when it rotates. The drag coefficient, therefore, does not depend on the angle of the pendulum. End caps are fitted to the tube to make it watertight.

The pendulum is positioned 29.880 m away from the wave maker. The wave maker rotation is prescribed and the generated waves pass three wave gauges: one in front of the pendulum, one at and one behind it. Measured with a laser distance meter, they are at 25.849 m, 29.880 m and 34.666 m from the wave maker. When wave interaction with the tube begins, the pendulum starts rotating, which is measured by a potentiometer. The pendulum was weighed on a scale to a mass of 8.86 kg. The center of gravity was found by putting it over a support and moving it until stable. It was positioned at 365 mm from the fulcrum, giving a restoring force coefficient $k = 31.7$ N m rad^{-1}.

The potentiometer is calibrated by giving it 10° rotations within its measuring range and fitting a straight line. Over the complete range the maximum error with respect to the fitted calibration factor is within 0.5°[1]. The wave gauges are calibrated by measuring the output at 20 mm intervals and also fitting a straight

[1] A printed protractor was used and the potentiometer is turned by hand. It is likely that there is some error introduced in the 10° increments, which is likely the dominant component in the measurement error. Looking back this calibration should have been done more carefully, repeated many times to even out the manual error in setting the angle. From the data it seems plausible that the error is due to manually setting the potentiometer, because there is random scatter around a linear relation. The 0.5° is about 10 mm at the tube of the pendulum. This is much smaller than the smallest wave lenght of 10 mm. Because of this and because the same calibration is used all the time the error with respect to a better calibration is considered negligible.

Table 2.1: Name, position and error of the three wave gauges in the experiment.

Name	Position	To Pendulum	Measurement error
WHM 1	Side of the wave maker	-4.031 m	0.5 mm
WHM 2	At pendulum	0.000 m	0.3 mm
WHM 3	Side of the beach	4.786 m	0.6 mm

line. Table 2.1 shows the names, positions with respect to the pendulum and maximum errors with respect to the calibration of the wave gauges.

At the beginning of each test the average signal of the first second defines the new 'zero', for which the entire signal is corrected; this corrects for drift in the wave gauges. All measurements are taken at 1000 Hz and then passed through a 100 Hz analog second order low pass filter. Additionally, we applied a digital moving average filter with a width of 25 samples for four times to remove higher vibration modes of the pendulum.

The wave maker generates waves according to a sine wave modulated with a window function to slowly ramp up the signal towards the desired amplitude and then down again. The signal is held at the desired amplitude for 50 s.

Each test features one wave length: $\lambda = 1$, 3, 5 or 7 m, with three repetitions for each wave length to get a quantification of the variability between experiments. The water depth was kept at 994 mm for all experiments, a wave amplitude of 50 mm was desired. Two measures were taken to keep the starting conditions for each experiment the same. First, because shorter wave modes dissipate faster, the tests were done in a series of increasing wave length. Second, a waiting time of 15 minutes was taken between tests to allow the water in the tank to come to rest. The effectiveness of these measures is assessed in the results section.

2.2 Analytical model

To better understand the experimental results we will use an analytical model based on the following assumptions. The pendulum has only one degree of freedom: rotation about its fulcrum. Only the tube at the bottom of the pendulum experiences a hydrodynamic force, which is constant along the length of the tube (width of the towing tank). Every occurrence of wave interaction in our experiment has four phases:

1. Water entry: the wetted area increases over time [96, 72]
2. Submerged motion: fully wet, with mostly drag and buoyancy [74, 71]
3. Water exit: wetted area decreases over time

4. Free vibration: only air and friction damping [29]

Water entry and exit can generate high peak pressures [94, 70], which are generally localized in space and time. Because the pendulum integrates all local pressures in its global motion we will assume that we can neglect peak pressures. The buoyancy force acts upward and is multiplied with the position and sine of pendulum angle to obtain the moment on the pendulum. For small angles, the moment is small and therefore ignored. Other studies [29] mention that the air drag is small, and therefore it is not taken into account here. We will reflect upon these assumptions in the results section.

The following reduced-order model describes how the pendulum responds after the interaction with the waves starts. The first component of the model is the equation of motion of the pendulum:

$$I\ddot{\theta} + c\dot{\theta} + k\sin\theta = M \tag{2.1}$$

where I is the inertia, c damping and k the restoring force coefficient, with θ the instantaneous angular position and M an external moment. We performed a free vibration test with the pendulum to determine these parameters. By taking the first and second time derivative of the angle we obtain the angular velocity and acceleration. These are substituted into the equations of motion to find the inertia and damping with a least squares approximation. With $k = 31.7$ N m rad^{-1} found as described above, we obtain the values $I = 2.17$ kg m^2 and $c = 0.205$ N m s rad^{-1}.

Figure 2.3 shows the free vibration of the experiment and reduced-order model (with M in Eq. 2.1 equal to 0) for the same starting position. Eq. 3.1 was rewritten in a state-space representation and integrated numerically with two-stage Runge-Kutta. The figure shows results for three time steps: 20, 10 and 5 ms. Reducing the time step from 20 ms to 5 ms does not bring about a significant change in error: 0.2% comparing the final maxima. We however choose to use the 5 ms time step to have enough temporal resolution to capture the period of the shortest waves (period $T = 0.8$ s for $L = 1$ m) with more than 150 time steps. The reduced-order model in Figure 2.3 shows a slightly faster decay than the experiment, which is likely because the actual dissipation mechanisms require more elaborate modelling than a linear damping coefficient. However, at the last shown maximum angle after 7 full periods of 1.64 s, the reduced-order model is only 0.07 s and 0.5° behind the experiment. This error is smaller than the calibration error of the potentiometer, and therefore acceptable. In comparing the model with the experiment, the time integration error has even less influence, because repeated wave forcing takes place in intervals of at most 2.5 s (period of the longest wave of 7 m), and the modelling error of the wave force is larger than the numerical error.

The forcing on the pendulum M is modelled as the cross product of moment arm, given as $L = 1050$ mm above, and the hydrodynamic force on the tube F_m scaled

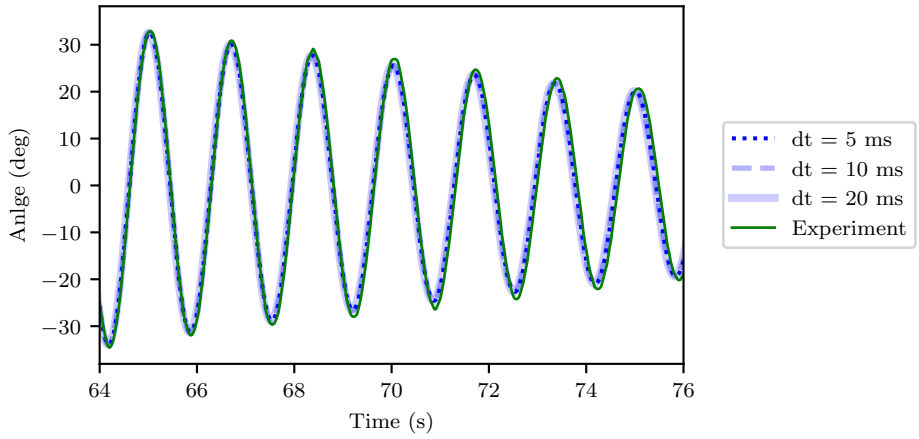

Figure 2.3: Reduced-order model of free pendulum decay fitted to the experiment, with convergence study for the time step.

by a factor β:

$$M = \beta F_m L \cos\theta \tag{2.2}$$

The reason for scale factor β is elaborated upon below. The force on the tube per unit width is given by the Morison equation [74]:

$$F_m = \rho \left(C_m V a + \frac{1}{2} C_d A |u| u \right) \tag{2.3}$$

Here, ρ is the density of water, taken as 1000 kg m^{-3}. Parameters C_d, C_m are the added mass and drag coefficients based on the Keulegan-Carpenter number KC, which can be found in [86]. Variables a, u are the acceleration and velocity of the water relative to the pendulum. The frontal area and volume of the cylinder are given by A and V.

One of the key ingredients of our experiment is the large change in wetted area. Since the pendulum is not completely wet or dry all the time we need another function to estimate the wet surface. How the force on a horizontal member depends on the wet surface was hypothesized before by [55], who alter drag and added mass coefficient with an analytical model, yet without validation. They describe only vertical forces, where we need a model for the horizontal force. In the model we approximate the varying wetness with a scaling factor for the Morison equation: our novel wetness parameter β. This parameter is 0 for a dry cylinder and 1 for a fully submerged cylinder, and linearly scales based on the submersion depth at the center of the tube:

$$\beta = \max\left(\min\left(\frac{\eta - (z_p - D/2)}{D}, 1 \right), 0 \right) \tag{2.4}$$

where D is the tube diameter, η wave elevation and z_p the instantaneous vertical position of the center of the tube. Note that for an underwater pendulum $\beta = 1$, which yields the equation of motion in [71]. While this wetness function is a large simplification of the physics that take place with water entry and exit, we believe it can be seen as a suitable approximation to explain the results of the experiments.

In our model we first assume that the free surface waves satisfy small amplitude potential flow, or Airy theory. Disregarding start-up effects and reflection from the beach, the surface elevation is then described by:

$$\eta = \eta_a \cos(k_w x - \omega t)$$

where ω, k_w are the angular velocity and wave number, and η_a is the amplitude. The velocity and acceleration of a fluid particle in horizontal direction are:

$$u_p = \eta_a \omega \frac{\cosh(k(z+h))}{\sinh(kh)} \cos(k_w x - \omega t) \tag{2.5}$$

$$a_p = \eta_a \omega^2 \frac{\cosh(k(z+h))}{\sinh(kh)} \sin(k_w x - \omega t) \tag{2.6}$$

For the Morison equation we however need the relative velocity and acceleration of the water with respect to the pendulum:

$$u = L\cos\theta\dot{\theta} - u_p$$

$$a = L\cos\theta\ddot{\theta} - L\sin\theta\dot{\theta}^2 - a_p$$

Where the first term in the velocity equation and first two terms in the acceleration equation are derived from the pendulum kinematics. Velocities and accelerations above the still water level are obtained by constant extrapolation from the value at the mean free surface position.

The interaction between waves and pendulum is a nonlinear process. For the chosen steepnesses the waves themselves are also nonlinear, albeit mildly. In order to investigate how important this wave nonlinearity is, the reduced order model was equipped with the nonlinear steady wave solution proposed by Rienecker and Fenton [83]. This is a wave solution that follows from fitting a truncated Fourier series to the nonlinear flow equations and nonlinear boundary conditions at the initially unknown instantaneous position of the free surface. The solution features no errors other than from truncating the Fourier series. As such, it is a more suitable approach for modelling the waves in our experiment in limited water depth, than the more often used nonlinear Stokes steady wave solution that is based on an expansion around the mean free surface with an expansion error and the requirement that the water depth should be sufficiently deep for the expansion to converge. Our nonlinear waves with the Rienecker-Fenton approach were solved with $N = 16$ Fourier components and converged until the error was smaller than 10^{-10}.

In order to determine the forces on the tube we need to use the drag and added mass coefficients C_d and C_m. These coefficients depend on the Keulegan-Carpenter number, in which we use the particle velocity, wave period and tube diameter. Since we use constant extrapolation for velocities above the water we substitute the amplitude at $z = 0$ m from Equation 2.5:

$$KC = \frac{UT}{D} = \frac{\eta_a \omega \frac{\cosh(k(z+h))}{\sinh(kh)} \frac{2\pi}{\omega}}{D} = \frac{2\pi\eta_a}{D} \tag{2.7}$$

which, by using 50 mm for the diameter D of the tube and 50 mm for η_a, gives $KC \approx 6$. From [86] we find $C_d = 2.0$ and $C_m = 1.0$ for our setup. Note that two assumptions are made here. First, choosing the particle velocity in determining KC is a modelling choice; we can equally well justify using the relative velocity of the pendulum with respect to the undisturbed wave particle velocity, as this is the velocity the tube truly experiences. That would make the procedure somewhat cumbersome, however. Second, we assume that the added mass and drag coefficients are equally valid for partially submerged cylinders as they are for the fully submerged cylinders from the original experiments.

2.3 Results and discussion

Here we describe the results of the experiment with the help of the analytical model. Then we compare the repetitions of the tests in order to investigate the variability of the surface elevation and the motion response of the pendulum. The waiting time of 15 minutes between each experiment was found to be sufficient because the wave gauge signal at the start of a new experiment was of the order of the calibration error of the wave gauges.

2.3.1 Comparison with analytical model

The comparison between experiments starts after the wave elevation at the second wave gauge (next to the pendulum) has reached the desired level. The 20 s of signal after that is input to our analysis. After that, there will be reflection from the longest wave components that exist due to ramping up the wave maker signal. The simulations are started at arbitrary time instances and run for 20 s. Then the transient response is cut off and the 'steady' part is compared to the previously selected 20 s of the experiment. Time synchronization between the experiments is done using a synchronization pulse. To synchronize the experiments with the numerical results the second wave gauge (WHM 2) and modelled surface elevation at the pendulum are matched.

The measured and modelled waves are plotted in Figure 2.4: in green the three repetitions of the experiment and in blue dashed lines the analytical model. We aimed for 50 mm wave amplitude in all tests, which is close to what was achieved (an average of $\eta_a = 45, 54, 50, 45$ mm for $\lambda = 1, 3, 5, 7$ m respectively). The steepness of the waves equals $H/\lambda = 0.090, 0.036, 0.020, 0.013$, the steepest wave

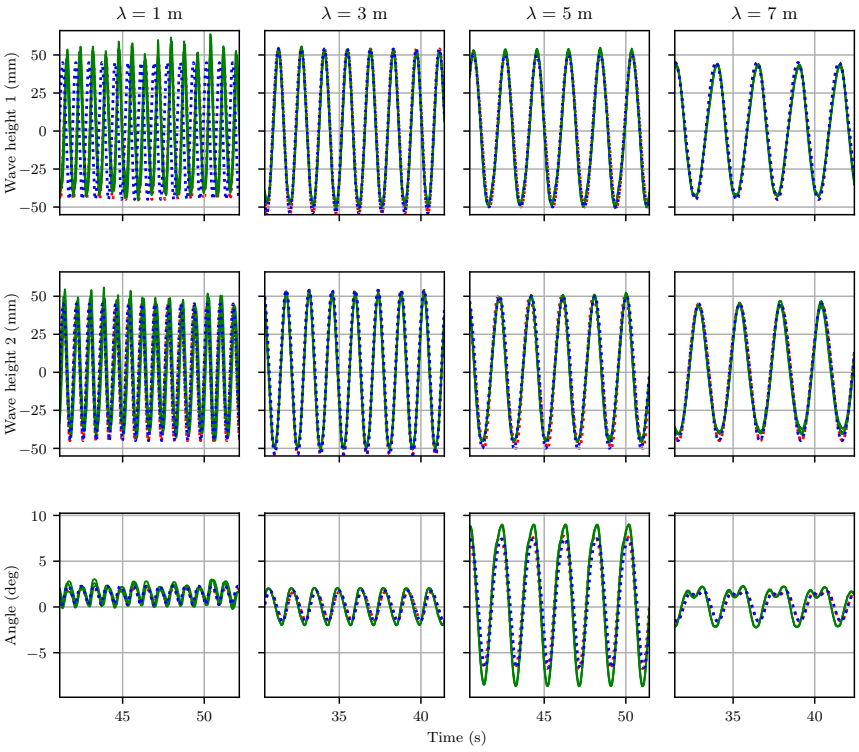

Figure 2.4: Wave elevation for wave gauge 1 and 2 (top two rows) and pendulum response (bottom) in experiment and model. Wave height measured at pendulum rest location. Legend same as in Figure 2.3, the additional red dotted line shows the results using the Rienecker-Fenton wave model [83].

therefore is slightly over half of the breaking limit of 1/7. Wave breaking is not expected, but the shortest wave demonstrates nonlinear behavior. As the wave length λ depends on wave height for steep waves we see a slight phase difference between simulations and experiment in WHM 1 for the shortest (and steepest) wave.

Fig. 2.4 shows that the free surface extremes are somewhat irregular. These irregularities do not repeat well between tests, as becomes apparent from the green lines for $\lambda = 1$ m that do not completely overlap. For the other wave lengths, the green lines overlap is nearly complete.

Additionally Figure 2.4 shows the pendulum response for the four wave lengths: positive response means the pendulum swings towards the wave maker. Recall that the dry natural period of the pendulum was found to be 1.64 s. The wet natural period of the pendulum is expected to be higher because of added mass.

The first thing that stands out is the average value of the response, which is close to zero for all but the 1 m wave length. Apparently, loading the pendulum with a wave period much lower than the natural period results in a mean position shift. This mean position shift marks the nonlinearity in the response, as the incoming wave is nearly sinusoidal with zero mean. We also observe that the pronounced maxima, and the irregularity of the maxima that are present in the surface elevation, are transferred to the pendulum motion.

The response to the 5 m wave is highest, indicating that resonance occurs for a period close to this wave's period. As expected, the natural period for our wet-and-dry pendulum is higher because of added mass, which cannot be assumed constant because the pendulum transitions from dry to wet intermittently. A clear indication that the resonance period of the pendulum with added mass is between the periods for the waves with $\lambda = 3$ m and $\lambda = 5$ m, is that the phase between the wave height and the pendulum response changes from in-phase to counter-phase. Finally, we reflect on the shape of the 7 m wave signal. Here there are two maxima: the first one is from the free vibration stage, when the pendulum is dry. When it is swinging back, the pendulum is grazed by the wave, giving a second maximum. We can see energy is added in this latter peak because it is higher than the previous one. The wave period is long enough to allow the pendulum to go fully in the other direction and back, after which the process repeats. For even longer waves we expect this to be more pronounced (although this could not be tested due to stroke limitations of the wave maker). This is also a clear nonlinear effect. The incoming 7 m wave is close to sinusoidal as shown by the wave gauges. Then the double peak in the response demonstrates that frequency components higher than the wave frequency were generated in the interaction between pendulum and waves.

In Figure 2.4, and more clearly 2.5, the red dotted line shows the wave profile following [83] and the response of the pendulum when using this wave model with

Table 2.2: Ratio of modelled response due to a 10% lower and higher wave amplitude compared to the original wave amplitude.

η_a	$R\|\lambda = 1$ m	$R\|\lambda = 3$ m	$R\|\lambda = 5$ m	$R\|\lambda = 7$ m
+10%	1.24	1.17	1.08	1.35
-10%	1.28	1.20	1.13	1.40

the higher frequency components. The wave height at wave gauges 1 and 2 is very similar to that of the Airy model, even when zooming in. The pendulum response to the Rienecker-Fenton wave is somewhat lower than for the Airy wave, which is explained by the crests of the Rienecker-Fenton wave being sharper. With sharper crests the pendulum is under water for less time, allowing less time for energy transfer. As the waves become longer, meaning less steep, the wave becomes more sinusoidal and the models overlap again.

The wave height is not exactly constant during a single test, due to for instance start up effects or interaction with the pendulum. It is therefore interesting to investigate by means of the analytical model what the sensitivity of the response is to a change in the wave amplitude. Figure 2.5 shows two additional lines compared to Figure 2.4, representing the response to a regular wave with a 10% bigger or smaller amplitude. A 10% higher amplitude means 10% higher velocity, with quadratic drag that should lead to a 21% larger response. Table 2.2 shows what this 10% change in wave amplitude does. It gives the ratio R of increased or reduced pendulum amplitudes over the original response amplitude, for all wave lengths. Surprisingly, the 5 m wave which excites the pendulum near its natural frequency shows the least sensitivity to change in amplitude. The effect of increasing the amplitude is smaller than the effect of decreasing it. Another counter-intuitive finding is that the expected ratio of 1.21 is only found for the 3 m wave. For the other wave lengths, wetness clearly also has a large influence on the sensitivity of the response amplitude to changes in the wave amplitude.

The analytical model is a good representation of the experiment because it captures important aspects of the dynamic interaction between waves and pendulum and allows us to investigate the experimental results in more detail. From the comparison with the analytical model we find that the main drivers for nonlinear motion behaviour are the wetting and drying of the pendulum and the drag on the cylinder when it is under water. Note, however, in Figure 2.5 that the response from the experiment is not inside the band formed by the analytical results with lower and higher amplitudes. This is an indication that in the experiment more is going on than can be captured by the analytical model. The water entry, buoyant behavior and water exit are included in the experiment but not in the model. Structures in the interface between water and air are notoriously difficult to study by means of numerical models, because the intermittent presence of the structure breaks the continuity of the interface. Apparently, even for situations that are not that violent, modelling a structure that is in one medium for some

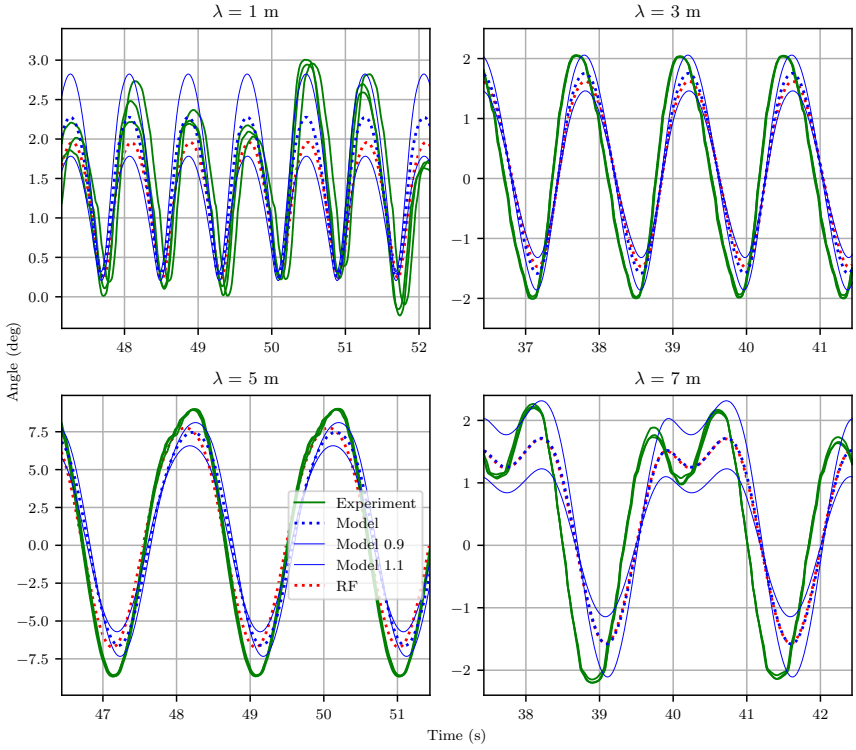

Figure 2.5: Detailed response of the pendulum. The model response has a band representing the outcomes when the wave amplitude is increased or decreased by 10%. RF is the nonlinear wave model of [83]

time, and then transitions to the other medium for the next stretch of time, will require numerical techniques like Volume-of-Fluid or Level Set to capture the air-water interface near the structure. This is why we believe the experiment can be a useful benchmark for the community that works on developing these techniques.

2.3.2 Variability

In Fig. 2.5 the variability (dissimilarity or irregularity of surface and pendulum position from period to period) is largest for the steepest wave with $\lambda = 1$ m. The variability in the surface elevation is transferred to the angular position of the pendulum. But is the variability of the angular position as large as of the surface elevation?

Loading as a result of wave interaction with free-surface-piercing structures is highly variable [17]. It was reported that - locally - pressures on a wall resulting from the same (or highly similar) wave input were strongly dissimilar, but also that - globally - the wave force on the wall varied between experiments with the same input [47]. Among others, [17] and [47] also found that the impulse, which is the integral of force over a meaningful time span, between experiments shows less variability. The analyses using impulse have in common that the structures are fixed and rigid, and therefore cannot undergo a change of momentum. Translating this approach to our experiment with a structure that is free to move, leads to the hypothesis that the variability of the motion response is smaller than that of the wave input.

Figures 2.6-2.9 show the variability of the measured surface elevation at WHM 2 and the measured angle of the pendulum. Here we divided the signal in parts as long as the period of the incoming wave. All these parts are then shifted to start at the same time. The minimum, maximum and, 25th, 50th and 75th percentile are calculated at every time instant and plotted in a single graph per experiment repetition. The top row shows the wave height at the pendulum, the bottom row shows the pendulum angle. Each column is one repetition of the experiment with the same input parameters. Table 2.3 shows a summary of the peaks of the wave elevation η and the pendulum response θ as well as the number of peaks n. For both of these variables the mean and coefficient of variation (CoV, standard deviation divided by mean) are given.

Table 2.3: Summary of the results: wave length, test series, number of tests n, mean and coefficient of variation of maxima response θ and wave height η.

λ, series	n	mean max θ	mean max η	CoV max θ	CoV max η
(1.0, 300)	28	2.36	47.8	0.230	0.100
(1.0, 304)	28	2.40	49.6	0.176	0.0874

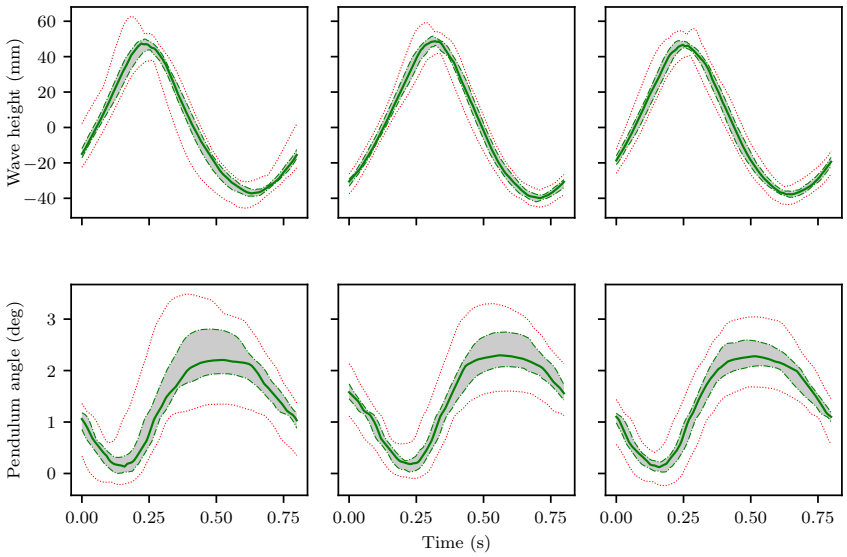

Figure 2.6: Surface elevation (top) and response (bottom) in experiments for wave length $\lambda = 1$ m, with statistics over 28 periods. Left, middle and right column represent the first, second and third repetition of the test. Mean position at a time indicated by continuous green, 25th and 75th percentile indicated by dashed green and the grey band, minimum and maximum values indicated by dotted red.

λ, series	n	mean max θ	mean max η	CoV max θ	CoV max η
(1.0, 308)	28	2.32	47.9	0.170	0.0759
(3.0, 301)	15	2.03	52.9	0.0551	0.0316
(3.0, 305)	15	2.02	52.9	0.0596	0.0305
(3.0, 309)	15	2.04	51.8	0.0561	0.0315
(5.0, 302)	10	9.00	49.6	0.0143	0.0323
(5.0, 306)	10	8.87	49.2	0.0217	0.0250
(5.0, 310)	10	8.92	48.4	0.0143	0.0195
(7.0, 303)	7	2.14	44.8	0.0254	0.0376
(7.0, 307)	7	2.15	43.6	0.0332	0.0181
(7.0, 311)	7	2.22	43.1	0.0324	0.0136

For the longer wave lengths $\lambda \geq 5$ m in Figures 2.8 and 2.9 we see the 25th and 75th percentile results visually overlapping, meaning there is not much variability. This is also shown in Table 2.3. For $\lambda = 3$ m we see a surface elevation with hardly any variability, but a larger variability for the pendulum angle. The shortest wave $\lambda = 1$ m has the largest variability in both surface elevation and

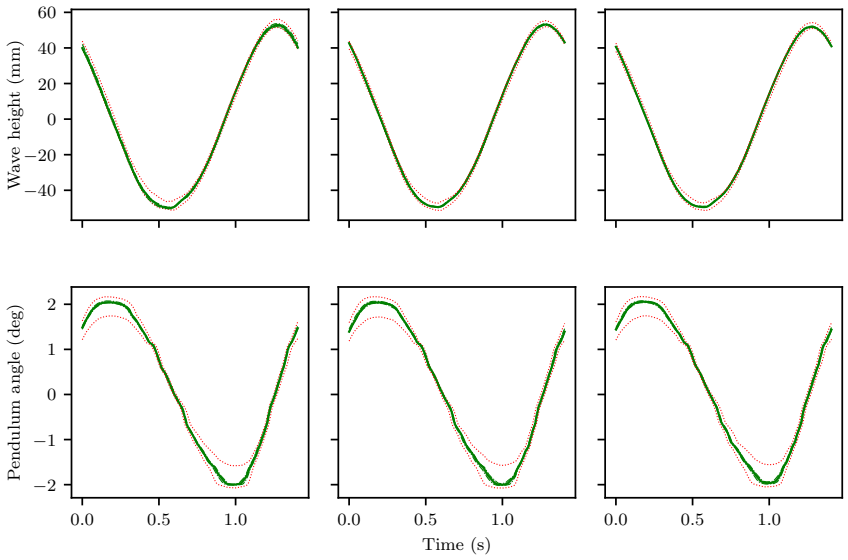

Figure 2.7: Surface elevation (top) and response (bottom) in experiments for $\lambda = 3$ m, statistics over 15 periods. Description as in Fig. 2.6.

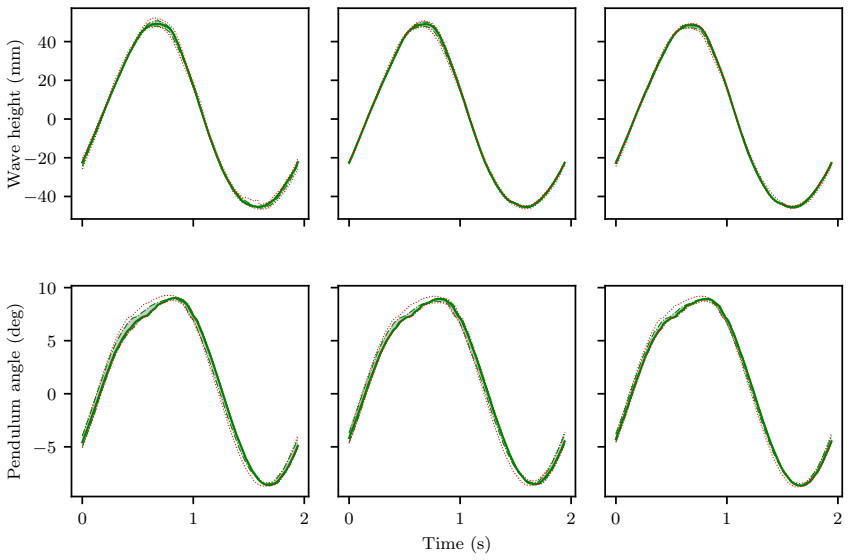

Figure 2.8: Surface elevation (top) and response (bottom) in experiments for $\lambda = 5$ m, statistics over 10 periods. Description as in Fig. 2.6.

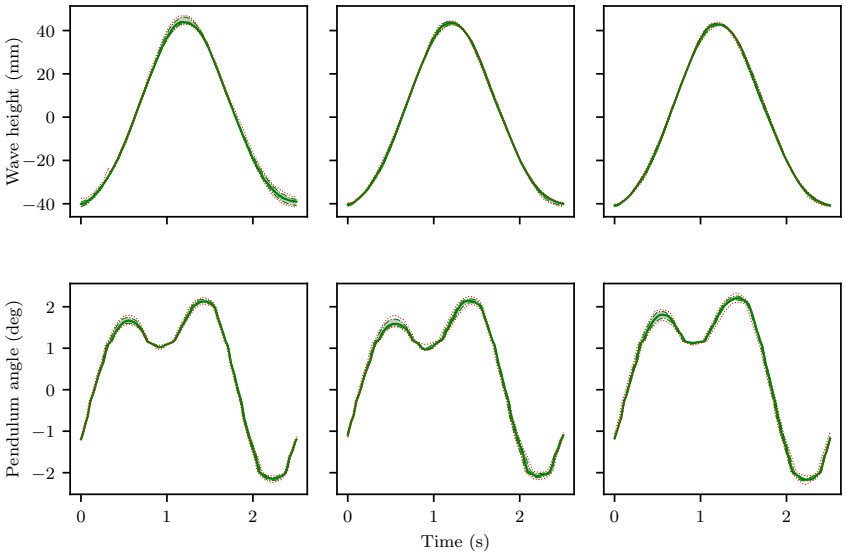

Figure 2.9: Surface elevation (top) and response (bottom) in experiments for $\lambda = 7$ m, statistics over 7 periods. Description as in Fig. 2.6.

pendulum angle, which is true for all repetitions. For almost all experiments, the pendulum response has larger coefficient of variation than the wave height. This finding disproves the hypothesis, which stated that the variability of the fluid is local and would be smeared out in the global response of a structure. Instead variability of the fluid is amplified in the structural response. Note in Table 2.3 that the $\lambda = 1$ m wave of series 300 has a coefficient of variation of 0.10 on the wave elevation, giving a coefficient of variation of 0.23 for the maximum angle. A similar sensitivity was found with the analytical model for this wave length, as shown in Table 2.2.

We conclude that the variability in the wave is amplified by the interaction with the pendulum. Using the findings from Table 2.2 confirms that a small variation in wave amplitude can indeed in most cases cause a superlinear increase in the response. Figures 2.6-2.9 and Table 2.3 show that the pendulum response is more variable when the angle is positive, that is when the pendulum is dragged along by the wave. Underwater turbulence may explain the added uncertainty when the pendulum is loaded by the wave. The pendulum swings through the wake field it has left, which is different for every loading cycle. This would imply that the drag coefficient changes as the experiment progresses. Another possibility is that the structure starts moving already due to some droplet or filament. With this initial velocity the relative velocity between fluid and structure changes, giving a different response.

2.4 Conclusions

In this paper we have presented a benchmark experiment for fluid-structure interaction in maritime applications: a pendulum in monochromatic waves. The experiment captures water entry, submerged behavior and water exit, modelling the large variations of wetted area that are typical for structures at sea. Large variations in wetted area cause different types of motion behavior for different wave lengths. For a wave period much smaller than the dry natural period a mean position shift of the pendulum was observed. For a wave period much larger than the dry natural period, secondary local maxima in the signal of the pendulum position were observed[2]. As expected, resonant motion behavior for a wave period higher than the dry natural period was observed (higher because of added mass).

A reduced-order model was made which includes the added mass and drag components of the hydrodynamic loading, together with a wetness factor. A good comparison between model and experiment was obtained. The distinguishing dynamics of the wet-and-dry pendulum are captured by the model, and the Morison equations with the chosen coefficients are suitable for the entire wet-and-dry behavior. The main drivers for nonlinearity are the wetting and drying and the drag. Seeing the small angles we obtained confirms buoyancy was rightfully disregarded from the model. There is no reason to assume that inclusion of air drag or buoyancy would have altered the results significantly.

A sensitivity analysis with the model that varied the wave amplitude demonstrated that model and experiment differ in details. A better correspondence would require a model that is able to represent the water entry and exit phenomena. Going into more detail it should model the wake of the pendulum as well as droplets and filaments. On the other hand, using linearised potential flow with small surface waves proved to be good enough.

The variability in surface elevation for waves with $\lambda \geq 3$ m was low, the variability of the shortest wave length was clearly the largest. For nearly all experiments the variability of the surface elevation was amplified in the response of the pendulum. This is confirmed by the sensitivity study, which showed that a 10% difference in wave amplitude gives a larger than 10% increase in pendulum response for all wave lengths except the 5 m wave. A hypothesis, extended from the literature about using impulse to interpret wave loading on non-moving structures, that the variability in the motion of the structure should be lower than that of surface elevation, could not be confirmed. The variability was also found to be larger when the pendulum is dragged along by the wave, than when the pendulum moves back through air.

We believe that the presented experiment is a good benchmark for maritime FSI

[2]The secondary maximum can also be considered a memory effect, where the pendulum was hit again before it came to a rest.

problems. The experiment could be augmented by investigating local vibrations of the structure, or additional (plastic) hinges. This will keep the experiment simple, but allows validation of other FSI phenomena. Another idea would be to repeat these tests for focused waves instead of monochromatic waves. Focused waves can be higher, and have a larger horizontal velocity when they break, increasing the water entry forces.

Chapter 3

Fluid Structure Interaction Between a Pendulum and Focused Breaking Waves

Based on R.W. Bos, P.R. Wellens. 'Fluid structure interaction between a pendulum and focused breaking waves' (2021) Physics of Fluids, 33 (6), art. no. 062118.

Safe containment of Liquefied Natural Gas (LNG) during transit requires hydroelastic evaluation of load and structural response. Predicting the time evolution of the structural deformation during a breaking wave impact by means of a numerical method is challenging. This article is about an experiment for a fundamental deforming structure in a breaking wave, that may serve as a benchmark for numerical methods. The experimental data and a description thereof are available as open data [103].

LNG will play a large role in making the maritime industry sustainable by replacing other more polluting fuels [28]. It is possible to safely transport LNG at -162° when the tanks are either nearly full or nearly empty. This avoids waves on liquid cargo, waves that can significantly damage the structure. Because the temperature of LNG would make the ship brittle, the tanks are fitted with insulation, called a cargo containment system (CCS)[49]. When using LNG as fuel the tanks will become less and less full, at some point creating the ideal situations for large breaking waves inside the tanks. Breaking waves pose a key challenge for the insulating membrane of LNG fuel tanks compared to the more traditional LNG cargo tanks.

Impacts of a breaking wave against a wall without hydroelasticity have been studied in detail: [65] consider the flip-through wave impact with detailed Particle Image Velocimetry (PIV) measurements and report vertical flow accelerations of $1500g$. Also for sloshing it is noted that breaking waves give higher loads than

waves that do not break [48]. In [66] there is a focus on the entrapped air cavity in a plunging breaking wave against the wall, whereas [93] measure the free surface in the tip of the plunger to study instabilities that would lead to variability in the pressure during impact.

A typical way to decrease the variability is not to look at local pressures, but rather at the pressure impulse [80, 41]. This is the time integral of a local pressure, thus integrating out the variability in time. Alternatively the pressure can be integrated over the structure to obtain a force or moment, effectively reducing the variability in the spatial dimension. This is discussed in [91], with as main benefit that the force relates well to the modal response.

In [10] sloshing is examined with more focus on the structure by sending breaking waves to a wall, modelling the insulation of an LNG tank of a ship. It is mentioned that a local impact load can lead to global deformation of the structure. For slamming, closely related to sloshing, hydroelasticity is investigated in for instance [32, 98]. Two impact phases are distinguished here: the structural inertia phase in which the beam accelerates due to an impact, and the free vibration phase in which the structure is submerged. Experimental validation shows that this distinction is valid. The hydroelastic slamming response in shallow-liquid sloshing with a hybrid experimental/numerical method is considered in [64] with overall good results. The maximum peak pressure was only found to correspond to the experiment when the added mass effect was considered. The hybrid method was however not able to reproduce the time evolution of the deformation of the structure.

Breaking wave impacts are not limited to situations with sloshing. For instance, [21] studied breaking wave impacts on a wind turbine foundation pile with nonlinear potential flow and a high-order boundary element method. Wave impacts are also considered for oscillating wave surge converters [99]. Another closely related problem is wave impacts for green water which are investigated in [23, 4]. A lab experiment is conducted to study a transient wave impact on a deck above the free surface. Similar impact loads of plunging breaker on a tension-leg platform (TLP) in 2D are discussed in [22], where the void fraction of the water hitting the structure is taken into account. Taking the void fraction into account gave a more accurate estimate of the impact coefficients, which predict the maximum impact pressure. Additionally one could take the pressure impulse, which is more repeatable than the maximum pressure [80]. However, for the structural response the exact temporal and spatial distribution of the load matters, especially when considering that the load also depended on the motion of the structure.

As mentioned in [13], fluid structure interaction for maritime applications (or hydroelasticity) has the following properties. It has high added mass, large changes in wetted area and the structures are heavy and stiff in local deformation. Hydroelasticity is considered especially important for in extreme events such as slamming, sloshing and green water. Impacts on freely floating maritime structures during

these events are a combination of many processes [59], but consist mainly of four phases [13]:

1. The wetted area of the structure increases / impact problem
2. The structure is fully submerged and vibrates with a maximum of added mass and damping
3. Wetted area decreases as the structure emerges from underwater
4. Free vibration of the structure with all energy that has been transferred

The behavior during the first phase depends on the shape of the incoming wave, as outlined in [59, 80]. Another important challenge is to account for the variability inherently present in wave impacts [36].

All four phases of fluid-structure interaction are important and, accordingly, validation problems including all these phases are required. With the experimental setup described in this article, we aimed to devise the simplest possible experimental model of a maritime structure that is free to move in extreme conditions, in order to study the variability of wave impacts. The maritime structure is modelled as a pendulum suspended above the mean free surface a towing tank. Focused waves are generated to simulate an extreme event in a sea state. The focused wave breaks near the structure and makes the structure undergo all four wave impact phases.

Traditionally many of these experiments have been performed with a rigid or flexible wall as structure, such as the sloshing experiments described by [8, 48]. [67] considered drop tests and wave impact tests with hydroelasticity. It showed that high aeration reduces the impact force for the flip-through and slightly breaking wave. The total force impulse decreases for the elastic wall, whereas the total pressure impulse increases. Hence, the scale of structure that is considered matters for whether hydroelasticity is important.

An advantage of the pendulum over a wall is that the maximum pendulum response is a measure of the impulse, force integrated over time, on the structure placed at a relevant position. The relevant position in our case is near to where the wave breaks, since that is where the highest forces are expected. An additional advantage is that the experimental setup with the pendulum above the mean free surface allows for a meaningful, almost undisturbed measurement of the wave near the pendulum, so that input to and response of the pendulum system can be compared in order to study the variability. This setup is inspired by [71], who achieve good modelling accuracy for a submerged pendulum.

3.1 The experiment and the reduced-order model

With this experiment we want to increase the fundamental understanding about fluid-structure interaction in extreme wave events for maritime applications, as well as provide reproducible validation data. This experiment uses a similar setup to [13]; the setup is explained first. An important addition to the original setup is the focused wave, so the second section describes how the waves are designed and generated. After that a reduced-order model is presented with which the experiment is compared.

3.1.1 Experimental setup

Figure 2.1 shows a side view of the small towing tank at Delft University of Technology. The structure that we call pendulum has rotation around a fulcrum as its only degree of freedom. It is shown in the middle of figure 2.1, suspended from the towing carriage and close to being impacted by the wave. On the far left is the wave absorbing beach and on the far right the flap type wave maker. Three wave gauges are mounted before, at and after the pendulum, to measure the surface elevation before, during and after interaction with the pendulum. The rotation of the pendulum is measured with a potentiometer, which goes to the same measuring system as the wave gauges. An analog second order filter with a cut-off frequency of 100 Hz is used and the data is sampled at 1000 Hz. A 250 fps camera records the motion of the pendulum and the evolution of the wave profile from the side, which is later synchronized with the measuring system using the frame in which the pendulum starts to move.

A photo of the pendulum is shown in Figure 2.2 and consists of a frame and a horizontal tube. The frame is made of stiff aluminum profiles, with two strips extending from the bottom of the frame, holding the PVC tube with a diameter of 50 mm. The tube is almost as long as the towing tank is wide so that three-dimensional effects can be considered small. The main thought behind this configuration is that only the tube has hydrodynamic interaction with the wave and that, because of its circular cross section, the hydrodynamic interaction does not depend on the rotation of the pendulum. The hydrodynamic interaction with the strips between frame and tube can be neglected. The length of the pendulum from the center of the tube to the fulcrum measures 1050 mm. We know from a least squares fit of free vibration experiments in [13] that the structural properties of the pendulum are $I = 2.17$ kg m^2, $c = 0.205$ N m s rad^{-1} and $k = 31.7$ N m rad^{-1}, with I the inertia, c the damping and k the restoring coefficient. The water depth is constant throughout the experiment at 995 mm.

The wave gauges were calibrated and the maximum difference between measured points and the linear fit was less than 0.5 mm over its entire range; for the potentiometer the maximum difference was less than 0.5°. The camera was focused and calibrated on the window in the side of the tank at the pendulum location. The recorded images have a resolution of 0.3 mm/px.

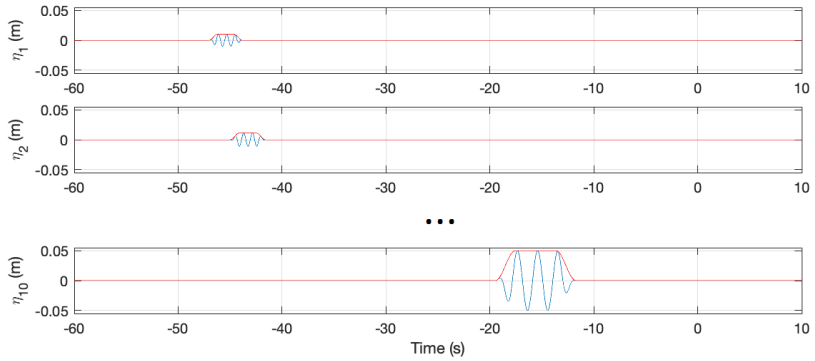

Figure 3.1: Surface elevation over time at the position of the wave maker. The first, second and final wave components of the focused wave (with window function to create groups).

The tests in the experiment were carried out with varied focus locations of the wave components (next section) and the clearance between the mean water level and the bottom of tube. Each test was repeated 5 times. All tests with the same configuration were performed after each other, with a waiting time in between tests of at least 15 minutes. This allowed the water to come to rest, with "rest" defined by the situation that the remaining free surface oscillations were lower than the calibration error of the wave gauge.

3.1.2 Wave generation

A breaking wave was generated at different locations in the tank by focusing wave components towards four focus locations in the tank at positions $x_{foc} = 29.880, 29.380, 28.880, 28.380$ m with respect to the wave maker. The latter focus position is the location of the pendulum itself. Relative to the pendulum the focus points are defined as $f = 0.0, -0.5, -1.0, -1.5$ m (in reverse order). Wave breaking takes time and distance to develop. The wave that focuses at the position of the pendulum, breaks somewhat further down the tank. It is therefore an example of unbroken wave interaction with the pendulum. The wave that focuses half a meter before the position of the pendulum gives interaction with the steep, undisturbed front of the breaking wave. The waves that break at 1 m and 1.5 m before the position of the pendulum have already overturned when reaching the pendulum and are therefore an examples of aerated wave interaction with the pendulum.

Figure 3.1 shows three of the ten components that we used to generate the breaking waves, with a windowing function that ramps the signal up and down so that

discrete wave groups are created. In this way, wave breaking near the wave board is prevented, which reduces the variability of the unbroken free surface signal at wave gauge 1. The wave lengths (or, equivalently, periods) of the components were selected in such a way that ramp-down of a shorter component overlaps with the ramp-up of a longer component. The wave lengths of the components in ascending order are $\lambda_i = (1.00, 1.10, 1.25, 1.45, 1.70, 2.00, 2.40, 2.90, 3.60, 5.00)$ m. The amplitudes of the wave components were found by giving each wave component a maximum steepness $H_i/\lambda_i = 1/50$, with H_i the wave height of the component. For this steepness the wave propagation of an individual component can reliably be predicted with linear theory. Wave components with lengths lower than 1.00 m or with a steepness higher than 1/50 give significant variability (with the wave maker in our tank) and wave lengths longer than 5 m with this steepness were limited in amplitude by the maximum stroke of the wave board.

The window function has two benefits and one downside, beside the fact that it prevents wave breaking near the wave board. First, it limits the stroke of the wave maker as not all components have to be generated at the same time. Second, it minimizes early nonlinear interactions because the wave groups themselves have a small steepness and only add up and interact near the pendulum. It means little difference between the linear group and phase velocity and what is obtained in the tank. Practically this means that the location of focus location can be reliably predicted. The downside of windowing is however that the ramp up and down introduces additional, mostly shorter, wave components, causing the wave group to loose energy along the way. Altogether, this means that although location of where the wave components converge is well predicted, but that the obtained surface elevation is lower than the sum of the amplitudes of the wave components. For the wave focussed at $f = 0.0$ m we can confirm that the measured maximum surface elevation is lower than the expected maximum.

The window function can be described as follows. It linearly ramps up the surface elevation of a component from 0 to the desired maximum surface elevation over a single wave period by means of a negative cosine function with twice the period and a shifted mean. Then the window function equals 1 for the duration of two wave component periods before ramping the surface elevation down again over one wave component period. The phase shift of a component is chosen such that the middle full-height peak of this four-period window for each wave component arrives at the focus location f at time $t = 0$. Then the window functions are moved back in time with the group velocity over the distance between the pendulum and wave maker to know when the wave maker should start generating these components with the appropriate phase and amplitude.

3.1.3 Reduced-order model

In addition to the experiment, a reduced-order model is employed to predict the response. The reduced-order model can be used to determine what the dominant force components are in the interaction between breaking wave and pendulum. In

[13] the reduced-order model is found to compare well to experimental results for interaction of the pendulum monochromatic waves. Here we use the same model for the interaction with breaking waves, with the same structural coefficients and the same hydrodynamics coefficients as in the setup with monochromatic waves.

The reduced-order model is based on the equation of motion of the pendulum:

$$I\ddot{\theta} + c\dot{\theta} + k\sin\theta = M \tag{3.1}$$

with pendulum angle θ, moment of inertia I, damping coefficient c and stiffness k. The external moment due to wave loading is denoted by M. M is defined as:

$$M = \beta F_m L\cos\theta \tag{3.2}$$

with L the distance between the fulcrum and the center of the tube and F_m the Morison force [74]:

$$F_m = \rho\left(C_m V a + \frac{1}{2}C_d A|u|u\right) \tag{3.3}$$

containing the density of the water ρ, submerged volume V, frontal area A, and the relative velocity u and relative acceleration a. The coefficients for added mass $C_m = 1.0$ and drag $C_d = 2.0$ are similar to [86]. This leaves only β to be defined: it is the wetness parameter of the tube, introduced by [13], denoting how far the pendulum is submerged:

$$\beta = \max\left(\min\left(\frac{\eta - (z_p - D/2)}{D}, 1\right), 0\right) \tag{3.4}$$

with D the tube diameter, η the wave elevation and z_p the instantaneous vertical position of the center of the tube with respect to the mean free surface, defined as $z = 0$. This model is integrated over time using a Runge Kutta 2 scheme with $dt = 0.05$ s, which gives a numerical error smaller than the calibration error of the potentiometer, even after 7 full periods of free vibration [13].

The Morison equation with the wetness parameter requires the fluid height, fluid velocity and fluid acceleration at the instantaneous position of the tube center. The surface elevation signal measured at wave gauge 2 is transformed to its Fourier components, with a complex amplitude. The amplitudes and phases are used in linear potential wave components (Airy wave components) to determine the velocity and acceleration amplitude vectors per component at the instantaneous position of the center of the tube, after which the complex velocity and acceleration amplitude vectors are transformed back to time signals. Note that constant extrapolation is used for the velocities and acceleration above the mean free surface at z = 0. We consider this a linearization of the fluid potential around the position of wave gauge 2, because linear potential wave theory is used to extrapolate the fluid velocities and accelerations to the instantaneous horizontal and vertical position of the tube center.

3.2 Results and discussion

In the experiment, the focus location of the wave components and the clearance of the bottom of the pendulum with respect to the mean free surface is varied. The amplitudes of the wave components are not varied between tests; the wave system therefore always has the same energy content. The response of the pendulum is measured in degrees of rotation as a function of time and the maximum deflection can serve as a measure of the impulse exerted by the breaking wave on pendulum.

According to [80], breaking waves can have a higher front velocity compared to non-breaking waves, leading to a higher maximum force. The presence of entrained air, on the other hand, can have a cushioning effect that reduces the force peak. It takes time and distance for a focused wave to overturn. Varying the distance between the focus location and the location of the pendulum, therefore, varies the interaction between the pendulum and the breaking wave in different stages of development. The focus location at the position of the pendulum will lead to unbroken wave interaction with the pendulum and no air entrainment, whereas the focus location farthest away from the pendulum will lead to interaction with a broken wave having entrained air.

The fluid velocities are largest near the crest of the breaking wave. Therefore, raising the pendulum by increasing the clearance between the bottom of the pendulum and the mean free surface, exposes the pendulum to higher fluid velocities, with a larger maximum force. On the other hand, the wave is also narrower near the crest than below, so that the time over which the pendulum is exposed to the wave is shorter.

The following shows how changing the focus location changes the free surface elevation at the location of the pendulum and how that affects its response over time and its maximum response. It also shows how changing the clearance changes the response. We will discuss 7 different configurations of focus location and clearance; for each configuration 5 repetitions were performed to investigate the variability. A configuration is addressed by the test number of its first test.

3.2.1 Qualitative analysis

Figure 3.2 shows a snapshot of a wave impact for each configuration taken with the high-speed camera from the side, just before the pendulum starts to move. The pendulum's interaction with the wave in the different configurations is described below. The focus location f in the description is given in meter with respect to the position of the pendulum (negative means opposite to the direction of wave propagation). The clearance c is given in meter with respect to the mean free surface (more positive means further away from the free surface). In order of increasing distance between pendulum and focus location:

- series 500, $c = 0.05$, $f = 0.0$: steep wave, no breaking;

- series 505, $c = 0.05, f = -0.5$: steep wave, onset of breaking, pendulum low;
- series 605, $c = 0.10, f = -0.5$: steep wave, onset of breaking, pendulum near crest;
- series 510, $c = 0.05, f = -1.0$: overturning has started, pendulum low;
- series 600, $c = 0.10, f = -1.0$: overturning has started, pendulum near crest;
- series 515, $c = 0.05, f = -1.5$: overturning with jet re-entry and mixing, air entrainment, pendulum below aerated zone;
- series 600, $c = 0.10, f = -1.5$: overturning with jet re-entry and mixing, air entrainment, pendulum in aerated zone.

The wave interaction with the pendulum is analyzed later in terms of the front velocity upon impact, the front angle or orientation of the free surface upon impact, and the wave height. The amount of air present in the water upon impact is not quantified.

3.2.2 Free surface at the position of the pendulum

In Figure 3.3 we see the free surface at the position of pendulum, measured with the second wave gauge WHM2, for all configurations. The time signal of the focused wave components at the focus location is designed to be symmetrical with respect to the maximum free surface elevation, with lower waves on either side. The realisation in the tank still features most of that design. Note that the focus location only coincides with the position of the pendulum for configuration 500. For the other 6 configurations, the wave gauge is farther away from the wave board than the focus location. The first two wave crests in the time signals pass underneath the pendulum without touching it. The third crest makes an impact with the tube of the pendulum, after which the remaining crests pass underneath without engaging with the pendulum anymore. There is one impact event per test.

In anticipation of the reduced-order model results, Figure 3.3 also shows the Fourier reconstruction of the signal when truncated to 40 Hz. Wave components above that frequency would have a wave length of 1 mm, which is thought to be beyond the measurement accuracy of the setup. The reconstructed signal is identical to the measured signal except for an almost imperceivable difference (1 mm) near the peak.

Compared to Figure 3.3, Figure 3.4 gives a more detailed representation near the peak of the free surface as a function of time, together with the free surface measurements from processing the last 25 camera images before the pendulum starts to move. The processing involved a Sobol filter to highlight edges in the images, the free surface being the brightest edge, after which a 7^{th} order polynomial was

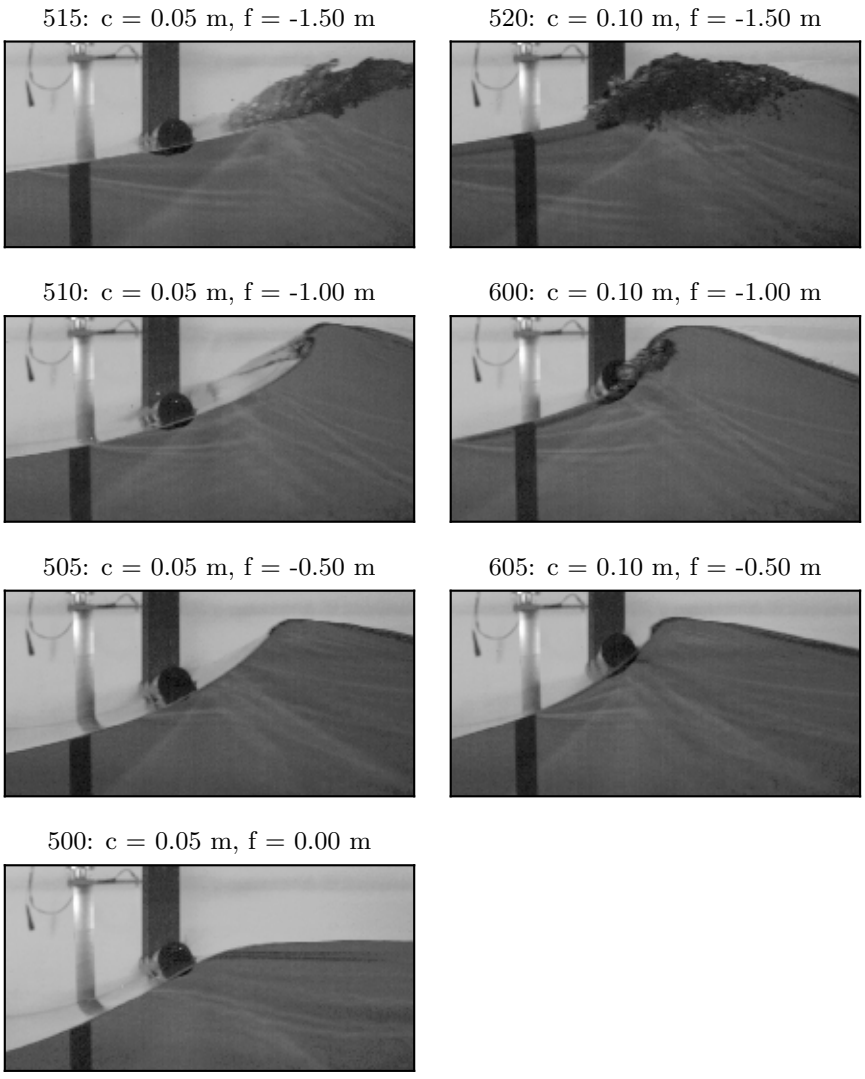

Figure 3.2: Snapshot of free surface just before the pendulum starts to move with c as clearance between the bottom of the pendulum and the mean free surface and f as focus distance with respect to the pendulum (negative is towards wave maker).

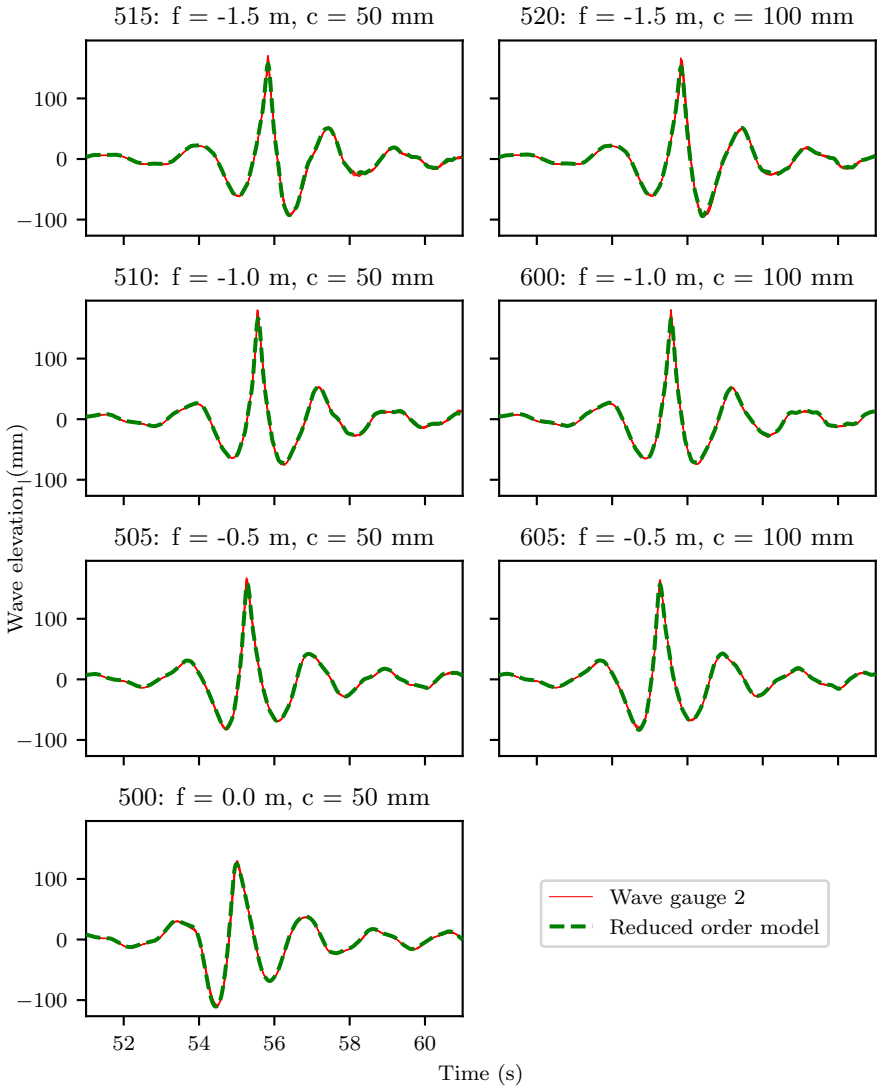

Figure 3.3: Surface elevation over time at the position of the pendulum (wave gauge 2); the reconstructed signal intended as input for the reduced-order model is compared to the experiment

fitted through the free surface. The differences in free surface between different realisations of a configuration were generally small. The free surface from the images also compares well to the signal from the wave gauge, but not for configuration 520. Here, the five different realisations give different results that are also dissimilar from the wave gauge signal. Upon careful inspection we find that also the wave gauge signals for the 5 realisations of configuration 520 are dissimilar from each other near the peak. Series 510 and 520 feature waves with a lot of mixing compared to the other series and with air entrainment. We now have to ask the somewhat philosophical question of what "free surface" means in a measurement with a resistive wave gauge in a water-air mixture. The free surface in the images appears to be less ambiguous: it is simply the dividing line between what can be considered air on the one side, and every mixture of water and air on the other. In any case it is clear that the realisations of waves with developed mixing regions and a high air content, such as for configuration 520, are different from each other, much more than before re-entry and mixing.

Figure 3.5 shows the free surface as a function of position at the time instant just before the pendulum started to move. The free surface is reconstructed from the image for that time, and also for 20 ms and 40 ms before that time to show the evolution of the free surface. The elevation measured by the wave gauge is also indicated at the position of the wave gauge for the time of impact. There is agreement between the free surface from the images and the wave gauge for all configuration, except for configuration 520. Here the wave gauge measurement of the free surface for the water-air mixture is different from what is detected in the images. Note that the different realisations for configuration 520 in space are not that dissimilar from each other. The differences only become larger in the last 5 cm before the position of the pendulum.

Figure 3.5 also shows the reconstruction of the free surface as a function of position, that is obtained from the complex amplitudes of the Fourier transform of the time signal of wave gauge 2, together with the wave numbers resulting from the linear dispersion relation. The reconstruction gives a reasonable impression of the wave shape, but is clearly not a good quantitative estimate of the position of the free surface. Linear wave theory is used far beyond the range of validity of the expansion around the mean free surface, and because many of the wave components in the Fourier transform are not linear and independent, but rather nonlinear coupled components. This already gives some account of the expected accuracy of the reduced-order model.

3.2.3 Maximum pendulum response

Figure 3.6 provides a summary of all interaction events between the pendulum and the breaking waves. Again, the vertical axis shows the maximum response angle θ of the pendulum, which is a measure of the impulse exerted on the pendulum. Three horizontal axes show: the front velocity upon impact v, the front

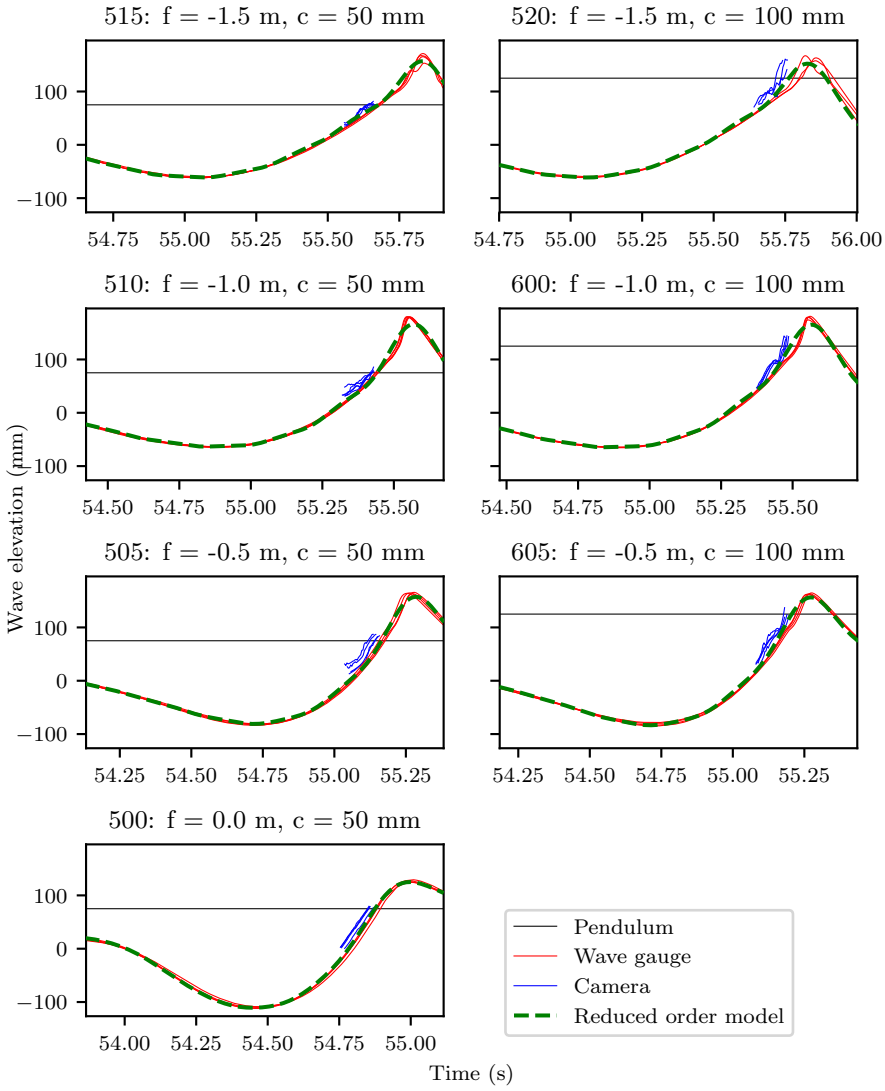

Figure 3.4: Surface elevation over time at the pendulum close to the moment of impact with the breaking wave; measurements of wave gauge 2 are compared to the surface elevation detected in the camera images.

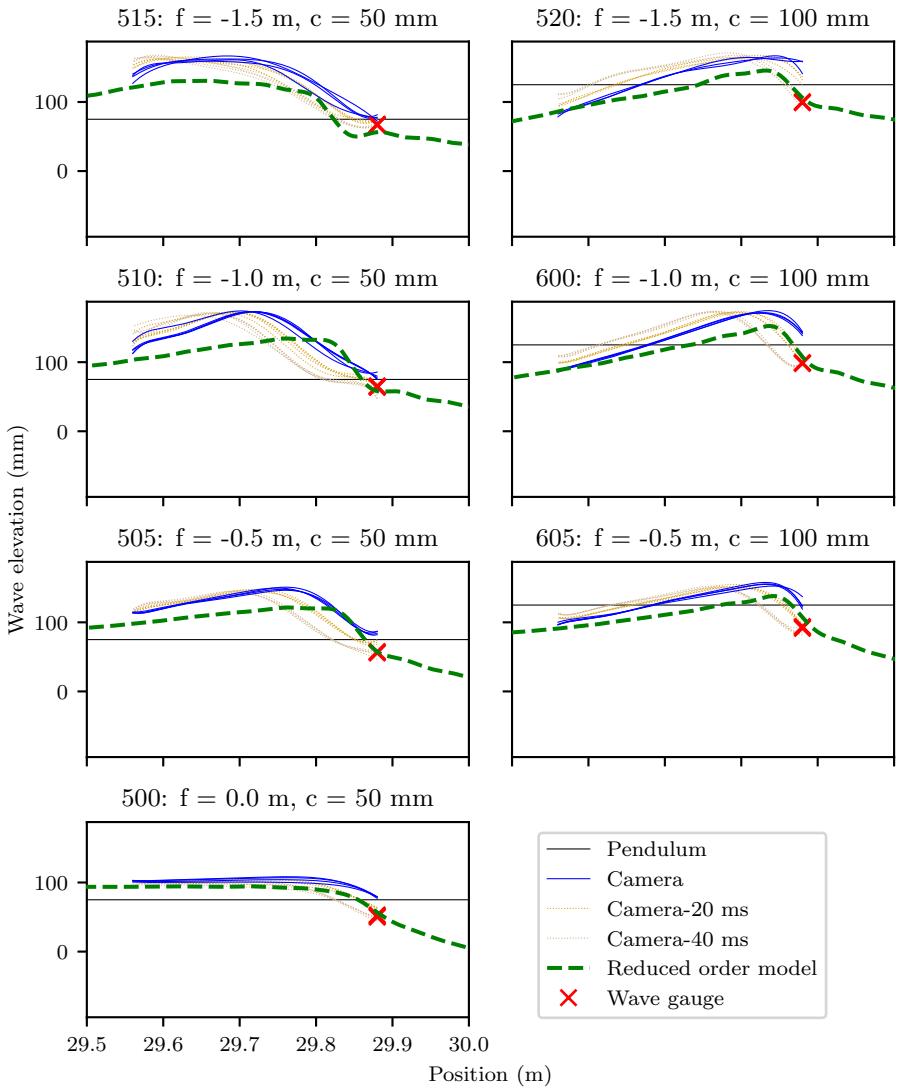

Figure 3.5: Surface elevation as a function of position close to moment of impact with the breaking wave; free surface reconstruction intended for the model is compared to the free surface from the camera image before pendulum motion is detected.

angle upon impact α, and the maximum surface elevation η measured at wave gauge 1 and 2. The front velocity and the front angle are determined from the camera images. The moment of impact is determined as the time instant of the image just before the pendulum starts to move. There were some difficulties determining the front velocity and front angle in configuration 520 in which a lot of air is present just below the interface. In these cases the last unambiguous measurement was used, which was 20 ms before impact in one case and 40 ms before impact in another.

The tests with configurations 515 and 520, involving the mixing and the air entrainment, gave the largest pendulum response. They also show the largest spread in the pendulum response. The pendulum response for the other configurations is more clustered. From series 515 it appears as if the largest front velocity correlates with the largest pendulum response. From series 510 on the other hand, it appears as if the maximum pendulum response has no relation with the front velocity at all. From series 520 it appears as if the largest front angles (steepest wave front) correlate with the largest pendulum response, but from series 515 it seems that the larger pendulum response correlates with a lower front angle. The largest surface elevation measured at wave gauge 2 (at the position of the pendulum) does not coincide with the largest pendulum angle, and from series 500 we find that a surface elevation that was on the low side of what was measured, can lead to a larger pendulum response than the highest surface elevations measured for series 600. Unlike all other configuration, series 500 with the unbroken wave, has a straightforward relation with the maximum pendulum response: the variability of the surface elevation is immediately transferred to a variability of the pendulum response. The variability at wave gauge 2 is due to the wave components converging near the pendulum and the subsequent nonlinear exchange of energy between components, because hardly any variability in the surface elevation is present at wave gauge 1. The variability for series 515 and 520 is most likely due to mixing and air entrainment.

Table 3.1 presents an overview of the average value of the main parameters, together with its coefficient of variation (cov, standard deviation over average value). The average value of the maximum pendulum response is largest for configuration 600, with the developed mixing zone and the air entrainment. The cov of the maximum pendulum response is larger for both configurations with the mixing zones and the air content, than for the other configurations. Table 3.1 does not reveal a clear trend for the average value of maximum pendulum response versus the average values of any of the other parameters. There is a clear trend for the cov: when the cov of the surface elevation is larger, then also the cov of the maximum pendulum response is larger. When the cov of the surface elevation is lower, then also the cov of the maximum pendulum response is lower. The cov of the maximum pendulum response is always larger than the cov of the maximum surface elevation. Similar trends for the coefficients of variation of the other parameters could not be identified. It is special for this system with a degree-of-freedom that there is variability of the global response at all and, hence,

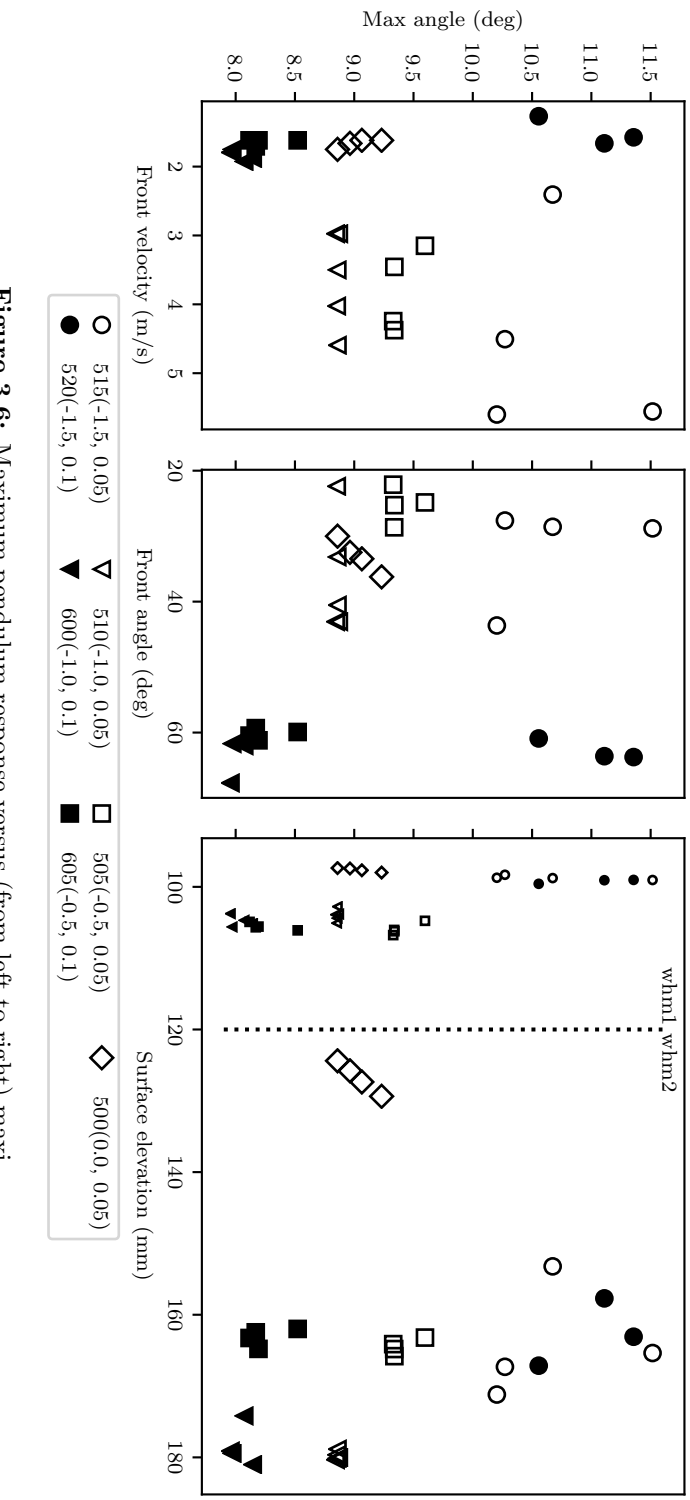

Figure 3.6: Maximum pendulum response versus (from left to right) maximum front velocity v, front angle α and surface elevation η at wave gauge 1 and 2.

of the impulse. Studies with similar breaking waves and rigid walls have shown that although differences in local pressures were measured between repetitions, the total impulse was approximately constant [47, 17].

We expected a stronger correlation between the maximum pendulum response on the one hand, and the three parameters front velocity, front angle and surface elevation on the other. An explanation for the absence of such a correlation with the front velocity and the front angle can be that the impact force, although large, has a short duration compared to time that the tube of the pendulum is submerged. The absence of a correlation between the average maximum surface elevation and the average maximum pendulum response cannot be explained in this way, because of the following effects. A higher wave has higher fluid velocities that will lead to a higher drag force. And on many occasions the increased surface elevation also means that the pendulum is submerged and exposed to drag for a longer time. These effects are considered in more detail in the next section where the results of the reduced-order model are presented.

Note that a few other things were tried to achieve any correlation between the different results. Based on the Wagner impact theory, a relation was sought between the front angle and front velocity of the impact, taking only the force component perpendicular to the pendulum. Also, squaring or cubing the front velocity was tried, to get the correlation with total impulse or load rise rate. Finally an energetic point of view was investigated, which was dropped not only because no significant relation was found. When comparing the interacting pendulum to an idealized setup where only force on the tube would be measured, then in the latter case there would be no energy transfer. Hence, it makes more sense to compare the results from a momentum point of view, since the motion of the structure is not involved.

3.2.4 Reduced-order model results

From the summary of the experimental results it was found that wave front velocity and front angle do not show a strong correlation with the maximum pendulum response. A reduced-order model was presented above that does not include the wave impact force, but does include the transition from dry to wet, the submerged exchange of momentum and the transition from wet to dry. Note that the surface elevation signal of wave gauge 2 at the position of the pendulum was transformed to linear Fourier components and that the complex amplitude of these components was used to reconstruct a fluid velocity and fluid acceleration at the instantaneous position of the center of the tube by means of linear Airy theory. Velocity and acceleration are input to computing the force with the Morison equation. Figure 3.7 shows the different components of the computed force for the different configurations. It is immediately clear that the total force on the pendulum is dominated by drag. For the same breaking waves (focus location the same), the maximum absolute force on the tube is higher when the clearance is smaller. The duration of the force is also longer when the clearance is smaller. Considering especially

Table 3.1: Summary of the test results, ordered by focus location f and clearance c. Average (avg) and coefficient of variation (cov, standard devation over average) is presented for maximum pendulum angle θ (°), maximum wave elevation η (mm) at wave gauge 2, front speed v (m/s) and front angle α (°).

(f, c)	avg θ	cov θ	avg η	cov η	avg v	cov v	avg α	cov α
515(-1.5, 0.05)	10.7	5.66e-02	1.64e+02	4.72e-02	4.52	3.31e-01	3.22e+01	2.39e-01
520(-1.5, 0.1)	11.0	3.72e-02	1.63e+02	2.91e-02	1.50	1.38e-01	6.28e+01	2.56e-02
510(-1.0, 0.05)	8.86	1.11e-03	1.80e+02	3.27e-03	3.61	1.94e-01	3.64e+01	2.43e-01
600(-1.0, 0.1)	8.04	1.10e-02	1.78e+02	1.66e-02	1.84	4.35e-02	6.30e+01	5.15e-02
505(-0.5, 0.05)	9.40	1.39e-02	1.64e+02	6.69e-03	3.81	1.57e-01	2.52e+01	1.06e-01
605(-0.5, 0.1)	8.25	2.23e-02	1.63e+02	7.51e-03	1.64	2.67e-02	6.02e+01	1.32e-02
500(0.0, 0.05)	9.03	1.75e-02	1.27e+02	1.69e-02	1.66	3.72e-02	3.30e+01	7.78e-02

the left column of Figure 3.7, for the smaller clearances, we may now also have an explanation why there is no direct correlation between the maximum surface elevation and the maximum pendulum response. The motion of the pendulum is counteracted by a force in the other direction. When the maximum surface elevation becomes larger, also the counteracting force becomes larger and longer in duration.

Figure 3.8 compares the results of the reduced-order model for the pendulum response as a function of time with the pendulum response that was measured in the experiment. The time signal shows the pendulum being exposed to the breaking wave, followed by a free vibration. The difference between the reduced-order model result and the experiment is particularly small for configuration 500, with the non-breaking interaction with the pendulum. Although the wave front for configuration 500 in Figure 3.2 is rather steep, the reduced-order model with a local linearization of the flow field is a good approximation of the experiment with a difference near the maximum response of less than 1%. For configurations 505 and 605, the breaking wave is at the onset of overturning. The reduced-order model overestimates the response compared to the experiment with a difference of less than 10% for both configurations. It is interesting that the difference with the experiment is the same for 505 and 605, because the distance between the mean free surface and the center of the tube is larger for 605. Before seeing the results, we thought that the constant extrapolation of velocities above the mean free surface in the model would turn out worse for 605 than for 505. But it does not. The breaking wave has started overturning for configuration 510 and 600. In these configurations, the difference between the reduced-order model and the experiment is largest and too large to be called a good approximation. It is, however, a conservative estimation of the pendulum response. The reduced-order model for 510 overestimates the maximum response of the pendulum by 12%. For 600, the overestimation of the pendulum is response is close to 20%. Here, we do see that the difference between model and experiment increases when the clearance is increased, which could be the results of using constant extrapolation of the velocities and accelerations above the mean free surface.

What is unexpected is that the reduced-order model overestimates the maximum response; beforehand we would have estimated that the fluid velocities in a steep nonlinear breaking wave would be larger than those obtained from a linear approximation of the flow field in such a wave. The experiments for configurations 515 and 520, finally, have the most complex flow field with a developed mixing zone and some air content. The reduced-order model has less than 3% difference in the maximum pendulum response for 515 and 5% difference for 520. Where for the other configurations the reduced-order model overestimates the maximum pendulum response, it gives an underestimation of the maximum response for 520. From Figure 3.6 it was found that the mixing zone and the air content caused a comparatively large variability of the maximum pendulum response, but for 515 and 520 the reduced-order model is a good approximation of the experimental results on average. Overall, the reduced-order model gives a good account of the

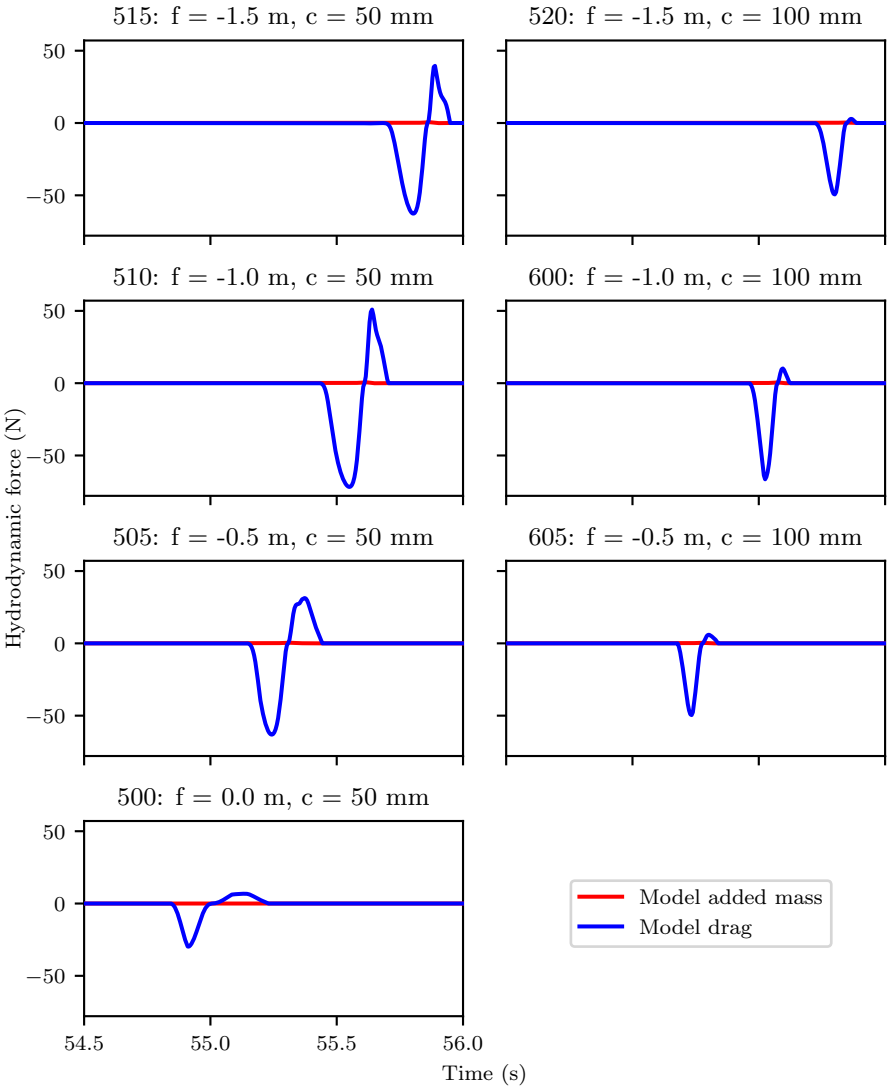

Figure 3.7: Reduced-order model approximation of the force on the pendulum in a breaking wave for the different configurations of focus location and tube clearance (negative force is in the direction of wave propagation)

changes in maximum pendulum response for the different phases of wave breaking that we enforced by changing the focus location of the wave components, and for the different elevations of the tube of the pendulum with respect to the mean free surface.

3.3 Conclusions

A 2D benchmark experiment for structural deformation in extreme waves was performed by measuring the response of a one degree-of-freedom pendulum with a tube at the base in focused breaking waves. The experiment varied the focus location with respect to the position of the pendulum and the initial vertical clearance between the bottom of the tube and the mean free surface.

The energy in the wave was the same for all tests. The response of the pendulum varied greatly with focus location and initial vertical clearance. It was found that the wave in this data set breaking farthest away, with the pendulum at its highest elevation caused the largest response. The wave front velocity and the angle of the front were determined by means of image processing of high-speed camera images. Although the largest pendulum response occurs for the largest wave front velocity, and the lowest response for the lowest wave front velocity, the maximum front velocity and angle do not correlate well with the response. The response correlates best with the surface elevation at the position of the pendulum. This was confirmed by the results of a reduced-order model that translates the surface elevation near the pendulum to a force and subsequent response corresponding well with the experimental results, without wave front velocity and angle.

The response also shows variability between experiments in which focus position and initial vertical clearance were kept the same. The variability in surface elevation is caused by the wave components converging over a small distance near the pendulum and the subsequent breaking, because the variability in the surface elevation at the first wave gauge is small and the variability in the surface elevation at the position of the pendulum is large. The variability in the response is large when mixing and air entrainment were present. Moreover, the variability of the pendulum response, was always larger than the variability of the surface elevation. The largest variability of the response was observed for the wave breaking farthest away from the position of the pendulum; it is thought that the variability is largest for this condition because here the overturning breaking wave has had the longest time to entrain air and to generate smaller flow structures. The variability in the total response, and hence the impulse, is different from what is observed in literature for breaking waves against rigid, vertical walls for which local pressures in similar wave impacts show variation between tests, but the overall impulse is approximately the same.

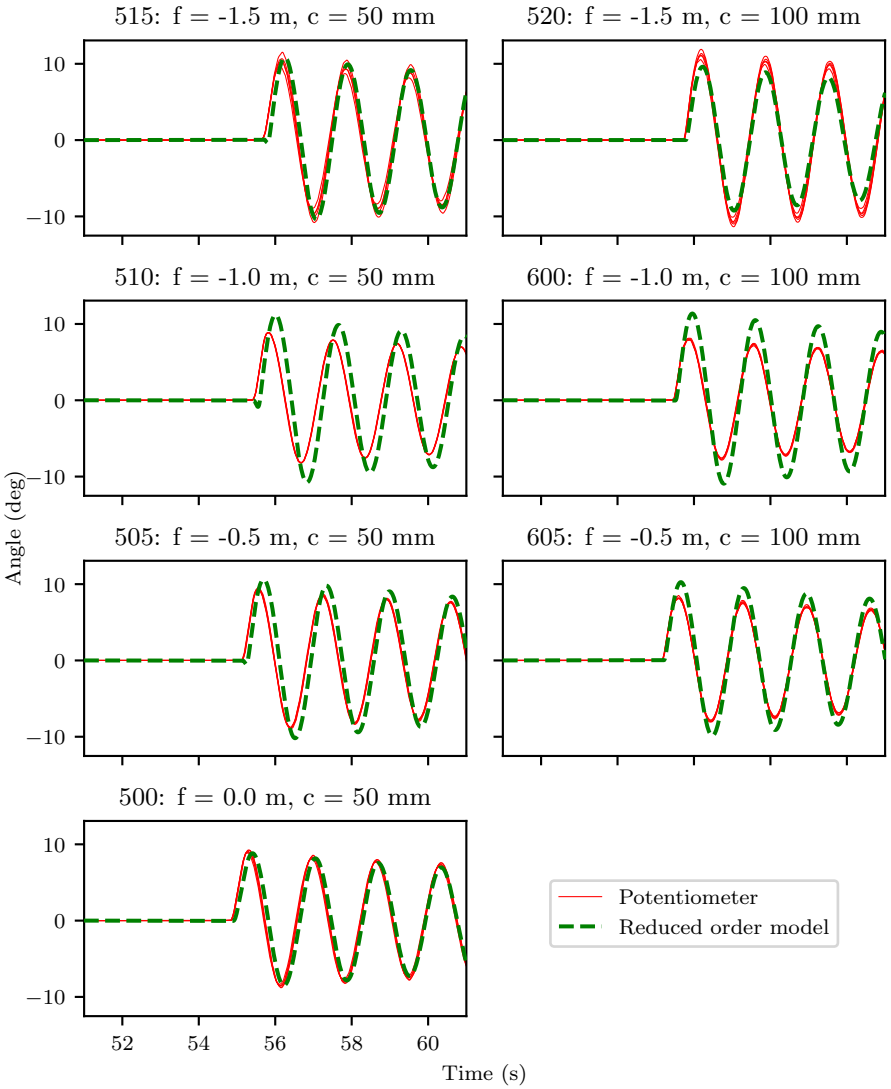

Figure 3.8: Pendulum response in a breaking wave as a function of time. Reduced-order model results are compared to the experiment

Chapter 4

A reduced order model for structural response of the Mark III LNG Cargo Containment System

Based on R.W. Bos, J.H. Den Besten, M.L. Kaminski. 'A reduced order model for structural response of the Mark III LNG cargo containment system' (2020) International Shipbuilding Progress, 66 (4), pp. 295-313.

Safe and efficient marine storage and transportation of liquefied natural gas (LNG) at -162°C requires cargo tanks providing sufficient strength and thermal insulation. At these temperatures LNG can be transported as long as the vessel's inner hull is insulated from the low temperature with a Cargo Containment System or CCS, as sketched in Figure 4.1.

The CCS experiences sloshing loads that are mainly investigated in 1:40 scale model tests, scaled up to full scale [69, 40]. Due to sensor size, the scaled loaded area is such that local flow features are lost. Scaled loads are then compared with structural capacity, while taking correction factors for operational experience into account. This procedure has allowed for safe sailing with LNG tankers for the past years.

While this method is safe, the physics were not well understood [8], leading to the Sloshel project. In this project sloshing impacts on a CCS were investigated in model and full scale [16, 53], which led to the identification of three Elementary Loading Processes (ELP) [59]:

1. Direct impact
2. Building jet

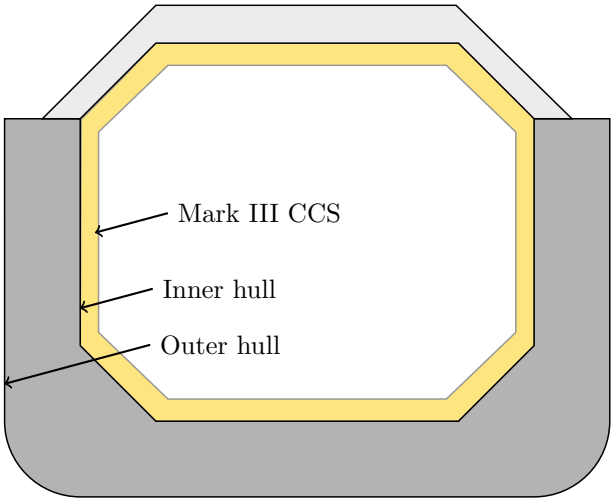

Figure 4.1: Cross section of a ship insulated with the Mark III cargo containment system.

3. Pulsating gas pocket

The physics governing these ELPs do not all follow the same scaling laws [27], and therefore the tuning of 1:40 scale pressures with operational experience is needed. Pressures measured in Sloshel were applied to a nonlinear FE model in [97]. They found that the stress in the foam contains less details than the temporal and spatial distribution of the pressures (pressure map) has. Hence, the structure filters the loads and therefore not all underlying ELPs may be relevant for the structure.

For new applications such as small scale LNG and liquid hydrogen, the same ELPs are expected. However, they will have other magnitudes. Furthermore, without the scaling factors from operational experience questions are raised about the importance of phase transition, variability, and fluid-structure interaction. The SLING project [8] investigates importance of these factors by analyzing their influence on the pressure map. A change in the pressure map does not necessarily mean that an effect is important, as demonstrated in [12]. This is determined by looking at the predicted structural damage. If omission of a factor does not change the predicted damage, then it is not considered important. Ideally all pressure maps would be investigated, to derive general conclusions and guidelines for model tests and numerical simulations, but this would be too time consuming for an FE analysis. This research is part of the SLING project and has as goal to efficiently quantify which part of the load is important for the structure. By knowing what loads are important the design of a CCS can be done more efficiently.

In this paper we take the first step towards a fast load screening method, without employing complex and time-consuming FE analysis for the large number of load cases that can be imagined. We define screening as a selection process, which results in a conservative prediction of structural damage by selecting the most damaging load cases. Screening should help to answer the question: *Which load influencing factors are important for the damage prediction of a membrane CCS?* The screening method should conservatively predict failure while being simple to apply. This led to the development of a reduced order model, which has three main advantages over FE analysis:

1. Such a model gives a stress estimate before using FE models, similar to the Euler beam theory which gives a first response estimate.

2. The model can be applied as a filter to determine which load parts are important.

3. It could be applied as fast design tool, as it gives a relation between loading, response and material parameters.

An additional use for such a screening method could be to investigate results of numerical sloshing simulations, which can deliver higher resolution results compared to model tests, such as [44, 43]. Such simulations come at high computational cost, and do not necessarily include all physics on all scales because modelling the pressure peaks requires high spatial and temporal resolution [69]. Additionally, variability of the flow is not accounted for when calculating a single impact, further increasing the cost if statistics are required.

This paper consists of two main parts. First, the reduced order CCS model is developed, starting with the assumptions used to reduce the model order and proceeding with the structural model. Second, the reduced order model response is compared to FE analysis results for a number of static load cases and a dynamic wave impact (from [59]). The paper finishes with conclusions and recommendations.

4.1 Simplified cargo containment system model

There are multiple CCS types on the market, in this paper we choose the oft-used Mark III CCS designed by Gaztransport & Technigaz. [31, 38, 49] explain the working principles behind the CCS, as shown in Figure 4.2. This insulation is made of prefabricated panels of 3 by 1 m, which rest on the inner hull using mastic ropes. The foam core insulates the tank, while the top and bottom plywood prevent local indentation either due to the impact loads at the top, or due to the supporting mastic ropes at the bottom. The primary and secondary membrane ensure gas and liquid tightness. Relaxation grooves in plywood and foam, as well as corrugations in the primary membrane, are used to reduce thermal stresses. After fixing the panels to the hull with studs, the top is made flat using insets called the 'top bridge pad', creating a flat inner tank. The primary membrane is

welded to a stainless steel anchoring strip which are fixed to the top plywood. For convenience we shall hereafter call the area between two corrugations a 'subpanel'.

Accurate response estimates have been obtained using idealized triangular loads and FE analysis, reconstructing the load from these idealized loads [56]. In early design it can be impractical to determine the response to idealized loads using an FE model. Here the reduced order model comes in. It gives an estimate of the structural stress, and therefore failure can be investigated. Two main failure modes are identified [49, 18]: indentation failure with maximum permanent deformation of the foam due to crushing, and shear failure of the bottom plywood.

From here on we will develop a reduced order model specifically for the indentation failure mode. The focus of the reduced order model is on the subpanel representing most of the tank wall. We decide to disregard the insets, studs and anchoring strips, assuming they can later be added using a stress concentration factor. Additionally, shear failure of the bottom plywood can later be added based on the deformation of the top plywood. Also, we will only investigate the linear response of the CCS. The presented model will be valid on the entire CCS excluding the corners, where the structure is different. For plastic deformation of the foam, the model of [25] can be chosen [49]. This model combines the square of the hydrostatic and Von Mises (mean and deviatoric) stress linearly to a failure locus. However, other failure laws can also be considered [51], and show a large influence on the capacity, which is why this choice is not made here.

A first idea for a reduced order model is a higher order sandwich model [37], with the plywood as face plates and foam as core. Such sandwich models are however still quite complex and do not lend themselves for a quick estimate without considerable effort. Looking at the failure mode allows further simplification as demonstrated in [75, 39, 89]. A beam-foundation models, such as the Vlasov model [95], is used to predict the combined behavior of the face plate (top plywood) and foam core. This method requires the displacement field over the height of the foundation, which can be determined with an energy minimization under static loading [90].

For highly dynamic impact loads such a minimization is impractical, as the displacement field of the foam changes in time. Instead of obtaining the displacement field of the foam by energy minimization, it is given by the first vibration mode of the CCS: the top plywood going up and down. This mode can be imagined as the top plywood moving up and down without bending. The following assumptions are made for the reduced order model:

- The displacement field over the height of the foam is similar to the displacement field of the first vibration mode, only scaled in magnitude.

- Only a short part of the bottom plywood between the mastic ropes can bend, hence the bottom plywood and mastic ropes are considered rigid.

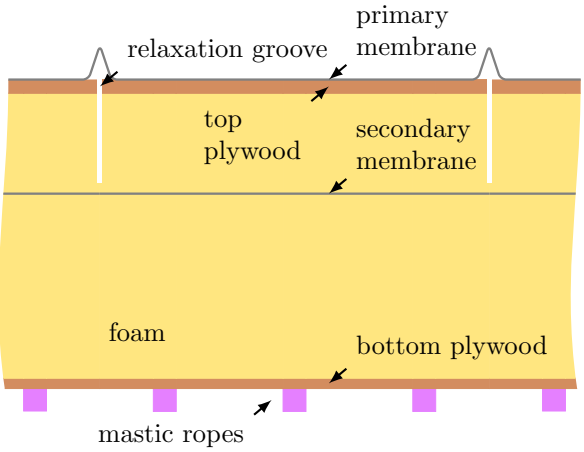

(a) Sketch of the CCS as installed on ships, repeating along the inner hull.

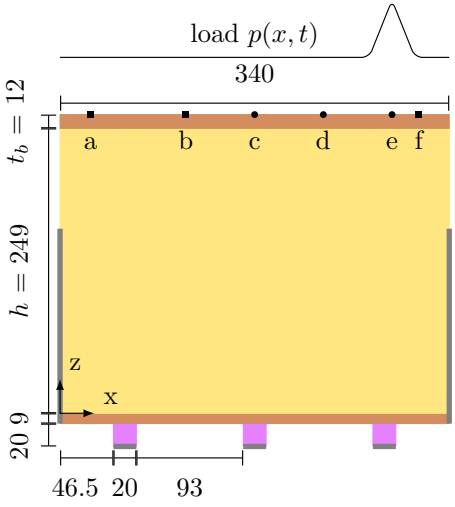

(b) Subpanel used in calculations with dimensions in mm, the dots on the top plywood indicate the pressure sensors [59] of the sloshing load case.

Figure 4.2: The Mark III cargo containment system as designed by GTT similar to [42, 58].

- The primary membrane is not included, following [49, 5]. It could be added to the bending stiffness of the beam.
- The secondary membrane of 1 mm thick is disregarded as done in [49, 5].
- The subpanel is isolated from other subpanels (relaxation groove goes all the way to the bottom).
- Anisotropic material properties and plasticity are not taken into account.

This gives a similar model to [75]. Then we can determine the stress response and boundary conditions. The effect of the first and second assumption can be asserted using the results presented later.

4.1.1 Foam displacement field

First the vibrations of a subpanel of the CCS with undeformed top plywood are determined. The foam is modelled as a bar along the subpanel thickness, with varying temperature and therefore stiffness, satisfying:

$$\rho A \frac{\partial^2 w_t}{\partial t^2} + c(z) A \frac{\partial^2 w_t}{\partial z^2} = 0 \tag{4.1}$$

with foam density ρ, cross sectional area A, elastic modulus $c(z)$ and through thickness displacement $w_t(z,t)$. The temperature distribution is assumed to be linear over the thickness (thermal conductivity is independent of temperature), hence $c(z) = c_0 + c_1 z$, interpolating between the 'cold' and 'warm' elastic modulus from Table 5.1.

No deformations are allowed at $z = 0$ (the bottom of the foam), at $z = h$ (the top of the foam) the mass of the top plywood is placed:

$$w_t(0,t) = 0,\ c(h) A \frac{\partial w_t(h,t)}{\partial z} = \rho_b A t_b \frac{\partial^2 w_t(h,t)}{\partial t^2} \tag{4.2}$$

where h is the foam thickness and t_b the thickness of the top plywood.

The solution $w_t(z,t)$ to Equation 4.1 is obtained using the Ritz method with a ninth order polynomial. The same analysis with the same boundary conditions is performed with an FE model. Figure 4.3 shows the mass normalized displacement field, which is equal for the reduced order and FE model. The frequencies match at 636 Hz for both models. In the following part w_t will be normalized to $\bar{w}_t$ by:

$$\bar{w}_t(z) = \frac{w(z)}{w(h)} \tag{4.3}$$

hence, the displacement in the foam is interpolated from the top by $\bar{w}_t$.

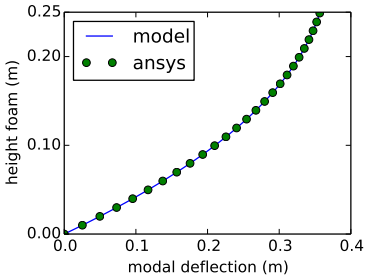

Figure 4.3: Ritz (reduced order) vs FE mass normalized displacement through the thickness of the foam, including thermal properties. Ritz (9 terms): 636 Hz, FE model: 636 Hz.

4.1.2 Top plywood response

The foam displacement field can be used in the beam-support model of [95], which is rewritten here:

$$\gamma \cdot \frac{\partial^2 w_b(x,t)}{\partial t^2} + \frac{\partial^4 w_b(x,t)}{\partial x^4} - \mu_s \cdot \frac{\partial^2 w_b(x,t)}{\partial x^2} + \mu_k \cdot w_b(x,t) = \frac{p_b(x,t)}{D} \tag{4.4}$$

where a 'unit' width of the system in y direction is disregarded. The entire equation is divided by the flexural stiffness of the top plywood in cylindrical bending, making it behave like a beam with: $D = E_b \frac{t^3}{12(1-\nu^2)}$. The coefficients are:

$$\gamma \cdot D = \rho \int_0^L \bar{w}_t^2(z,t)dz + \rho_b t_b \tag{4.5}$$

$$\mu_s \cdot D = \frac{1}{2(1+\nu)} \int_0^L E(z)\bar{w}_t^2(z,t)dz \tag{4.6}$$

$$\mu_k \cdot D = \frac{(1-\nu)}{1-\nu-2\nu^2} \int_0^L E(z) \left(\frac{\partial \bar{w}_t(z,t)}{\partial z} \right)^2 dz \tag{4.7}$$

with ρ and ρ_b as foam and top plywood density respectively and ν as Poisson ratio of the foam. Physically, γ is the top plywood mass combined with weighed participation of the foam. The shear stiffness of the foundation is represented by μ_s, the compressive resistance of the foam is given by μ_k. The total displacement field in the foam is described by $w(x,z,t) = \bar{w}_t(z)w_b(x,t)$: a product of the normalized through thickness displacement and the deformation of the top plywood.

4.1.3 Stresses at top and bottom of foam

When the deformation is known, the vertical stresses σ_z can be determined. The contact normal stress between the foam and plywood is obtained by subtracting

the beam from the foundation. The beam satisfies:

$$D\frac{\partial^4 w_b}{\partial x^4} = p_b - \sigma_z(x, z = h) \tag{4.8}$$

where w_b is the deformation of the beam, p_b the pressure at top of the beam and $\sigma_z(x, z = h)$ the stress at bottom of the beam. Combining this with Equation 4.4 yields:

$$\sigma_z(x, z = h) = D\left(\mu_k w_b - \mu_s \frac{\partial^2 w_b}{\partial x^2}\right) \tag{4.9}$$

and the bottom stress is predicted by looking at the vertical strain ϵ_z at the bottom of the foam. We know $\epsilon_z = \partial \bar{w}_t / \partial x$, resulting in:

$$\sigma_z(x, z = 0) = D\mu_k \cdot w_b \tag{4.10}$$

For the horizontal stress σ_x is determined using the stress-strain relation from [75], who assumes the foam has no displacement field in horizontal direction, hence there is no strain in this direction:

$$\epsilon_x = \frac{\sigma_x}{E} - \nu\frac{\sigma_z}{E} = 0 \tag{4.11}$$

and therefore the horizontal stress $\sigma_x = \nu\sigma_z$. The same procedure may be followed to investigate horizontal stress at the bottom of the foam, and for the stress in the thickness $\sigma_y = \sigma_x$.

Following our kinematics the following shear stresses are obtained [75]:

$$\gamma_{xz} = \frac{\partial w}{\partial x} = \bar{w}_t \frac{\partial w_b}{\partial x} \tag{4.12}$$

$$\tau_{xz} = \frac{1}{2(1+\nu)} E(z)\gamma_{xz} \tag{4.13}$$

which vanishes at the bottom: $\tau_{xz}(x, z = 0) = 0$, due to the boundary condition at the bottom $w_t(x, z = 0) = 0$.

In the following the σ_z stress at the top is compared for the reduced order and FE model. As seen here, the other stresses are derived from this stress and the displacement. Also, the other stress components are expected to be much smaller.

4.1.4 Boundary conditions and solution

The relation between top and bottom normal stress and total shear force of the foam can be determined, by requiring the total force equilibrium on the foam to be zero, over a certain portion of the beam $a \leq x \leq b$:

$$0 = \int_a^b \int_0^h \frac{\partial \sigma_z}{\partial z} + \frac{\partial \tau_{xz}}{\partial x} dz dx \tag{4.14}$$

$$= [Q(x)]_a^b + \int_a^b \sigma(x, z = h) - \sigma(x, z = 0) dx \tag{4.15}$$

which has to hold regardless of a, b. Therefore the shear force on a cross-section of the foam is:

$$Q(x) = -D\mu_s \frac{\partial w}{\partial x} \tag{4.16}$$

By looking at the relaxation grooves in Figure 4.2, the beam should be considered free, whereas the foam is elastically restrained up to approximately halfway its thickness. These boundary conditions can be realized by enforcing the sum of shear force in the beam and the foam to be zero, hence:

$$Q_{\text{end}} = D\left(\frac{\partial^3 w}{\partial x^3} - \mu_s \frac{\partial w}{\partial x}\right) = 0 \tag{4.17}$$

Additionally, the moment at the end of the beam is zero:

$$M_{\text{end}} = D\frac{\partial^2 w_b}{\partial x^2} = 0 \tag{4.18}$$

The aforementioned boundary conditions can be thought of as a free beam with an end spring, coupling rotation with shear. Hence there is a concentrated contact load between the beam and foam at the free ends, comparable to free-edge effects in laminates [73].

A static solution is obtained by setting $w_b(x,t) = w_b(x)$ and $p_b(x,t) = p_b(x)$, loosing the inertial part. A fourth order ordinary differential equation is the result of which the roots can be found. The particular solution can for instance be found for linear pressure distributions $p_b(x) = p_0 + p_1 x$:

$$w_b = \frac{1}{\mu_k D} \cdot (p_0 + p_1 x) \tag{4.19}$$

Then coefficients of the exponential functions are used to match the boundary conditions.

A modal solution is found by applying separation of variables. Substitute $w(x,t) = X(x)T(t)$ into the partial differential equation, and bring all time dependent parts to one side, space dependent to the other:

$$-\gamma \frac{\partial^2 T}{\partial t^2} = \frac{\partial^4 X}{\partial x^4} - \mu_s \frac{\partial^2 X}{\partial x^2} + \mu_k = \alpha \tag{4.20}$$

The aim is to solve the spatial ordinary differential equation:

$$\frac{\partial^4 X}{\partial x^4} - \mu_s \frac{\partial^2 X}{\partial x^2} + (\mu_k - \alpha)X = 0 \tag{4.21}$$

which is most convenient if $\mu_k - \alpha = 0$, meaning $X = c_0 + c_1 x$. These are the two rigid body modes: up-down and rotation of the beam; the latter drops out because of the boundary condition in Equation 4.17. The natural frequencies are

found by substituting $\alpha = \mu_k$ into the time equation. Then we find that the natural frequency of the rigid body mode of the beam is:

$$\omega_0^2 = \frac{\mu_k}{\gamma} \tag{4.22}$$

which is analogous to taking the foundation as spring, and the beam with part of the foundation as mass. Hence, this results in the same natural frequency as described in Section 4.1.1.

For higher modes a Wronskian matrix of the boundary conditions is used. The zero values of the Wronksian determinant are determined, changing only α, which can in turn be used for the natural frequencies ω_i.

4.2 Results and discussion

In this section static and dynamic results of the reduced order model are compared with the FE calculations. A 2D model is made to represent the CCS, containing the top and bottom plywood, foam and relaxation grooves. The structure is supported from below by the mastic ropes. ANSYS© Academic Research Mechanical, Release 16.2 is used for the finite element calculations [3], with linear plane strain elements (`PLANE182`) for the top and bottom plywood as well as the foam. All displacements are measured at the interface between the top plywood and foam.

A narrow and a wide model are used, the narrow model has one subpanel, Figure 4.2, the wide model has three, with the middle one loaded. Elements of 3, 1.5, and 0.75 mm are used for the convergence in the narrow model, in the wide model 3 mm elements are used. The elements are as square as possible, an example of the wide model is shown in Figure 4.4. The material model is isotropic linear and properties are chosen after [79, 51] and similar to [78], and displayed in Table 5.1. The top plywood is free at both ends, and continuously supported by the foam.

Table 4.1: Input parameters similar to [79] (density, Poisson ratio), [51] (elastic modulus).

		Bottom (20°C)	Top (-163°C)	
Plywood	E_b	7,700	11,300	MPa
	ρ_b	680	680	kg/m^3
	ν_b (FEA)	0.3	0.3	-
Foam	E	55	105	MPa
	ρ	125	125	kg/m^3
	ν	0.2	0.2	-
Mastic rope	E	2,800	-	MPa
	ρ	960	-	kg/m^3
	ν	0.3	-	-

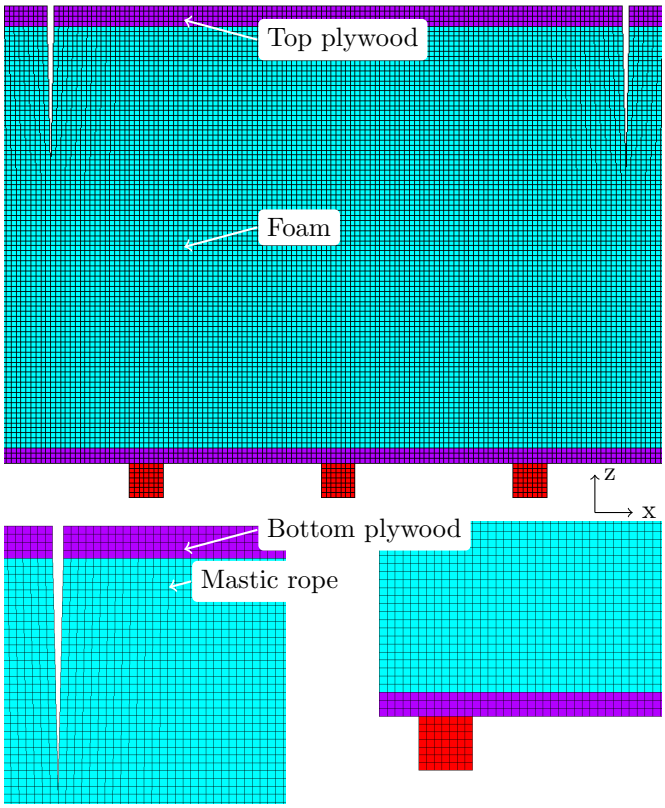

Figure 4.4: Finite element mesh of the wide model, with detailed view of the relaxation groove and mastic rope.

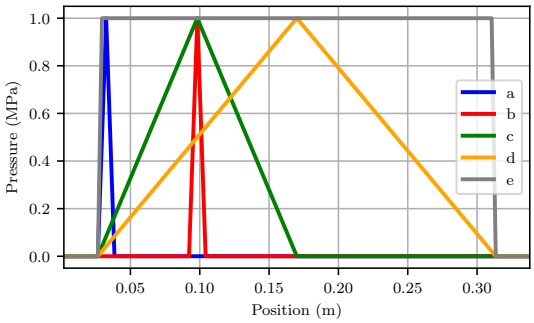

Figure 4.5: Static load cases, index corresponds to static load figures.

For all FE models the bottom of the mastic is constraint in vertical z direction. The foam and bottom plywood are constraint in horizontal x direction, as shown in Figure 4.2. Only the stress and displacement at the top of the foam are compared, other stress results can be obtained as described in Section 5.1.

4.2.1 Static response

Sloshing loads can be divided up in three ELPs [59]: (1) direct impact, (2) building jet and (3) pulsating gas pocket. The loads investigated in this section are based on these three ELPs, and one test case of measured loads. The small corrugation starts at 53/2 mm from the center of the relaxation groove [78]. Any load closer to the relaxation groove will be redistributed by the corrugation.

Five static load cases are proposed in Figure 4.5. The peak loads (12 mm wide) represent direct impacts and building jets in the corner of the corrugation and at about one third of the width. A wider peak (143.5 mm wide) is applied at one third of the panel. Between the corrugations a triangular and uniform loading are applied, representing a wide pressure caused by, for instance, entrapped gas or hydrostatic load. All loads have a maximum of 1 MPa, to easily compare their effects. We believe that these loads show clearly the advantages and limitations of this model regarding spatial accuracy, even though they do not vary in time. In fact, it is easier to investigate the spatial accuracy with a static model, because there is only one time step to compare.

After application of the loads in Figure 4.5, the following figures are obtained. Figure 4.6 shows the static displacement at the top of the foam, and Figure 4.7 compares the vertical displacement field in the foam between the reduced order (line) and reference solution (colored). These can be compared by looking at the shape and closeness of the lines: closer lines denote a larger strain.

With respect to the reference solution, the narrow model consequently overestimates displacement, as the boundaries of the foam are free to move vertically

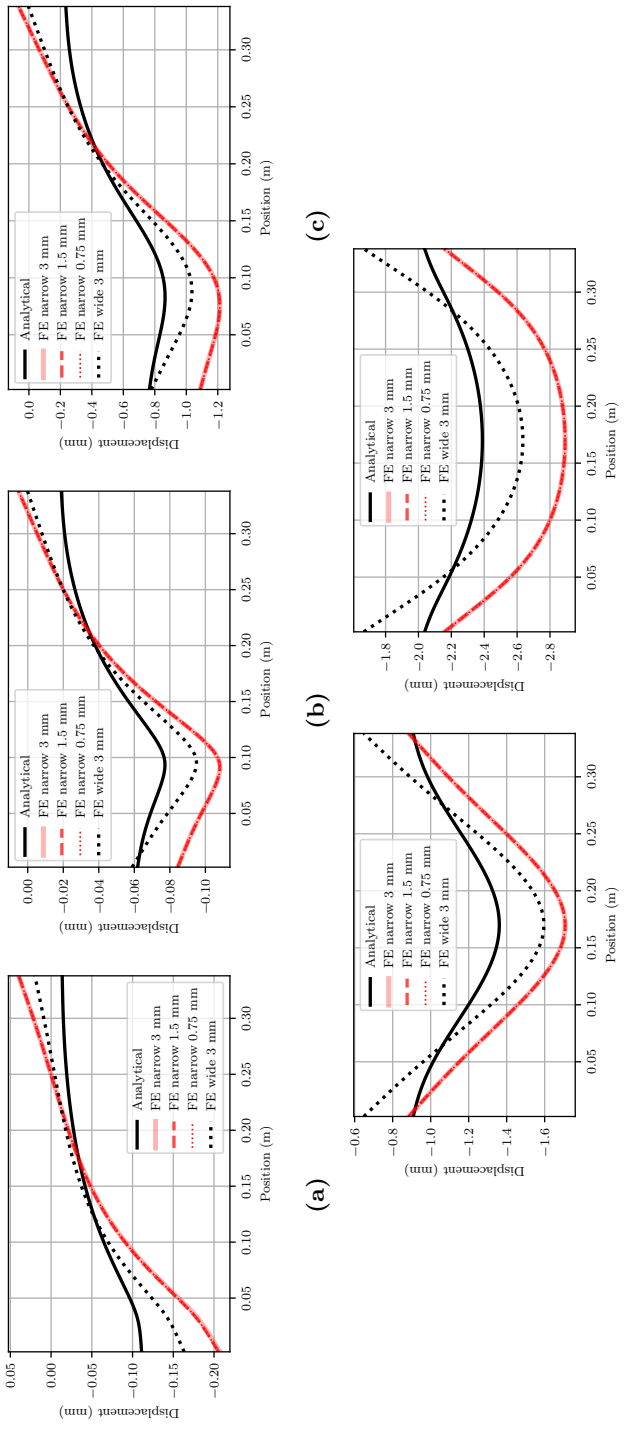

Figure 4.6: Displacement for static loads, subplots correspond to the lines in Figure 4.5.

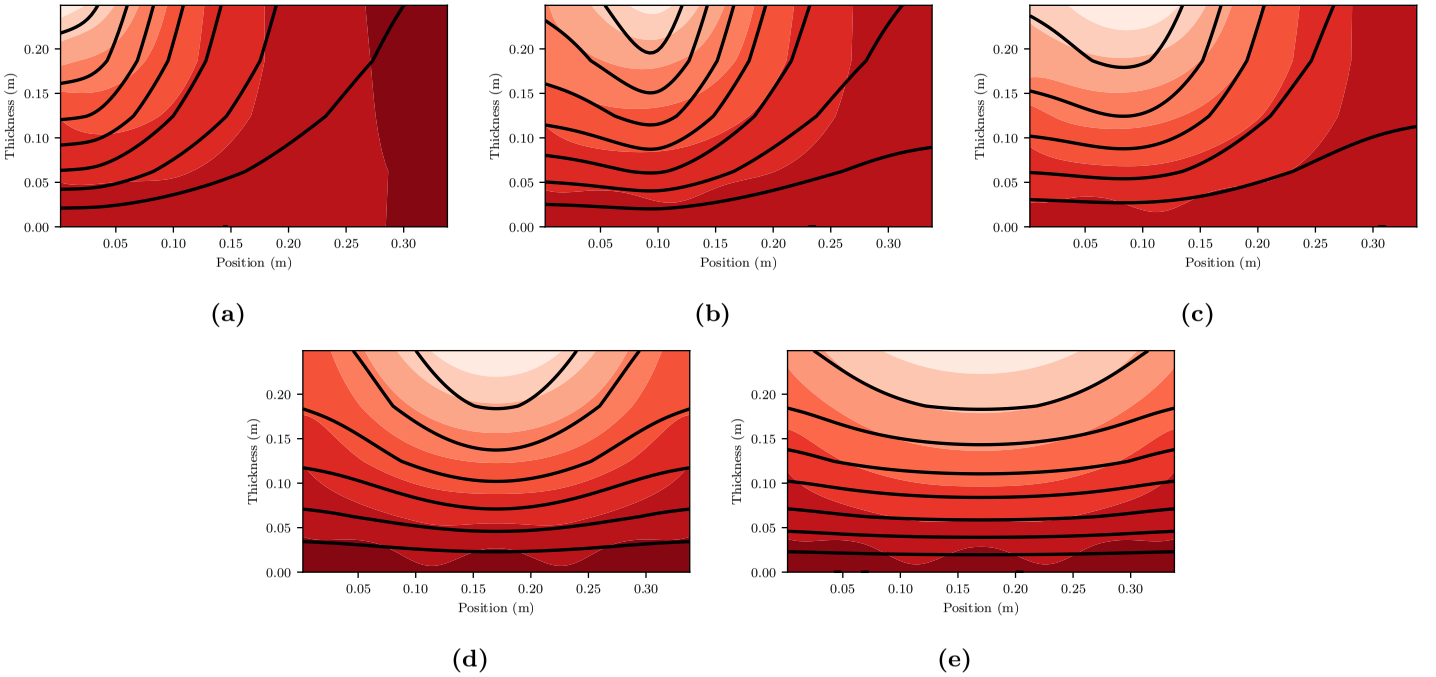

Figure 4.7: Displacement contours for static loads, wide FE model vs reduced order. Cases are reduced order (solid lines), and wide FE model (colored contour). Subplots correspond to the lines in Figure 4.5

.

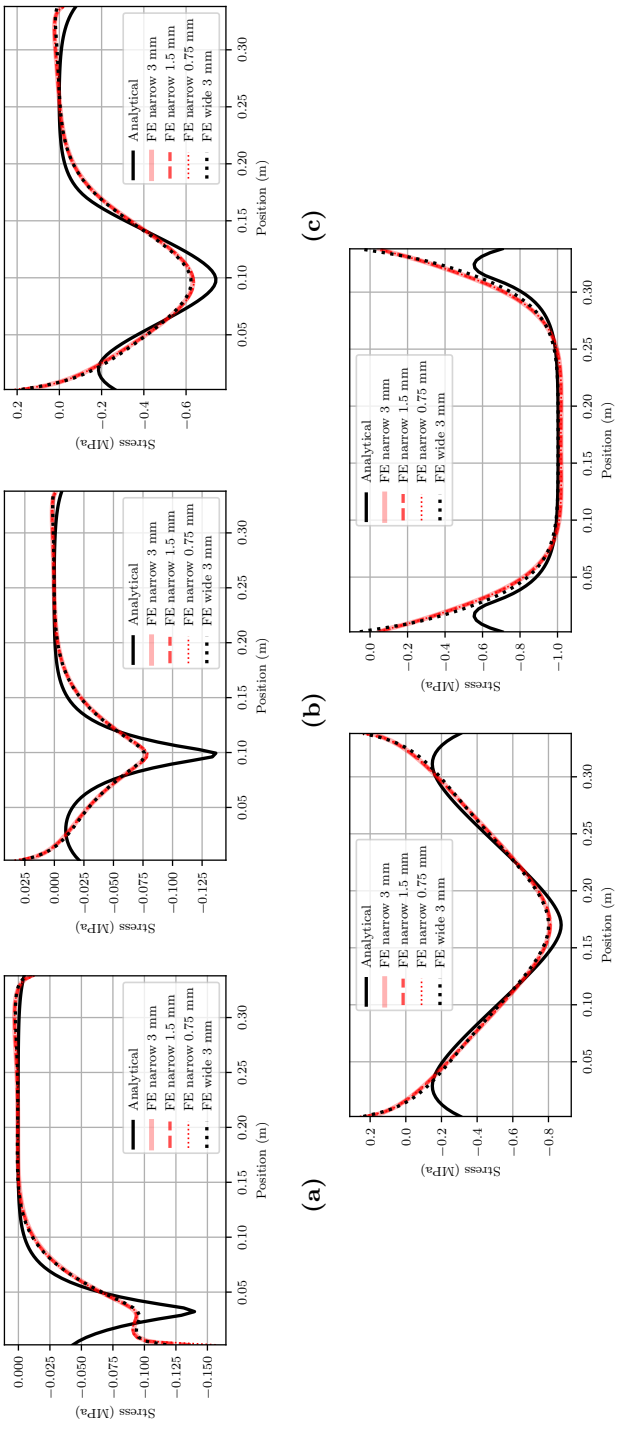

Figure 4.8: Vertical stress for static loads, subplots correspond to the lines in Figure 4.5.

rather than resting on the next subpanel. All shown element sizes overlap and are considered sufficiently accurate to predict stress and displacement. The reduced order model underestimates displacement for local loads, with increasing accuracy as the load becomes more uniform. This can be explained using Figure 4.7, where the FE model has most deformation at the top of the foam. Compare this to the reduced order model where the deformation is distributed over the entire height the foam. Therefore we conclude that the FE model is softer for local loads.

It was assumed earlier that the deflection of the back plywood between the mastic ropes does not affect the displacement at the top of the foam. This assumption is confirmed by looking at the displacement contours which, except for the bottom one, do not show where the mastic ropes are. At the bottom of the FE model there will be displacement between the mastic ropes but this is not predicted by the reduced order model.

Failure of the CCS requires specific material knowledge, which is not widely availiable. The vertical σ_z stress at the top of the foam is used instead and is plotted in Figure 4.8. First, note that the reduced order method overestimates the stress at the point where the load is maximum. As mentioned before, the FE model is softer for local loads than the reduced order model. Because it is softer the same total force at the top of the foam is distributed over a larger area, leading to a lower maximum stress. Loads near the edge add an additional stress peak, since there is a discontinuity in stiffness between the foam and plywood. This is not taken into account in the reduced order model. It is beneficial for the screening procedure to overestimate the response, because it makes the loads more important than what they really are.

For some of the reduced order results an increase of stress is found at the edge, because of the end spring condition derived earlier. We could also say this stress concentration indicates a peeling failure, which is not further explored here. For loads that are applied further away this stress is distrubuted over a larger area. An a priori error estimate is hard to define, because it strongly depends on the shape of the load. However, the general trend of the deformation and stress is similar, and therefore the reduced order model is considered a reasonable estimate.

4.2.2 Dynamic response

In Figure 4.9 the investigated load case is shown, a sloshing load from [59]. The three known pressure sensors are denoted $x = 17, 23, 29$ mm (c,d,e) in Figure 4.2. We scaled the pressures at $x = 2.65, 11, 31.35$ mm (a,b,f) with a factor $0, 0.1, 0$ from the nearest ones. At other times and positions the pressures are interpolated in time and space using third order splines.

The reduced order model uses the first eleven vibration modes to determine the response, it is compared to the narrow FE model, which has a geometry closest to the reduced order model. In Figure 4.10 the dotted line denotes the narrow

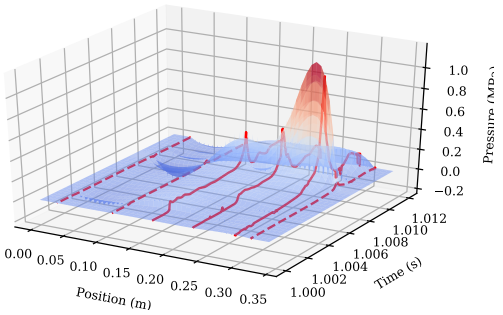

Figure 4.9: Dynamic 'slosh' load from [59], interpolated with cubic b-splines. The known sensors are plotted solid, the interpolated ones are dashed.

FE model with an element size of 3 mm, and the solid line the reduced order model. The FE model took about ten minutes to run, the reduced order model was finished within seconds. In the idealized case, the reduced order model would be 90 times faster than the FE model: the FE model has 90 elements over the height of the CCS, and the reduced order model one. The same comparison holds for the static loads, but there the difference is not as pronounced because only five loads are investigated. Such a run time would not be a problem for one load case, but in order to investigate many load cases the difference is significant.

Comparing the displacement shows that the FE model has higher displacement than the reduced order model. By looking at the different graphs, the trend of the displacement is quite similar, especially for the first impact. After that the load decreases again, going more towards free vibration. Any difference observed after the initial impact is due to the free vibration and therefore denotes a difference in natural frequency and mode shape between both models.

The stress in the FE model reaches its maximum earlier than the reduced order model, even though the displacement has coinciding maxima. This indicates that not all natural frequencies of the reduced order model are correct. The stresses are overestimated by the reduced order model, as in the static load case, so this is not considered to be a problem. For a specific structure one could, if an FE model is also available, tune the model parameters to maximize agreement for a load condition.

4.3 Conclusions and recommendations

This paper presents a reduced order model for a subpanel (panel between corrugations) of the Mark III CCS, to efficiently assess sloshing loads. A beam-foundation model is used, with a predefined displacement field over the thickness of the foam tuned to the first vibration mode of the subpanel. The reduced order model is

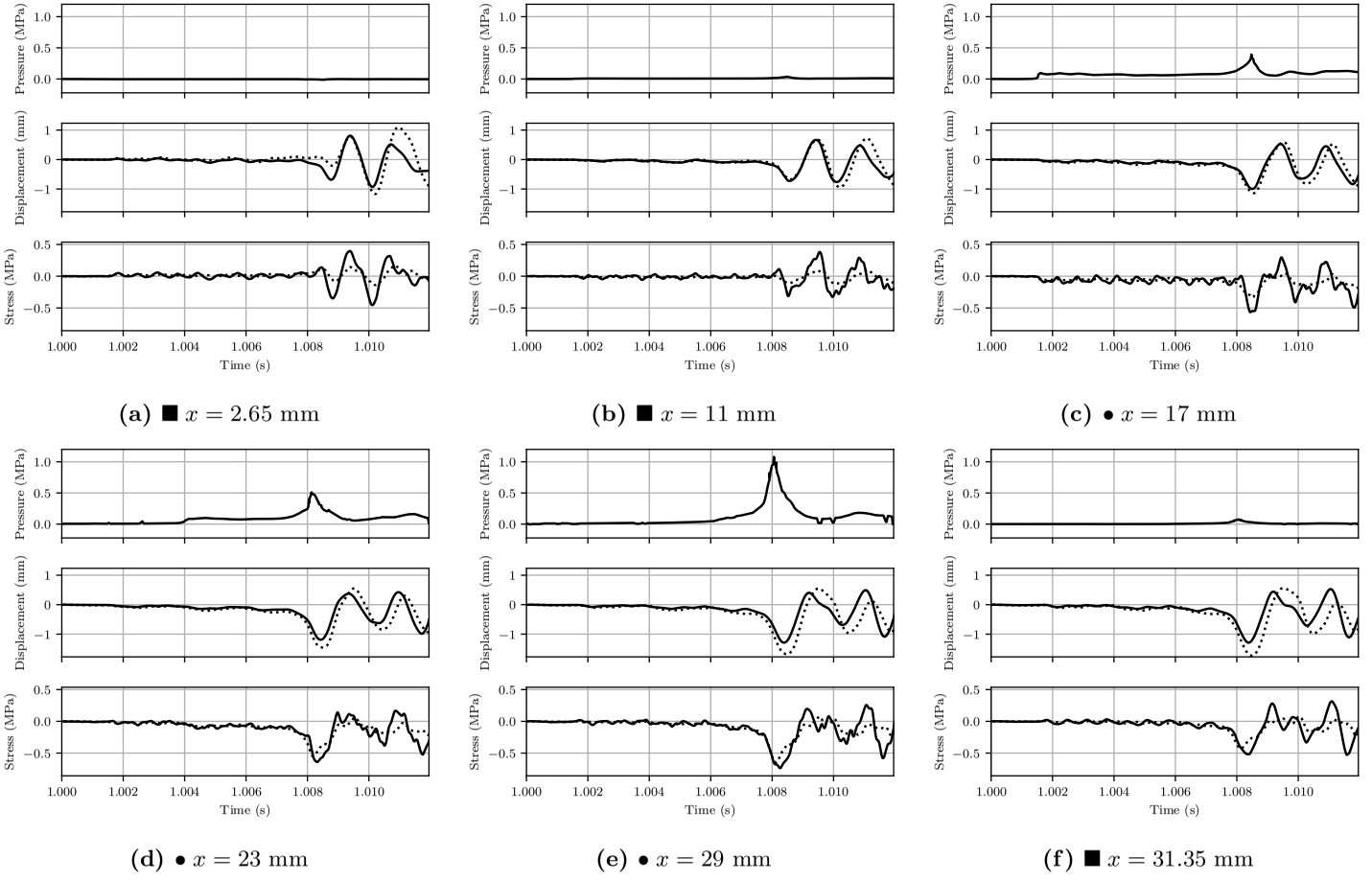

(a) ■ $x = 2.65$ mm **(b)** ■ $x = 11$ mm **(c)** • $x = 17$ mm

(d) • $x = 23$ mm **(e)** • $x = 29$ mm **(f)** ■ $x = 31.35$ mm

Figure 4.10: Displacement and contact stress at top of the foam for slosh load. Cases are reduced order (——) and FE model (.....). The load is from [59]. The symbols at the subplots correspond to the indications in Figure 4.2.

compared to a FE analysis for five static load cases and one dynamic load case using the same boundary conditions. Regarding the modelling assumptions, considering the bottom plywood and mastic ropes as rigid is justified when top stress and displacement are considered, as their effects cannot be seen at the top.

The reduced order model overestimates the maximum stress for the presented cases, while being two orders of magnitude faster. We see a larger difference for more localized loads, meaning the response to ELP 1 is predicted worse than for ELP 2 and 3. Because of its speed and conservativeness, the model is ideal for screening: to identify the important features, and associated phenomena, of sloshing loads. In addition the model can be used for defining maximum spatial distribution and size of pressure sensors to be used in experimental sloshing tests. However, we still recommend users of this model to double-check the most critcal cases with an FE model.

In future work there should be a better estimate for added mass and damping, because during the wave impact the structure is not completely wet or dry. The developed model should be extended with the ship inner hull, which can interact via its stiffness, damping and mass with the CCS, and therefore affecting the stress. Finally, other failure modes such as fracture of bottom plywood at supporting mastic ropes should be taken into account. With the aforementioned improvements and a failure law of choice, this model can be included in a screening procedure which quickly investgates many load cases. Then the user knows which cases are important and can investigate those cases further with an expensive FE model.

Chapter 5

Comparing 2D and 3D linear response of a simplified LNG membrane cargo containment system

Based on R.W. Bos, M.L. Kaminski. 'Comparing 2D and 3D linear response of a simplified LNG membrane cargo containment system' (2018) Proceedings of the International Offshore and Polar Engineering Conference, 2018-June, pp. 780-787.

Liquefied natural gas (LNG) is transported on board of ships in tanks insulated with cargo containment systems (CCS). These tanks are never completely full nor empty, which means that waves can form in the tank and impact on the structure. The wave impacts cause loads, and these loads and response to these loads are hard to predict. Both 2D and 3D models, experimentally and numerically, are used for such predictions.

In the Sloshel project [16] 2D wave impacts on a CCS were investigated experimentally, using different types of breaking and non-breaking waves in a flume tank on small and full scale. With these tests three elementary loading processes (ELP's) were identified [59]. Each ELP loads the structure in a different way, both very local and more globally, and each ELP scales with different dimensionless numbers.

Each ELP is associated with a different pressure distribution in time and space, also known as a pressure map. The first ELP is the direct impact, which is a high pressure localized in time and space due to the acoustic phase at first impact. The second ELP is the building jet, arising from the flow changing direction after hitting the wall, which is changing location over time. The third ELP is due to

entrapped gas, and pulsates over a larger (compared to other ELP's) area. In Sloshel the gas is air, inside a cargo tank this would be vapor.

The tests in Sloshel were performed in a 2D setting, whereas real cargo tanks are volumes with waves coming from all directions. In [87] sloshing tests two tanks with different widths, both smaller than the other dimensions, are excited in the plane. Higher loads are registered in the wide tank than in the narrow tank, hence even for this relatively 2D-case 3D-effects are noticed.

The global motion and loads can be predicted accurately, yet local variability is observed, as shown in [36]. The variability is caused by local features resulting in local loads. This variability introduces stochastic variables to the sloshing assessment. For assessment of the cargo containment system (CCS) model tests are used. Waves with a 3D profile are generated by imposing 6 degree of freedom motions on a partially filled model scale tank [40]. A statistical correction should be used to take the variability, and the difference thereof between small and full scale, into account. This is displayed in first three boxes of Fig. 5.2.

On the other hand we can look at CFD, for instance [44, 43], in which wave impacts are simulated using an SPH code. It takes a lot of computational effort to capture all the local flow details in the pressure map related to the direct impact. Even then, some physics are not included, such as phase change, as shown in the bottom of Fig. 5.2.

Knowing these difficulties exist, we can wonder whether they are 'important': do they influence the response, and ultimately the failure of the structure? For which ELP's should the scaling be absolutely correct, looking from the structural response and failure point of view? Should variability and phase change and local variability be included in CFD? The sensitivity of the structural response to these questions should be the answer. These questions are addressed in the SLING research programme, and will play a role when liquid hydrogen is considered in the future.

Looking at the structure, commonly 3D models are used. For instance in [79], a square section of the Mark III CCS is modelled from the mastic ropes up to the primary membrane. Such an assessment is also required by class [1, 26], where the capacity of the structure under a patch load is investigated.

A possible starting point for investigating the sensitivity of the CCS to non-2D loads is to use 3D FEA analysis, including many structural details. That would however require a lot of computational effort for what is in fact a sensitivity study. A model is therefore chosen which represents the characteristics of the CCS, but does not provide exact answers. In [75] a model of a beam on a foundation is used to model plastic sandwich indentation, which is adapted in this paper to represent the CCS, as is done in [11].

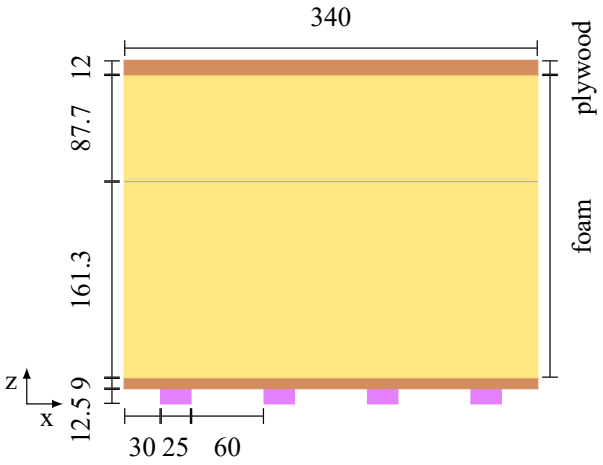

Figure 5.1: Cross-section of the Mark III cargo containment system (CCS) as designed by GTT with measures in mm similar to [58].

Summarizing, complex 3D models give an accurate representation of the structural response, but are computationally expensive. Knowing 2D models are computationally cheaper, it can be wondered in which cases such a 2D model would be sufficient. And we know that even idealized 2D experiments have a 3D component. In this paper the structural response to 'almost' 2D loads is investigated, in order to quantify the influence of such a deviation from a 2D load. This question is summarized in Fig. 5.3. On the left side the 2D load is shown, on the right side the load has a slope, meaning the load maximum at one side of the panel is at a different place than at the other side. These loads will henceforth be called ridge loads. In order to quantify the importance of the slope, indentation and stress levels due to both loads are compared. A similar procedure is followed for local cone-shaped impacts, which are related to direct impact of for instance a droplet on the wall.

The model represents the foam and top plywood of a Mk III CCS designed by GTT and it is shown with dimensions in Fig. 5.1. The top plywood is modelled by a Kirchhoff plate, the primary and secondary membrane are not modelled. Free boundary conditions are placed at the relaxation grooves, so the plywood plates are not coupled. All material anisotropy is disregarded, taking only stiffness in the thickness direction for the foam and in weakest bending direction for the plate. Added mass, damping and temperature effects due to the LNG are also not taken into account. Hereafter the top of such a unit is called the subpanel (plywood plate of 340 mm by 340 mm), hence a part of a larger panel of the CCS. Such a small area is looked at because it repeats all over the tank walls, ceiling and bottom.

This paper consists of the following parts. First the method is explained, in

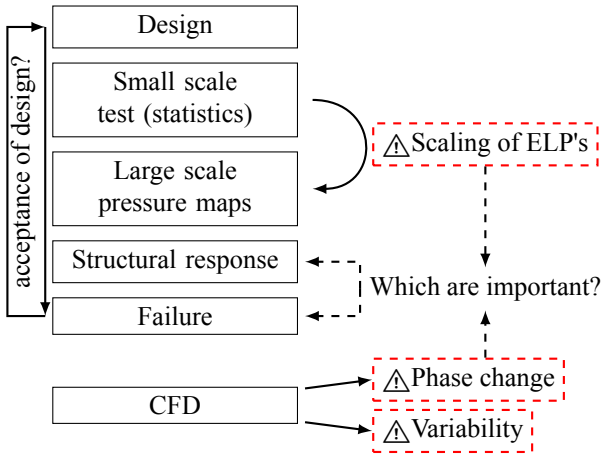

Figure 5.2: Place of this research in CSS assessment.

which emphasis is put on explaining how the natural vibration modes are found using a semi-analytical model. Then, the load cases are given and the response is calculated, at the same time the results are discussed. Finally, the conclusions are presented.

5.1 Method

The response to a load is calculated using modal analysis. First the vibration modes and frequencies are calculated, which is explained in the first part of this section. In the second part of this section these vibration modes are verified through comparison with FEA. Then the load is projected on the modes and the modal response is integrated over time. After integration the contributions of each modes are summed up to yield the displacement of the plate.

For time integration a trapezoidal implicit scheme is used, with a time step of one

Table 5.1: Input parameters from [79], no subscript means foam, subscript b means top plywood.

E_b	13,200	MPa
t_b	12	mm
ρ_b	680	kg/m^3
ν_b (FEM)	0.3	-
E	95	MPa
h	249	mm
ρ	125	kg/m^3
ν	0.2	-

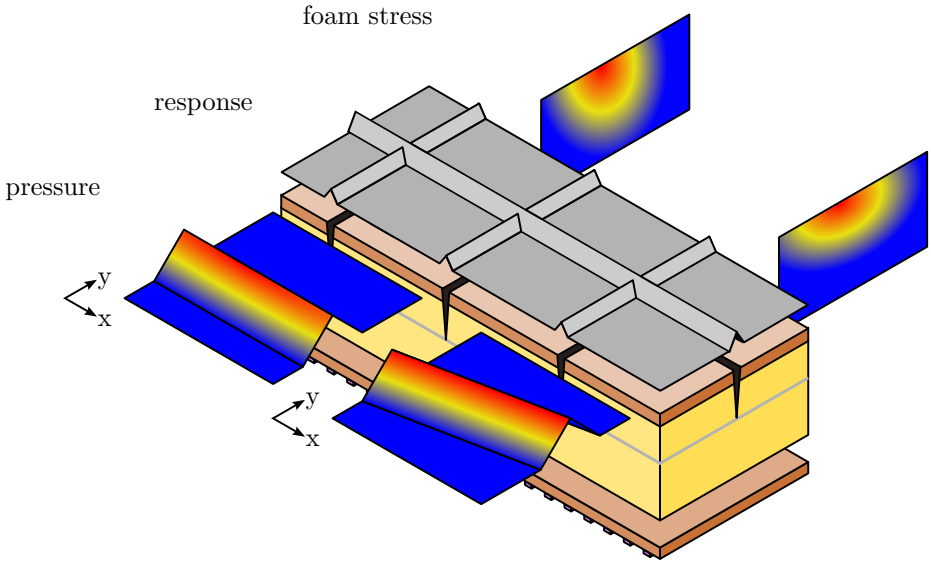

Figure 5.3: Graphical summary of this paper. Similar loads with different slopes are shown left and right, and applied to a simplified model of the Mark III CCS. This model is a subpanel, describing the area between relaxation grooves including only top plywood and foam. Resulting stresses are compared.

tenth the rise time $dt = \tau/10$. This allows for a small enough time step the lower modes to be solved with reasonable accuracy, and higher modes automatically taken as static. A damping of 0.1% of the critical damping is taken for each mode.

5.1.1 Analytical model

For a two dimensional sandwich structure the local indentation and stress between the face sheets and core can be predicted using an elastic beam on a foundation [75]. This leads to the following equation of motion, [95] (coefficients renamed):

$$\gamma \frac{\partial^2 w}{\partial t^2} + \frac{\partial^4 w}{\partial x^4} - \mu_s \frac{\partial^2 w}{\partial x^2} + \mu_k w = \frac{1}{EI} p_t \tag{5.1}$$

with $w = w(x,t)$ as displacement field of the top of the foam over space and time and $w = p_t(x,t)$ as pressure map.

From [95] the constants of Equation 5.1 can be determined. One is supposed to take an assumed displacement field $\psi(z)$ over the height of the foundation (or foam core), which interpolates the top indentation to the foam displacement field. Here the foam is homogeneous over the height since it is chosen to disregard the temperature properties and anisotropy. In a thought experiment, the first

vibration mode will be a uniform 'up and down' motion of the plywood, giving uniform compression of the foam. Therefore $\psi(z) = z/h$ is chosen, making the displacement field of the foam $w_f(x, y, z, t) = (z/h) \cdot w(x, y, t)$, where $w(x, y, t)$ is the plywood indentation.

Submitting the aforementioned displacement field into the equations given by Vlasov leads to the following coefficients:

$$\gamma = (\rho_b h_b + \frac{\rho h}{3})\frac{1}{D},\ \mu_s = \frac{Eh}{6(1+\nu)}\frac{1}{D},$$
$$\mu_k = \frac{E(1-\nu)}{h(1-\nu-2\nu^2)}\frac{1}{D} \tag{5.2}$$

In which E is the elastic modulus of the foam, h foam height, D flexural stiffness of the plywood and $\rho_b h_b$ the inertia per unit area of the plywood, ρ the density of the foam. These parameters are taken from [79] and are listed in Table 5.1.

For free beam vibration the following boundary conditions can be derived:

$$M(x) = D\frac{\partial^2 w}{\partial x^2} = 0 \text{ at } x = 0, a \tag{5.3}$$
$$Q(x) = -\mu_s \frac{\partial w}{\partial x} + \frac{\partial^3 w}{\partial x^3} = 0 \text{ at } x = 0, a \tag{5.4}$$

where the first states that moment $M(x)$ at the edges $(x = 0, a)$ should be zero, and the second states that shear force Q at the edge of the beam should be compensated by the shear force of the foundation.

Using [95] with the aforementioned displacement field for the foam, the coefficients of the 2D theory can simply be used in the 3D equations, where $w = w(x, y, t)$:

$$\gamma \cdot \frac{\partial^2 w}{\partial t^2} + \nabla^4 w - \mu_s \nabla^2 w + \mu_k w = \frac{1}{D} p_t(x, y, t) \tag{5.5}$$

which has the same coefficients and boundary conditions as the aforementioned 2D equations, recognizing they work the same in the out of plane direction. The ∇^4 and ∇^2 denote the biharmonic and harmonic operators respectively.

Also in this simplified model the indentation and curvature of the subpanel are related to the stress at the top of the foam, by:

$$\sigma_z(x, y, z = h) = D \cdot (\mu_s \nabla^2 w + \mu_k w) \tag{5.6}$$

which is obtained by subtracting the plate and its applied load from Equation 5.5, leaving only the load on the bottom of the beam. This means that the normal stress at the top of the foam depends on the indentation and curvature of the top plywood.

Free boundary conditions are applied to the sides, which physically represents the top plywood subpanels being independent. These boundary conditions, as well as the coupling term in the PDE, make finding a solution difficult. To summarize, only a part of the solution is taken in order to approximate the deformation field. This method is also proposed in [84].

5.1.2 Verification using finite element analysis

A structural model using the same geometry and material properties as analytical model is set up in ANSYS. The primary and secondary insulation are merged into a single linear solid element over the height. The top plywood is modelled by a linear plate element, without offset. At the bottom the plywood and mastics are assumed rigid, the primary and secondary membranes are not taken into account. At the top all nodes are constrained in the in-plane direction, so only the 'plate bending' modes are allowed. Element size is chosen to be approximately 4.5 mm on each side. This model has as goal to verify the analytical model, the assumptions behind this model are therefore not investigated.

The vibration frequencies of the FEA model can be calculated and compared to the analytical modes. In Fig. 5.4 two vibration modes are compared by their Chladni figure, which draws lines on the nodes of the vibration. These vibration modes are predicted using only the first ten cosine terms up to a maximum of 50 kHz. Whenever a similar mode was found between the cosine terms, the lowest (most compliant) mode was chosen.

As can be seen in Fig. 5.4, the agreement in shape is quite good, since the grey lines of the Ansys solution match the black lines representing the semi-analytical solution. In general the FEA solution has more details, as seen by the wiggles in the lines. Looking at the frequencies the difference is small for low frequencies, but increases to 5%-10% for higher modes. This can be explained by the omission of the higher cosine terms, both in finding and weighing the solution. In practice this results in the higher modes being too stiff, hence the plate is less sensitive to local loads and deformations.

5.2 Results and discussion

The loads are defined as follows. First, a pressure distribution is defined over the height of the subpanel, with a unit width and its center at the bottom. For the ridge load cases the coordinates of the points describing the mode shapes are transformed to this 'height' coordinate using:

$$h(x, y) = \phi(\theta x + y + c) \tag{5.7}$$

where ϕ gives the total width of the load, θ is the slope and c shifts the load from the bottom of the plate upward. The cone shaped load cases are defied by a cone diameter ϕ and the center of the cone x_m, y_m. In time the load is a triangular

pulse with rise time τ, equal to the falling time. All loads have a maximum of 1 MPa, which means that the force and impulse exerted by the load is not equal among the load cases. Examples of the loads are shown in Fig. 5.5.

Table 5.2 shows the load cases, for which the response is determined. Three ridge load cases are chosen: two loads applied in the center of the subpanel, and one at about one third of the height. Also, three cone load cases are chosen, of which the impact location is changing from the edge to middle. These loads are chosen because by taking a 2D slice, for instance by a 2D simulation or pressure measurement, one obtains the same 2D pressure. All loads have a rise time τ, and the load is applied in a triangular profile with same rise and fall time.

It should be mentioned that adding a slope to the load, or displacing the cone, has a very limited effect on the magnitude of the load ($< 1\%$). Load case 2 has twice the total impulse (pressure integrated over time and area) compared to load cases 1 and 3, because it acts on a larger area while keeping the same maximum load. The same goes for load case 5 compared to load cases 4 and 6. Between the different rise times there is a factor 10, which is the same factor of difference for the impulse.

The difference in response can be quantified by comparing the maximum indentation of the top plywood, as well as the normal stress between the foam and plywood. This normal stress is related to the failure of the CCS and therefore a good measure of the importance of the load slope and impact location.

For load case 1 with rise time of $\tau = 0.01$ s a snapshot of the deformation at time of the maximum deformation is shown in Figs. 5.6a and 5.6b, for slopes of $\theta = 0, 0.4$, of which the loads are shown in Fig. 5.5. The results for slope $\theta = 0$ show symmetric indentation of the structure, which is largest at the sides and smallest in the center, 0.26 mm and 0.18 mm respectively. One could expect the same displacement along the width of the subpanel, as with a 2D beam. This is not the case because of the edge spring stiffness at the boundary conditions. Another difference with a 2D beam is, that the plate has higher stiffness due to the

Table 5.2: Load cases

Ridge	ϕ (mm)	θ (-)	c (mm)	τ (s)
Case 1	50	0, 0.1, ..., 0.4	170	0.01, 0.001, 0.0001
Case 2	100	0, 0.1, ..., 0.4	170	0.01, 0.001, 0.0001
Case 3	50	0, 0.1, ..., 0.4	85	0.01, 0.001, 0.0001
Cone	ϕ (mm)	x_m (mm)	y_m (mm)	τ (s)
Case 4	50	34, 68, ..., 170	170	0.01, 0.001, 0.0001
Case 5	100	34, 68, ..., 170	170	0.01, 0.001, 0.0001
Case 6	50	34, 68, ..., 170	85	0.01, 0.001, 0.0001

Poisson ratio and that the bending directions are coupled due to the biharmonic operator in Equation 5.5.

Comparing $\theta = 0$ to $\theta = 0.4$, the sloped load, the indentation at the sides differ little, at 0.22 mm and 0.20 mm. The ridge load excites more complicated modes with higher natural frequency, which are more stiff. Hence, the maximum indentation due to the sloped load is somewhat less than for the straight load.

Loads with a rise time of $\tau = 0.0001$ s are well past the first natural frequency of the subpanel, and should therefore yield a dynamic response. The result is shown in Figs. 5.6c and 5.6d, which are compared to Figs. 5.6a and 5.6b to investigate the effect of rise time. In contrast to the slow load, largest response of the subpanel seems to be concentrated at the edges. This is because the shorter rise time excites higher modes, and the more global displacements due to the first vibration modes is much less.

A similar analysis can be performed for the cone loads, for instance for load case 5 in Fig. 5.7. Here it is observed that for both rise times the load excites much more response when it is applied near the edge than in the center. An intuitive explanation is that the edges are less stiff than the center because it is less well supported. Another trend which is observed is that the fast load has more local features than the slow load, which is also seen with the ridge loads. For instance, in Fig. 5.7b there is indentation over the entirety of the foam, whereas the left and right edges of Fig. 5.7d are not indented at all.

The maximum indentation of all ridge load cases is summarized in Fig. 5.8a, and for the cone loads in Fig. 5.8b. Taking the force of the loads into account, it makes sense that indentation is approximately twice as large as for load case 1. Load case 3 gives a higher indentation due to being applied close to the edge. A slope moves the load even closer to the edge of the subpanel, explaining the sensitivity. Rise time seems to have little effect, once the load is applied faster than the first natural frequency.

From the load cases with conical loads, Fig. 5.8b, load case 5 is most sensitive to location, load case 4 and 6 are less so. The reason is that load case 5 is applied on a large area compared to the subpanel size. For all load cases the maximum indentation is lower when the loads are applied closer to the center of the subpanel.

Stress levels at the top of the foam as result of the ridge loads, Fig. 5.9a show a different trend. This can be attributed to the stress also depending on the second derivative of the indentation, as described in Equation 5.6. When indentation and curvature increases, the stress at the top of the foam increases. An example of this is shown by comparing Fig. 5.6a and 5.6b. The maximum indentation is the same, but the contour lines are closer for the sloped case.

The conical loads of small radius (load case 4 and 6) show in Fig. 5.9b a similar

result for stress, regardless of distance from the side and bottom. This is different from the trend observed for the indentation, meaning that close to the edge the indentation increases but the curvature not, as confirmed by looking at Fig. 5.7a and 5.7b. For the load with the larger radius, and therefore total force, the impact location influences indentation in the same way as stress. This can be explained by larger load area causing smaller curvature, hence the stress is dominated by the indentation.

Comparing Figs. 5.8a and 5.8b it is shown that all the cone loads, with same maximum pressure, have similar order of magnitude maximum indentation and stress. This is somewhat surprising since the cone loads act on a smaller are than the ridge loads, moreover the ridge loads have a line of the maximum pressure, while the cone loads have only one point.

A reasonable estimate for the indentation might be obtained for the ridge loads with all investigated slopes, but the stress error is already apparent for slope $\theta = 0.1$. The sensitivity of the indentation and stress to the location of the cone load is small for a small cone radius and at distance from the side.

5.3 Conclusions and recommendations

The slope has little effect on the indentation as long as the load spans over the width of the subpanel. When looking at the stress and applying the load near the edge of the subpanel, the sensitivity to the slope is higher. Hence, it can be concluded that 2D models are only suitable if the slope is small ($\theta < 0.1$). For larger slopes a 3D model should be used.

When cone loads are considered, as long as the size of the cone is small enough compared to the subpanel they can be placed anywhere and yield similar maximum indentation and stress. For larger cones the application point of the load does influence the result, where a load closer to the edge of the top plywood elicits a larger indentation and stress.

For both the ridge and cone loads there is not a large influence of rise time in the maximum stress or indentation, the trends and absolute values are similar.

These conclusions do not render the 2D models useless. Most indentation and stress levels show the same order of magnitude independent of the slope or impact location.

A simple improvement to increase the accuracy of the answer, is to use more vibration modes. As next steps, the foam can be modelled more accurately using higher order shapes for the displacement field, including anisotropy of the foam. Furthermore, a considerable effect of added mass and damping is expected for such a lightweight structure. The comparison of indentation could be supplemented with a comparison of stress at the bottom of the foam, where the extreme values

are expected. In order to check the assumptions a comparison with a refined linear dynamic FEA model could be made.

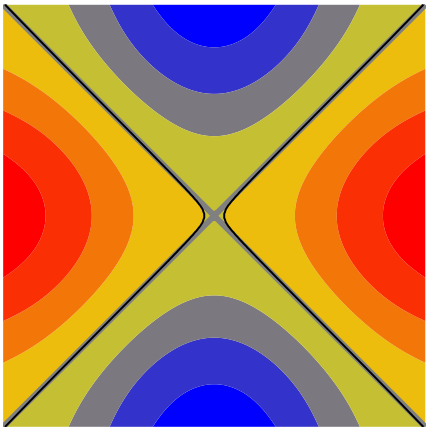

(a) Ansys: 1527 Hz, Analytical: 1518 Hz

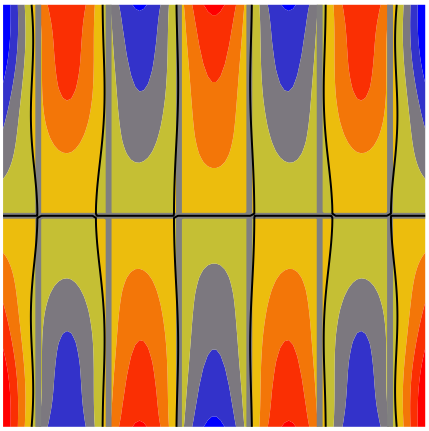

(b) Ansys: 5838 Hz, Analytical: 6073 Hz

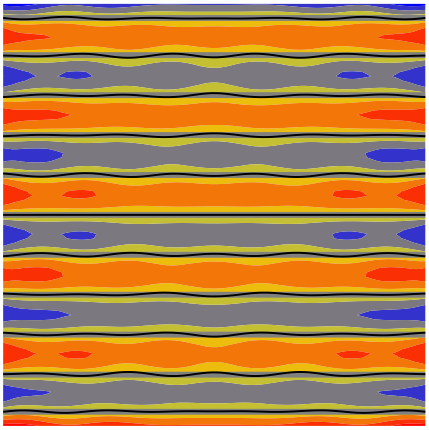

(c) Ansys: 15273 Hz, Analytical: 17417 Hz

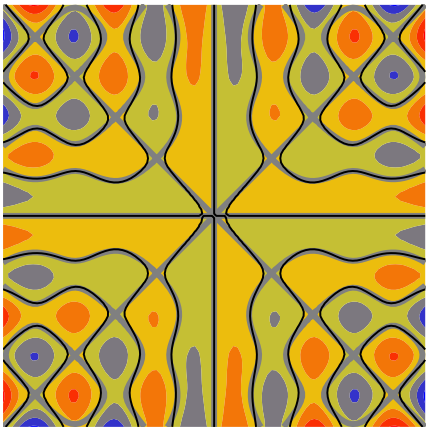

(d) Ansys: 15275 Hz, Analytical: 17513 Hz

Figure 5.4: Chladni figures of the vibrating plate for two frequencies. The coloured contour shows the out of plane displacement of from FEA, with the thin black line as zero crossing line, the thick grey line is the zero crossing of the analytical solution.

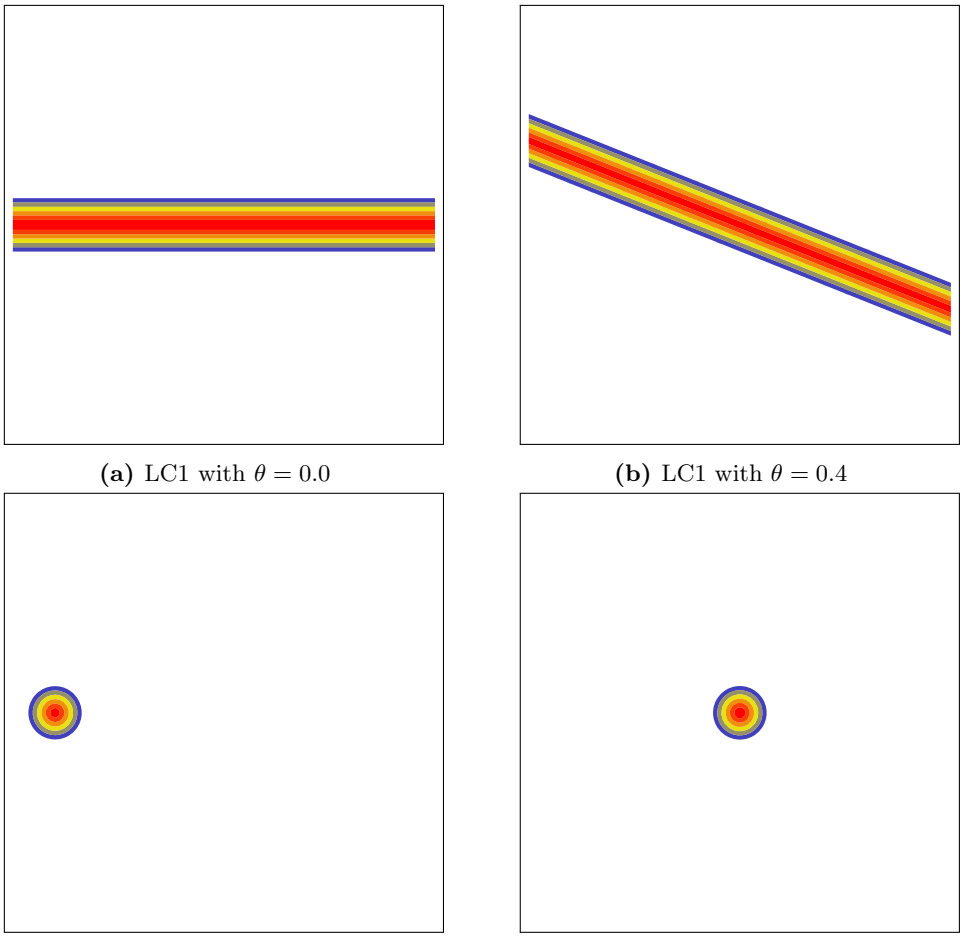

(a) LC1 with $\theta = 0.0$

(b) LC1 with $\theta = 0.4$

(c) LC4 with $x_m = 34$ mm

(d) LC4 with $x_m = 170$ mm

Figure 5.5: Loads applied on the structure, with minimum of 0 MPa and maximum of 1 MPa.

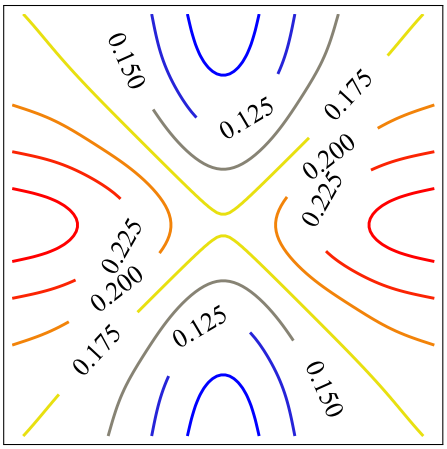

(a) $\theta = 0.0$, $\tau = 0.01$ s

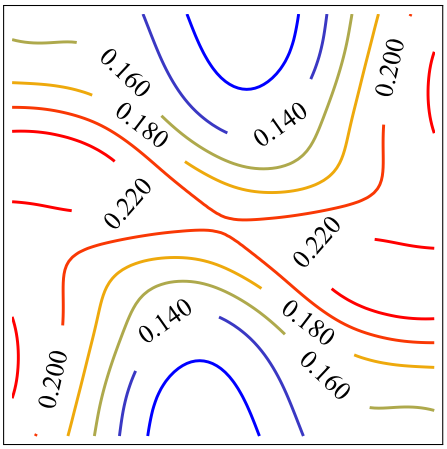

(b) $\theta = 0.4$, $\tau = 0.01$ s

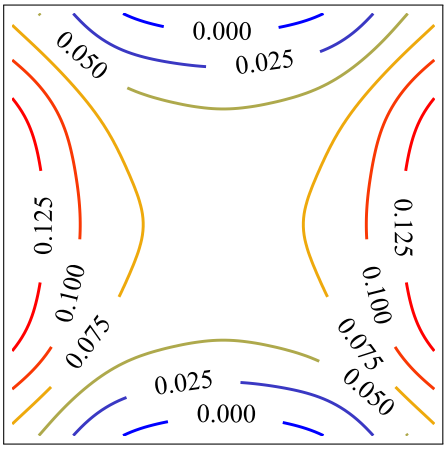

(c) $\theta = 0.0$, $\tau = 0.0001$ s

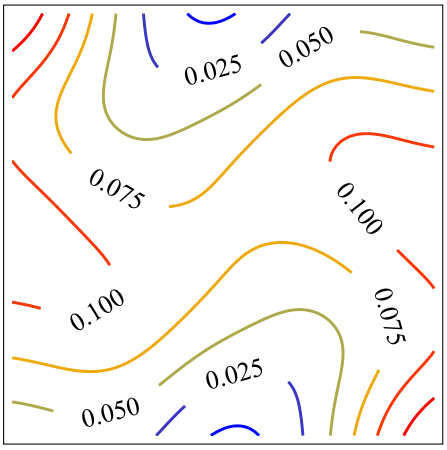

(d) $\theta = 0.4$, $\tau = 0.0001$ s

Figure 5.6: Maximum indentation for LC1

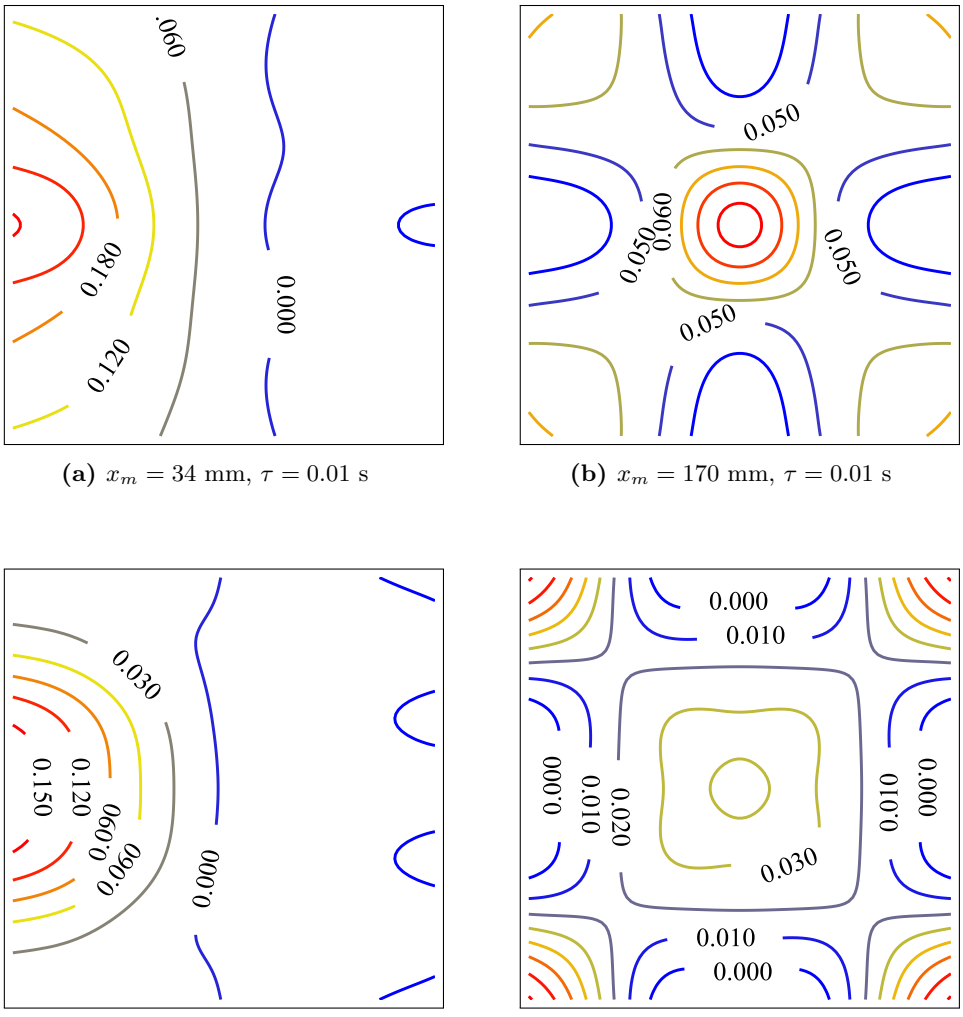

(a) $x_m = 34$ mm, $\tau = 0.01$ s

(b) $x_m = 170$ mm, $\tau = 0.01$ s

(c) $x_m = 34$ mm, $\tau = 0.0001$ s

(d) $x_m = 170$ mm, $\tau = 0.0001$ s

Figure 5.7: Maximum indentation for LC4

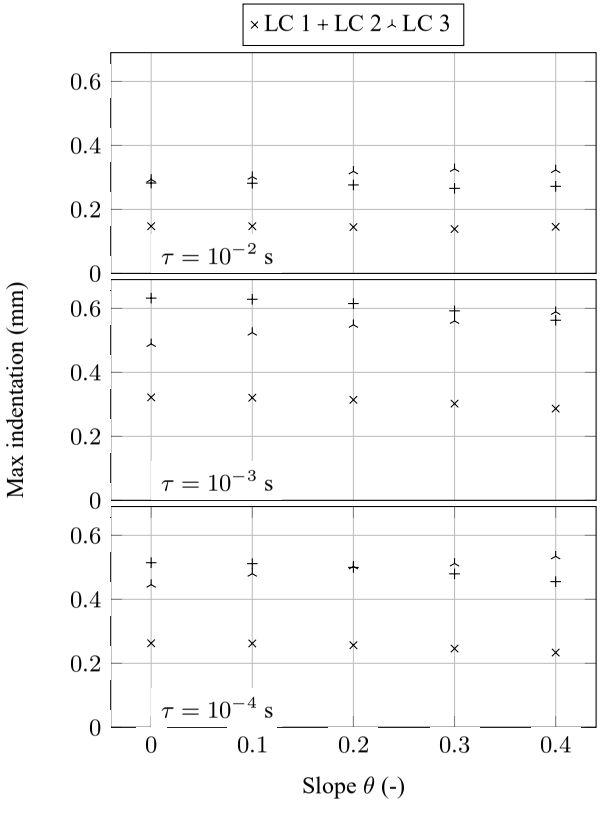

(a) Maximum indentation for ridge loads (LC1-3)

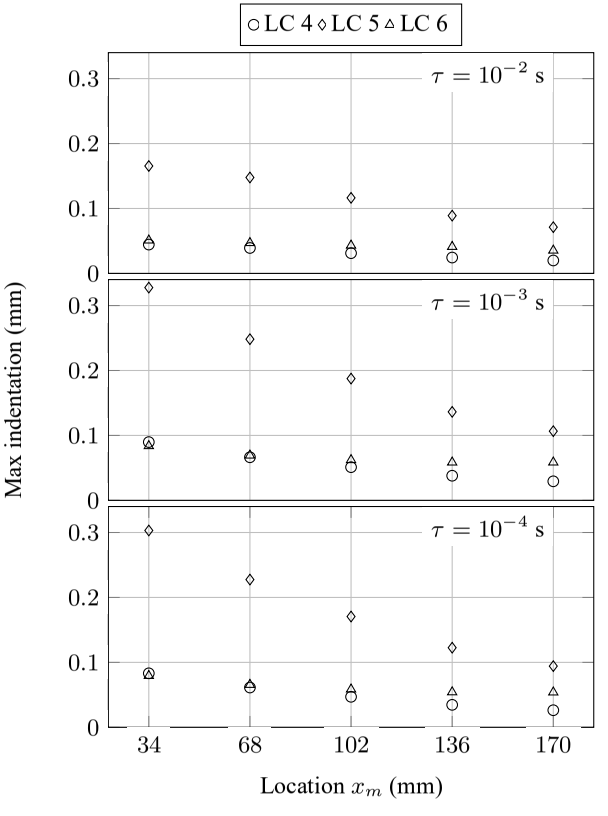

(b) Maximum indentation for cone loads (LC4-6)

Figure 5.8: Summary of indentation for load cases 1-6.

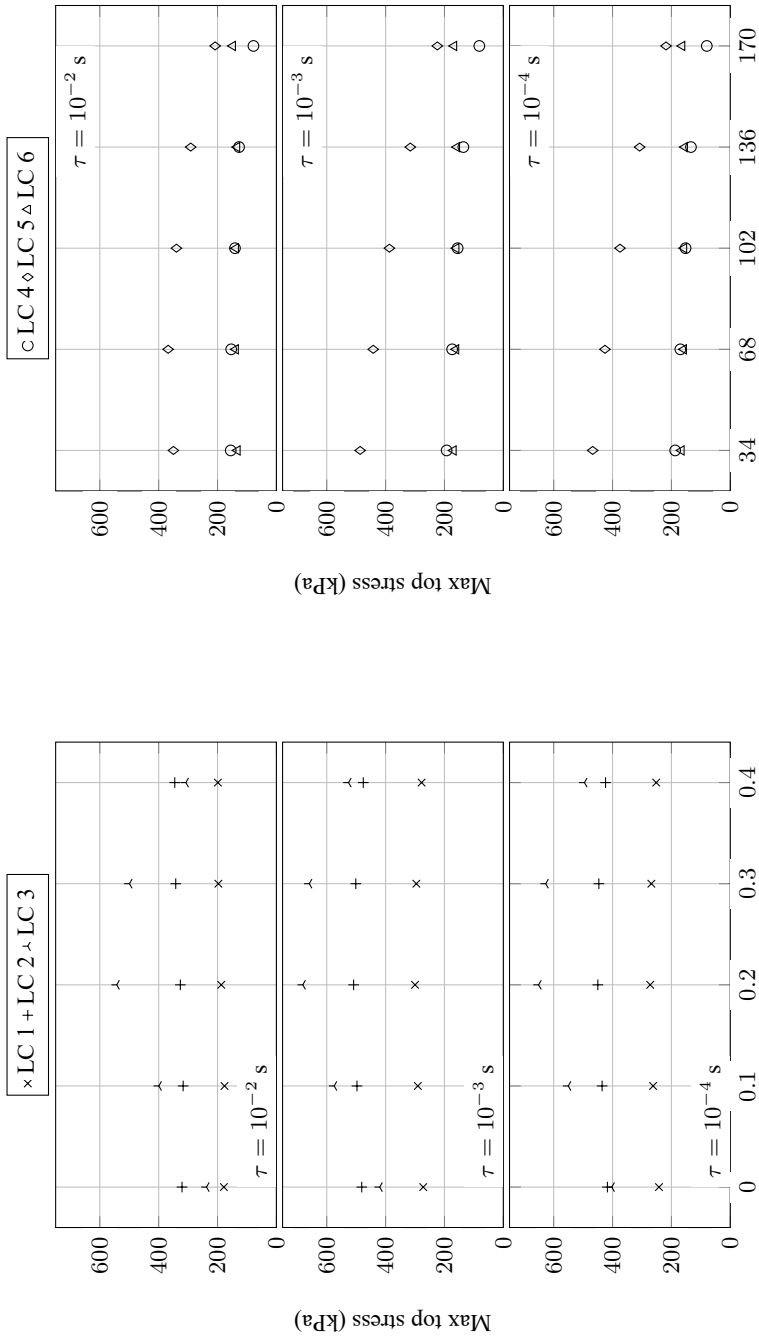

(a) Maximum top stress for ridge loads (LC 1-3)

(b) Maximum top stress for cone loads (LC 4-6)

Figure 5.9: Summary of stress for load cases 1-6.

Chapter 6

A reduced order model for FSI for wave impacts in LNG sloshing

Based on R.W. Bos, M. van der Eijk, P.R. Wellens, J.H. den Besten. 'A reduced order model for FSI for wave impacts in LNG sloshing', submitted.

Wave impacts on inner walls are known phenomena in liquefied natural gas (LNG) sloshing on board of LNG tankers, and is characterized by high variability of the loads due to free surface instabilities before impact [8]. The LNG in the tanks is kept at its boiling point (-162°C), causing phase change and cryogenic conditions for the tank walls which should maintain structural integrity at all times. An insulating cargo containment system (CCS) is applied to the tank walls in order to prevent the steel hull from becoming brittle. For an optimal insulation the tank walls should be as light and thick as possible, for maximum strength they should be as thin and heavy as possible. These contradicting requirements combined with the variability of loads complicate the design of such a CCS.

The design loads of a CCS are typically determined using model tests on a 1:40 scale [40]. A rigid scale model of the LNG tank is fitted with pressure sensors and excited in a similar way as the real tank would. The pressures are statistically post-processed and applied to the structure in patches [81]. In this approach the dynamics and flexibility of the structure is not directly taken into account, only through dynamic amplification factors.

A large test campaign investigating wave impacts for LNG CCS is the 'Sloshel' project [8, 9, 53]. A real LNG CCS was put in a vertical end wall of a flume. Then different shapes of waves loading the wall were obtained by changing positions of the focal point with respect to the wall. Depending on the wave shape, three elementary loading processes (ELPs) were identified [59]:

1. Direct impact: the first part of the wave hits the wall
2. Building jet: the fluid has to change direction and spreads along the wall
3. Pulsating gas pocket: enclosed gas is compressed and causes a varying load

Each of these ELP's has a different signature, physics, and scaling, which makes the aforementioned model tests difficult to translate to real tank applications. However, not all these ELP's are of equal importance for the response of the structure. The response depends on the loaded area and time signature, as for instance demonstrated in [12]. Furthermore, if it is known which loads (or ELPs) are most important for the structural response, then the hydrodynamicist can focus on predicting these loads.

The structure considered in this paper is the 'Mark III' CCS of the company GTT [49, 38], which is a sandwich structure with a foam core and plywood face sheets, as shown in Figure 4.2. On the inside of the tank a stainless steel membrane is fitted to keep the LNG inside, and a secondary membrane is fitted between the foam layers for redundancy. In order to minimize thermal stresses, relaxation grooves are cut just above the secondary membrane, creating 'subpanels' of 340 by 340 mm which are to a large extent uncoupled [11].

The CCS has two main failure modes: plastic indentation failure of the foam and shear failure of the bottom plywood [49, 18]. A reduced order model for the onset on indentation failure is presented in [11], based on [75] and [95]. Prediction of the structural response can be significantly sped up using such a reduced order model, possibly leading to great simplification of the coupled problem.

The problem is however slightly more complex, as shown for instance in [64], where sloshing model tests including FSI are described for a flip-through impact. A 2D tank is used with an elastic flat wall at the end, which represents the CCS. The deformations of the wall are measured and computed (using pressures on the rigid wall). A comparison shows that the wall response requires more than just the pressure on the wall and added mass and damping, especially due to the change of added mass in time. This means for us that the response of the structure to the loads (one way coupling) is different from the fully coupled response (two way coupling). Hence, it can be necessary to take the two way coupling between the load and wall into account when investigating which loads are important.

The two-way coupling can be investigated for the entire tank, as demonstrated in [106]. Here the stiffness of the wall was varied and the tank excited in the same way. As the tank wall becomes increasingly compliant, the pressures decrease and show a more vibratory response. The total time during which the pressure sensor was loaded is longer. This is however numerically expensive and time consuming, especially considering the highly variable loads that require a probabilistic assessment.

For such a probabilistic assessment we look at simplified models, that are fast and sufficiently accurate for the situations in which they are used. The load due to a wave impact and therein encapsulated air can be predicted using two simplified models: the Wagner and Bagnold model [68]. First, the Wagner model can describe the building jet (ELP2) based on an initial shape and potential theory for the flow [96]. The load of the Wagner model starts with a high peak at the point where the wave hits the structure, and then spreads out over the wall and simultaneously decreases in magnitude. Second, the Bagnold model describes how entrapped gas pulsates (ELP3) based on a gas law and some moving mass representing the surrounding water [6].

In this paper the coupling between the CCS and a wave impact is investigated on the subpanel level. The subpanel is represented by the model proposed in [11], namely a beam-foundation model. ELP 2: 'building jet' is chosen as load case, because it is expected to give a response on the length and time scale as the structure. This paper focusses on how the load is modelled and how the load interacts with the structure. It presents a simplified model for ELP2, in the form of non hydrostatic shallow water equations (NHSWE [52]), made suitable for numerical implementation of the coupling. To our knowledge this is the first paper to propose a reduced order model for fluid-structure interaction for wave impacts, that is fast and versatile enough for probabilistic evaluation. Figure 6.1 shows how the presented model relates to an actual wave impact. The drawn lines approximate the shape of the breaking wave, symmetrical over the horizontal plane. We developed this model to be faster than a detailed CFD code, so that it can be used in to perform a sensitivity study of the importance of FSI for various wave impact parameters.

In the rest of the paper we will derive the equations for the fluid model and couple it to the structure. Then a number of wave impact scenarios are investigated with this code and a more detailed in-house CFD code: EVA. EVA is based on the Navier-Stokes equations for the motion of a mixed fluid with varying properties to model the combination of a liquid and a gas phase. The robust method makes use of a fixed staggered Cartesian grid where for the convective term a second-order upwind scheme is used. The time integration is based on a second-order Adams-Bashforth scheme. The description of the free surface is done with the Volume-of-Fluid (VoF) where the interface is geometrically reconstructed using piecewise-linear line segments. By consistently coupling the mass and momentum fluxes, EVA is capable to model high density ratio two-phase flows. The externally added interaction is solved using the Crank Nicolson scheme in both ways. A detailed description and validation of the CFD flow solver EVA is given in [92]. Both codes are used in this paper to investigate the effects of fluid-structure interaction for a wave impact.

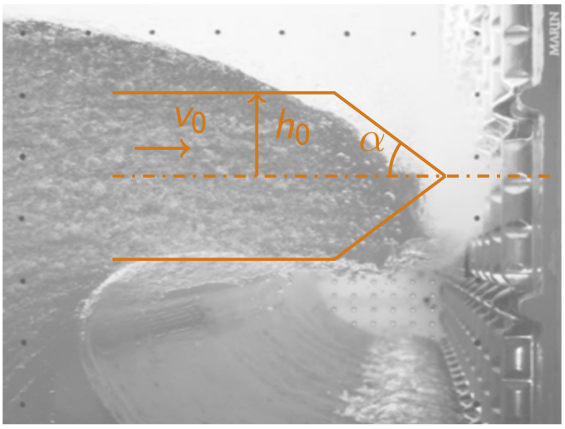

Figure 6.1: Wave impact from [59]. The orange lines represent the cut-off wedge impact which is simulated in this paper. The cut-off wedge has an initial constant velocity v_0 towards the wall, an angle α and an initial height h_0.

6.1 Method

The starting point is the Wagner impact model, which assumes an initial shape and constant velocity. It then calculates the flow and wall pressures using some perturbation method [68]. However, such a solution may not be feasible for the coupled problem, in which the relative velocity between structure and fluid is not constant. We can however take the same starting conditions to construct a comparable model which is easier to solve. The following is assumed:

- The wave impacts are perpendicular to the wall, and are symmetric with respect to the axis normal to the wall.
- Water height and velocity are prescribed along the normal of the wall, and are only a function of the distance to the wall.
- Gravity and air are disregarded

Gravity is kept in the derivation of the equations of motion in order to be in line with literature.
For now, assume that the gravity is retained, then it turns out that this gives the non-hydrostatic shallow water equations [104, 88, 52]. In these equations part of the pressure is caused by the vertical acceleration of the fluid. Therefore the assumption of Wagner, disregarding gravity for an impact, can be used, and comparison is possible.

6.1.1 Fluid equations of motion

A similar approach is taken to derive the fluid equations as in [52], only here a flat bottom is assumed representing the symmetry of the impact. The starting

point of the Fluid model are the Euler equations:

$$u_{,x} + w_{,z} = 0 \qquad \text{Continuity} \tag{6.1}$$

$$u_{,t} + uu_{,x} + wu_{,z} = -p_{,x}/\rho \qquad \text{Momentum x} \tag{6.2}$$

$$w_{,t} + uw_{,x} + ww_{,z} = -(g + p_{,z}/\rho) \qquad \text{Momentum z} \tag{6.3}$$

where u, w are the velocity fields in x, z direction, and $u_{,x}$ denotes the derivative of u to x. The kinematics are defined as:

$$u = U,\ w = z\frac{\dot{H}}{H} \tag{6.4}$$

where H is the free surface level and $\dot{H} = H_{,t} + uH_{,x}$. Therefore the velocity field of w interpolates the velocity at the free surface to a point in between. Instead of having to define u, w over the complete wet field we now only have to define it over the x axis, hence the problem is reduced from two dimensional to one dimensional. In order to solve the equations of motion we need to loose the z that appears in all equations due to w. Therefore we integrate all equations over the height, which is similar to using the method of weighted residuals in one direction [35]. The height averaged vertical velocity is:

$$W = \frac{1}{H}\int_0^H w\ dz = \frac{1}{H}\int_0^H z\frac{\dot{H}}{H}\ dz = \frac{1}{2}\dot{H} \tag{6.5}$$

We can now average the continuity equation over the height:

$$0 = \int_0^H u_{,x} + w_{,z}\ dz = \dot{H} + HU_{,x} \tag{6.6}$$

$$= H_{,t} + (UH)_{,x} \tag{6.7}$$

and momentum x equation:

$$\int_0^H u_{,t} + uu_{,x} + wu_{,z}\ dz = \int_0^H -p_{,x}/\rho\ dz \tag{6.8}$$

$$H(U_{,t} + UU_{,x)} = -f_{,x}/\rho \text{ with } f = \int_0^H p\ dz \tag{6.9}$$

Note that in the latter, the atmospheric pressure is equal to zero. Equation 6.3 can be simplified, by substituting the kinematics:

$$-(g + p_{,z}/\rho) = w_{,t} + uw_{,x} + ww_{,z} \tag{6.10}$$

$$= z\left(\frac{\dot{\dot{H}}}{H} + \frac{\dot{H}^2}{H^2}\right) \tag{6.11}$$

$$= z\left(\frac{\ddot{H}}{H} - \frac{\dot{H}^2}{H^2} + \frac{\dot{H}^2}{H^2}\right) \tag{6.12}$$

$$= z\frac{\ddot{H}}{H} \tag{6.13}$$

This equation can be further simplified, by weighing with z and integrating over the height. We weigh with z in order to end up with the average wall force f at the left hand side.

$$\int_0^H -z(g + p_{,z}/\rho)\, dz = \int_0^H z^2 \frac{\ddot{H}}{H}\, dz \tag{6.14}$$

$$-\frac{1}{2}gH^2 - [zp]_0^H/\rho + \int_0^H p/\rho\, dz = \int_0^H z^2\, dz \frac{\ddot{H}}{H} \tag{6.15}$$

$$-\frac{1}{2}gH^2 + f/\rho = \frac{1}{3}H^2\ddot{H} \tag{6.16}$$

$$\tag{6.17}$$

Here we could use the assumption that $\ddot{H}$ is small leads to the shallow water equations. However, we substitute the definition of W into this equation of motion, giving:

$$-\frac{1}{2}gH^2 + f/\rho = \frac{2}{3}H^2\dot{W} \tag{6.18}$$

To summarize, we have the following equations that describe the fluid behavior:

$$\begin{aligned} H_{,t} + (UH)_{,x} &= 0 \\ \rho H(U_{,t} + UU_{,x}) &= -f_{,x} \\ \rho\frac{2}{3}H^2\dot{W} &= -\frac{1}{2}\rho g H^2 + f \\ \dot{H} &= 2W \end{aligned}$$

6.1.2 Implementation

The fluid model is discretized with a fractional step method. The first step, from t_n to t_* is pure convection, all right hand side is at t_n:

$$\frac{H^* - H^n}{\Delta t} = -HU_{,x} - UH_{,x} \tag{6.19}$$

$$\frac{U^* - U^n}{\Delta t} = -\frac{1}{\rho H}f_{,x} - UU_{,x} \tag{6.20}$$

$$\frac{W^* - W^n}{\Delta t} = \frac{3}{2\rho H^2}f - UW_{,x} \tag{6.21}$$

The second step is to proceed from t_* to t_{n+1}, while enforcing the incompressibility condition. It is assumed the wave height is not changing in the second step:

$$H^{n+1} = H^* \tag{6.22}$$

$$\rho H\frac{U^{n+1} - U^*}{\Delta t} = -f^c_{,x} \tag{6.23}$$

$$\frac{2}{3}\rho H^2\frac{W^{n+1} - W^*}{\Delta t} = (f^c - \frac{1}{2}gH^2) \tag{6.24}$$

$$0 = 2W^{n+1} + H^* U^{n+1}_{,x} \tag{6.25}$$

where f^c is a pressure correction, used to enforce continuity. The boundary conditions are added here and the linear system is solved for the new time step t_{n+1}. The last step is to correct the pressure:

$$f^{n+1} = f^n + f^c \tag{6.26}$$

Equations 6.23-6.25 can be combined to yield an equation for f^c. First, Equations 6.23 and 6.24 are rewritten for U^{n+1} and W^{n+1}. This is then submitted into Equation 6.25, giving the following equation:

$$\frac{\rho}{\Delta t}(2W^* + HU^*_{,x)} - \frac{3}{2}g = 3\frac{1}{H^2}f + \frac{H_{,x}}{H}f_{,x} - f_{,xx} \tag{6.27}$$

To solve the system we need boundary conditions which are on the velocity, not on the pressure. Therefore the system is transformed to have on the boundaries the first derivative of the pressure as unknown. It allows us to prescribe the change in velocity that the pressure correction needs to deliver.

The equations are solved using collocated vertex centered finite differences. Discretization is upwind for convective terms, and central for the terms in Equation 6.27. The vertices are spaced evenly, dividing the $L = 1$ m domain into 250 parts of equal length.

6.1.3 Structure equations of motion

As a start the structure is taken as mass-spring system:

$$m\ddot{s} + c\dot{s} + ks = f \tag{6.28}$$

with $s = s(t)$ as displacement, mass m, damping c, stiffness k and external force f. The equations of motion are converted to state space form ($\dot{u}(t) = Au(t)+g(t)$) and integrated over time using Crank-Nicolson:

$$u_1 = u_0 + (Au_1 + g_1 + Au_0 + g_0)\,dt \tag{6.29}$$

where subscript 1 denotes the new state and 0 the old state, matrix A describes the system dynamics and $u(t)$ the state of the system. This method is chosen because it is stable and conservative.

6.1.4 Coupled solution

The structure is placed at the edge of the fluid domain $x = L$. For the wave impact problems investigated here, we assume the deformations of the structure are small, so that we need not modify the fluid domain. The inflow / outflow velocity of the fluid is made equal to the velocity of the structure: $U(x = L, t) = \dot{s}(t)$. The force on the structure is equal to the force on the wall of the fluid: $Q(x = L, t) = f(t)$.

The actual coupling takes place in the pressure correction step of the fluid. The structure is added to the system of equations of the fluid, thus solving both at the same time. This avoids sub-iterations or the choice of under relaxation parameters required for a partitioned solver and gives a robust implementation. The resulting system of equations is directly solved without iterations.

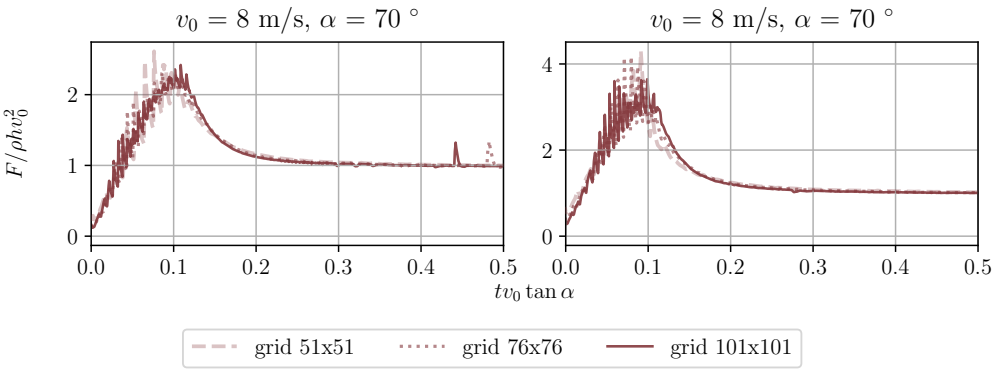

Figure 6.2: Grid convergence of force on the wall for the two impact angles for EVA.

6.2 Uncoupled wedge impact

Following the initial investigation of the code, a number of important parameters can be deduced. First, the rise time of the load. At the start the change from wedge to rectangle is at $x_c = h_0/\tan\alpha$. The starting velocity is v_0, so if the cut-off wedge would move along with the flow, the arrival at the wall would be:

$$t_c = \frac{x_c}{v_0} = \frac{h_0}{v_0 \tan\alpha} \tag{6.30}$$

After this point the force on the wall should go from wedge-dominated to rectangle-dominated. Second, we investigate the load level. If an infinite wedge impact on a wall is investigated with the Wagner model, the force would be [107]:

$$F(t) = C(\alpha)\rho v_0^3 t \tag{6.31}$$

where $C(\alpha)$ is a constant depending on the wedge angle, v_0 the velocity at far field and t the time. On the other hand, if there was only water being bent off by the wall, conservation of momentum would give:

$$F(t) = \rho h_0 v_0^2 \tag{6.32}$$

In the worst case scenario the wedge behavior will continue up to t_c, giving the maximum force:

$$T_{\max} = \frac{C(\alpha)\rho v_0^2 h_0}{\tan\alpha} \tag{6.33}$$

To better compare the results we decide to present them in a dimensionless form, when applicable. The dimensionless time τ and force ϕ are defined as:

$$\tau = tv_0 \tan\alpha, \ \phi = \frac{F}{\rho h_0 v_0^2} \tag{6.34}$$

Here we choose to make the force dimensionless by the steady state force on the wall instead of the peak force, because the former does not depend on the impact angle. Additionally we could have included the water height h_0 in the dimensionless time τ, but this would be a simple scaling since this parameter is not changed in this paper. All calculations are performed with water density $\rho = 1000$ kg/m^3, an initial height $h_0 = 0.2$ m.

Due to the assumptions made in modelling the fluid flow there is no straightforward validation problem. However, we believe that the comparison between the reduced order model and EVA give enough confidence to trust this method for optimization or probabilistic evaluations. Because EVA is validated for fluid flow it is possible to make the link with reality. Additionally, this model is meant to predict the relevant trends, and the effect of taking hydro-elasticity into account. The next step could be to extend the model in a way that allows direct comparison with experiments.
A convergence study for EVA for the investigated wedge angles is shown in Figure 6.2. This figure shows on the horizontal axis time and vertical axis the dimensionless total force on the wall. In this paper all calculations are performed on a 1 by 1 m grid, with water ($\rho = 1000$ kg/m^3) and 'air' ($\rho =$ 1e-8 kg/m^3). The air density is chosen to be close to zero, which matters for the comparison with the NHSWE code in which there is no air. The grid resolution as varied between 51, 76 and 101 cells in each direction on a Cartesian grid, which are the values 51x51 and so forth in Figure 6.2. At the same time the time step was appropriately scaled by enforcing CFL < 0.1 at all times. The wall force is roughly the same for all grid resolutions, however the noise decreases when the grid is more refined. The noisy behavior, is caused by local pressure spikes. These are caused by the correction to the explicit momentum terms to remain divergence free and is associated with the large density ratio. For the fully coupled scheme, Crank Nicolson is used which relaxes these local pressures.

Figures 6.3 and 6.4 show the force on the wall for an impact with $v_0 = 8$ m/s with $\alpha = 60°$and $70°$. These impact velocities and angles are chosen because they have the impact duration that causes hydro-elasticity to have an effect. First the impact force follows the result of [107], as shown by the two lines indicating 'ZF93'. They are analytical Wagner solutions to the impact problem. Although for the wedge water entry case [107] and the plate wedge water impact case (Figures 6.3 and 6.4), the roles of the fluid and the structure are reversed. For wedge water entry the body is penetrating the flat fluid surface and for plate wedge water impact a wedge shaped fluid surface is impacting a flat body - the way the impact force develops is similar.

Both codes, NHSWE and EVA, adhere quite well to the initial angle. At some point the slope decreases and the maximum force is reached and this depends highly on the angle α as mentioned before. Finally, all scaled impact forces converge to unity as expected. These tests have been repeated using different impact velocities but yield the same curve, meaning our aforementioned scaling factors

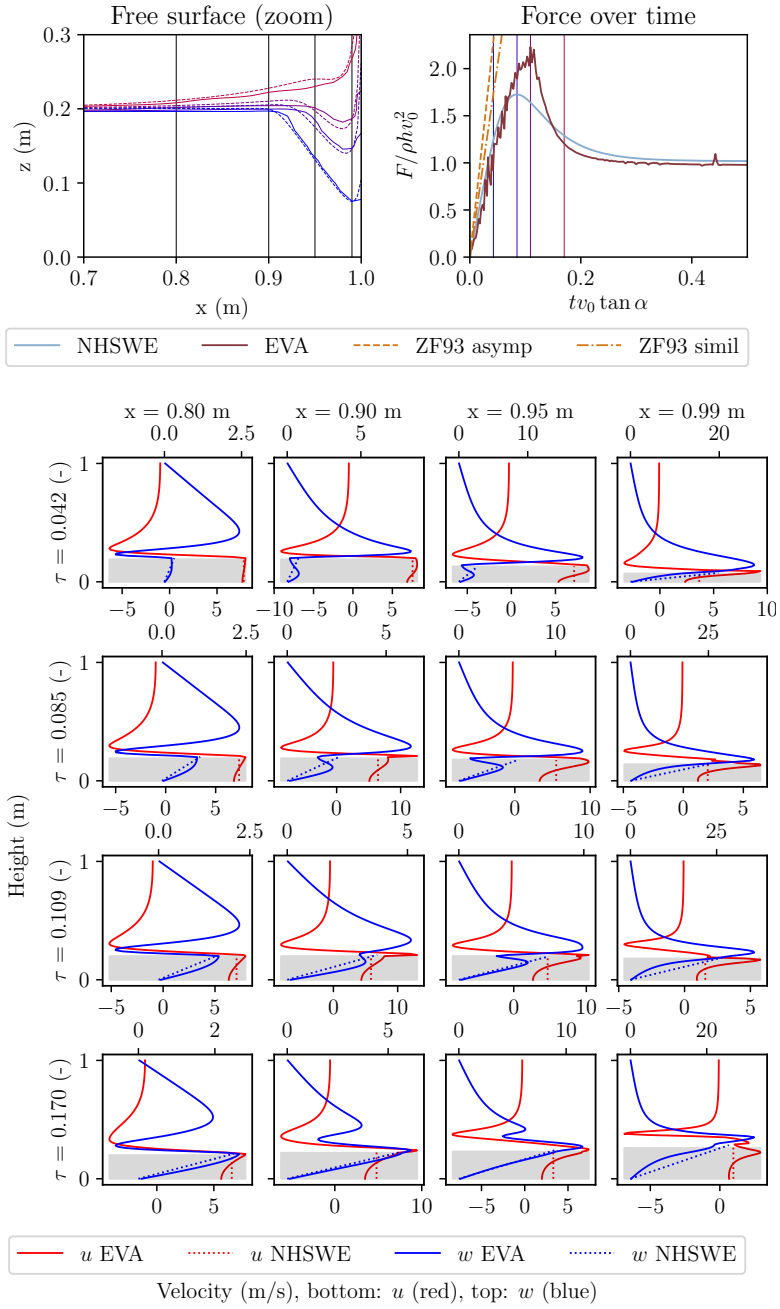

Figure 6.3: Velocity over height for impact with $v_0 = 8$ m/s and $\alpha = 60°$

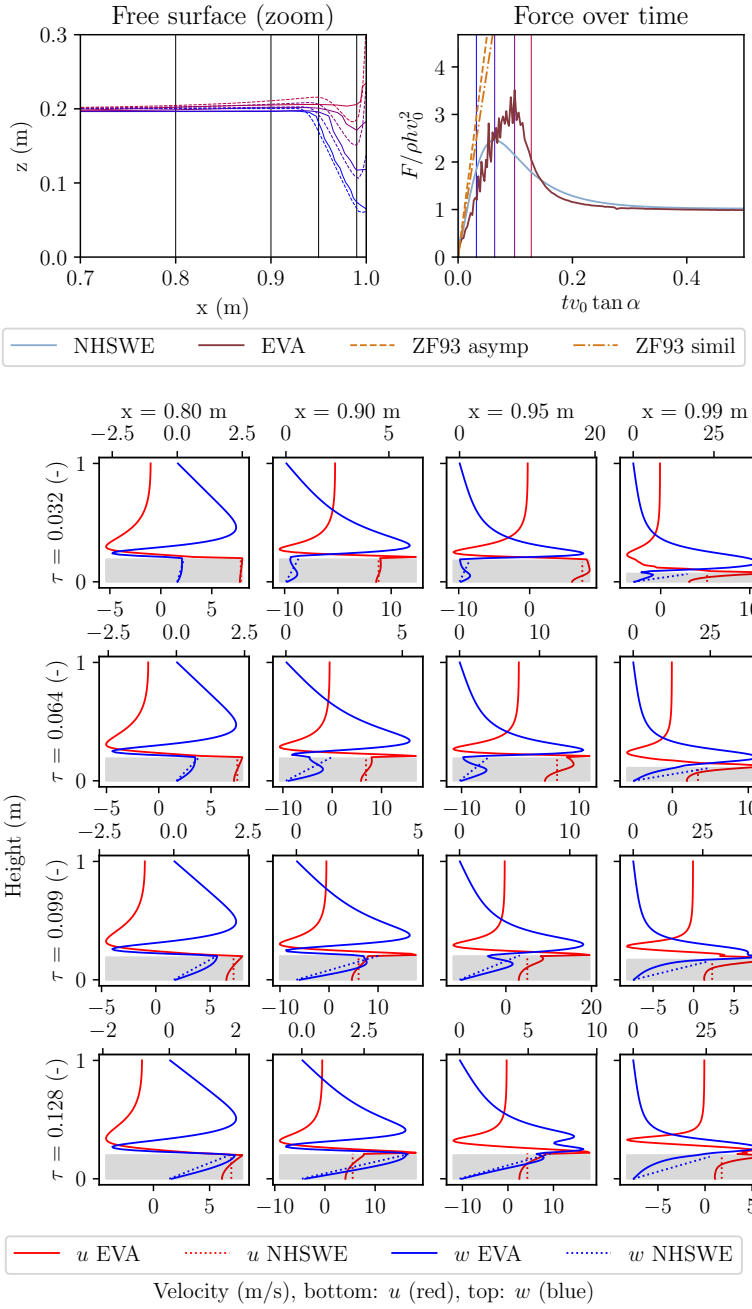

Figure 6.4: Velocity over height for impact with $v_0 = 8$ m/s and $\alpha = 70°$

work. It is clear that EVA shows a much higher peak value, up to 40%. Even disregarding the spikes in the force of EVA, likely caused by the fluid going into the next cell, the maximum force is about 30% higher. However, it should be noted that the difference in total impulse is within 3% percent because the same mass of fluid has to be turned around. In order to explain why there is a difference in maximum force, we need to look at the velocity profiles.

We know that there is one big difference between the models: EVA has multiple cells over the height of the domain, whereas NHSWE has only one. This allows EVA to have more local details, which we know the wave impact problem has [96, 24]. The different velocity fields at four places are plotted in Figures 6.3 and 6.4, for four times (before max, max NHSWE, max EVA and near steady). These positions and times are indicated in the free surface and force over time plots in these Figures. In the second row of Figures 6.3 and 6.4 we can observe why the peak results are so different. The two rightmost graphs show that the horizontal velocity in EVA is higher where it is not obstructed by other parts of the fluid which are in contact with the wall. In EVA we can see the bottom part of the fluid column being stopped by the wall while the top is still progressing. At the same time, the NHSWE model requires the complete height of the column to be stopped at the same time. This requires compared to EVA a higher force from the start, but as total momentum is conserved, this leads to an earlier decay.

When most of the fluid stream is bent off in the bottom row, the initial wedge shape is no longer visible and both codes yield almost the same force. The velocity profiles become similar again, except for some local details.

Summarizing, the upward and downward slopes seem the same, the response is of the same order of magnitude and the impulse is the same because the same amount of fluid is redirected. The difference then comes from the higher resolution in EVA, which models more accurate the velocity profiles due to the sharp bent in the flow, see Figure 6.3, which is not as well modelled by NHSWE as by EVA. A downside of EVA are the pressure spikes that increase the absolute maximum. However, as the total impulse is nearly the same, as is the velocity profile at the end of the simulation, we believe it is worthwhile to investigate the coupled response of these wave impact codes with a moving wall.

6.3 Coupled wedge impact

We choose to investigate a subpanel of the Mark III CCS [49, 38], with properties derived as described in [11]. The properties are determined without the primary or secondary membrane, and assuming the bottom plywood rigid and rigidly mounted to the ship inner hull. We select the first vibration mode to represent the response of the structure, because it is just the top plywood moving up and down rigidly. It has the lowest natural frequency of all the modes, meaning the modal stiffness is lowest and it is the most likely to respond. This gives a modal mass of 7.86 kg and a stiffness of 125 MN/m, resulting in a natural frequency of

Table 6.1: Overview of the simulations performed with EVA and the simplified NHSWE model, all with $h_0 = 0.2$ m.

	α (deg)	v_0 (m/s)	solver	coupled	max f (N)	max s (m)	T_l (s)	s_l (m)
0	60	8	EVA	one-way	30973	0.000230	0.00158	0.000116
1	60	8	EVA	two-way	29244	0.000229	0.00450	0.000115
2	60	8	NHSWE	one-way	22094	0.000178	0.00158	0.000106
3	60	8	NHSWE	two-way	22407	0.000180	0.00534	0.000113
4	70	8	EVA	one-way	46667	0.000333	0.00154	0.000104
5	70	8	EVA	two-way	42157	0.000321	0.00432	0.000157
6	70	8	NHSWE	one-way	31470	0.000262	0.00157	0.000114
7	70	8	NHSWE	two-way	32416	0.000264	0.00457	0.000125
8	60	16	EVA	one-way	122549	0.000920	0.00097	0.000430
9	60	16	EVA	two-way	122589	0.000976	0.00485	0.000620
10	60	16	NHSWE	one-way	88377	0.000776	0.00157	0.000484
11	60	16	NHSWE	two-way	95069	0.000784	0.00485	0.000555
12	70	16	EVA	one-way	189220	0.001303	0.00156	0.000585
13	70	16	EVA	two-way	179790	0.001392	0.00417	0.000982
14	70	16	NHSWE	one-way	125882	0.001328	0.00157	0.000707
15	70	16	NHSWE	two-way	150883	0.001358	0.00399	0.000875

634 Hz or a period of 0.00158 s. The subpanels are actually 340 mm squares, but here we will take the entire wall as representing one subpanel.

6.3.1 Comparison with EVA

Figure 6.5 shows the load and response of the CCS to a wave impact with velocity v_0 of 8 and 16 m/s, and angles α of 60°and 70°, the water height $h_0 = 0.2$ m. These parameters are chosen because they show an effect of including the coupling in some cases and no effect in others. Time, force and response are made dimensionless with respect to rise time, steady load and static response respectively. The dimensional response is summarized in Table 6.1. We already know that EVA has a higher maximum force, yet the impulse of both models are nearly the same. Here it is shown how the response is changed by a different load shape with the same total impulse. First we describe the difference in response between the models, because the difference in wall force comes from the difference in response.

The response of the wall is shown in Figure 6.5b and the response becomes increasingly dynamic with increasing angle α or velocity v_0. As the impact has a higher velocity or steeper angle, the interaction is increasingly important. This is based on two load characteristics: the load rise time is such that it easier excites the structure and the load magnitude such that it is felt by the structure. What is however strange is that the difference in response of the one way and coupled solutions is not the same for EVA and the reduced order model. One reason for this is that the loads have the same force integral but with different maxima. Hence, the peak and force as function of time are different, and these parameters are of importance for the dynamic response. Another reason is that the run up along the wall is different, meaning that if the structure starts to move, it has a different added mass moving along.

We also see that the response of the structure after the impact does not damp out. Over time mass enters the domain with a velocity, therefore adding energy. We expect that the coupled system response will not die out, so a sensible cut-off time should be taken. A simple proposal is the time when the water column in front of the structure exceeds the structure size, or when the uncoupled wall force stabilizes (within a margin) to the expected steady wall force of Equation 6.32. Here, we took a dimensionless time of $\tau = 0.5$.

For the 8 m/s impact velocity the impact forces almost coincide for coupled and uncoupled, just the 70°is shows a deviation for all time. The 8 m/s, 60°impact is just slightly decreased by the moving structure. With the fast 16 m/s impact a much larger difference is observed, clearly showing the vibration of the structure in the load. We can see that the coupled solution can result in a higher load on the structure than the uncoupled solution. There is a simple explanation: the structure moves along with the fluid but at some point has to come back. When it does, the relative velocity of the fluid with respect to the structure is

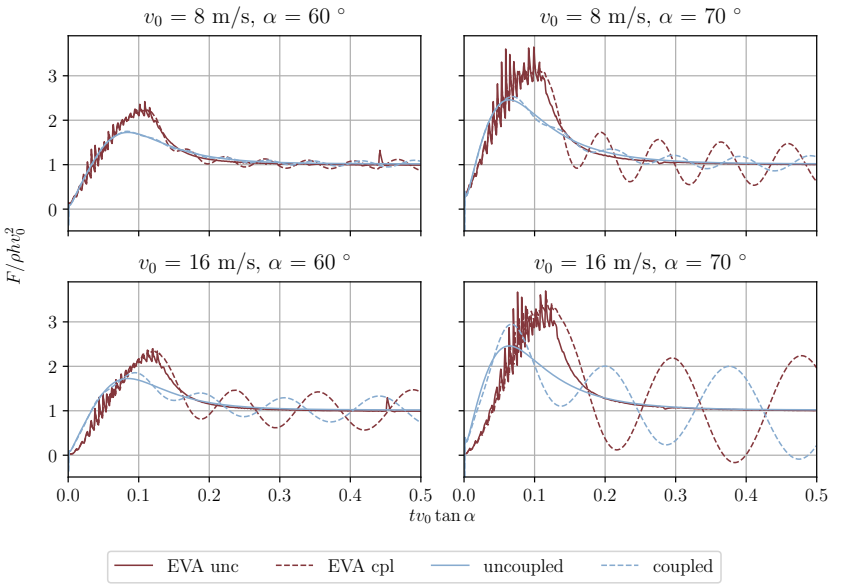

(a)

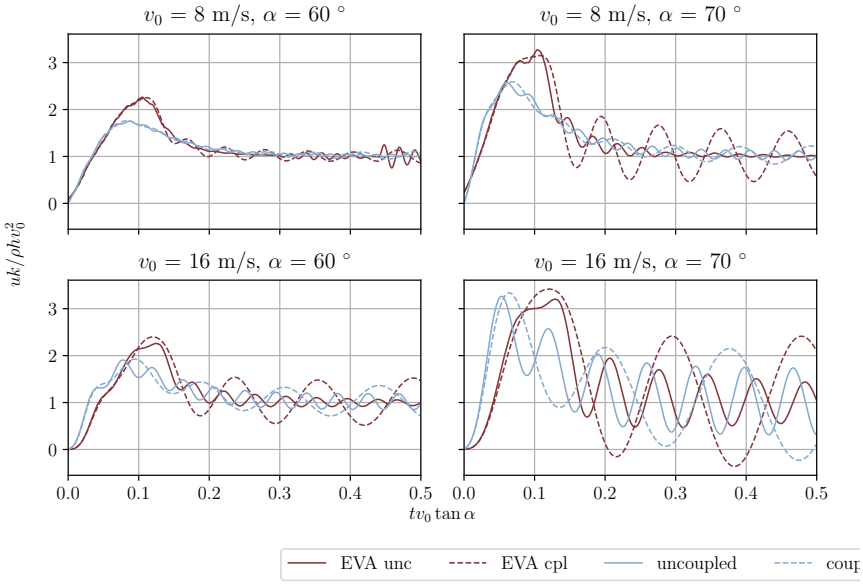

(b)

Figure 6.5: Wall force and response for uncoupled and coupled impacts at 8 and 16 m/s with 60°and 70°.

increased, therefore increasing the load. This all happens at a time scale where the dynamics of the structure is important. In other words: whether the load is increased due to FSI is very dependent on the dynamics of the load and structure.

Finally, it should be noted that Table 6.1 gives the duration of the final vibration period. We can see a big difference between the coupled and uncoupled structures, where the coupled response is almost the same for both solvers. Physically this means the added mass for both solvers is approximately the same. Furthermore, even though the impact maximum is equal, the NHSWE solver does say something about the effect of FSI and it could be a valuable tool to check the system sensitivity with respect to the coupling.

From Table 6.1 we can also see the height of the last peak for coupled or uncoupled response is the same. It means that we do predict approximately correctly how much energy is absorbed by the structure, and whether the FSI is amplifying the response or diminishing it. The added benefit of the reduced order model is that it is much faster than the high fidelity method in doing so, in the order of a few minutes versus a day of computation time.

6.3.2 Variation of impact angle and velocity

The low fidelity model can be used to check the effect of different angles and impact velocities, as an example of a sensitivity study. Figure 6.6 shows a study of the difference between coupled and uncoupled impacts for angles between $\alpha = 45° \ldots 80°$ and $v_0 = 2 \ldots 32$ m/s. The other parameters such as fluid density, fluid height and the structural parameters are kept the same as previously. In the graphs a contour plot of the ratio of force or displacement is shown, the coupled result divided by the uncoupled one. Also contours are shown of the critical time t_c, as defined in Equation 6.30, which was earlier defined as a measure when the wedge has fully been absorbed by the wall. Only results related to the peak of the wedge impact are used, not the (numerical) direct impact nor any vibrations after $1.25 \cdot t_c$.

It is clear from the both graphs that the lines of the ratio have similar alignment as the lines of the critical time. Especially the critical time $t_c = 0.005$ s is close to the wet natural period, and $t_c = 0.002$ is close to the dry natural periods (see Table 6.1). This indicates that whether FSI affects the result depends on the critical time of the loading compared to the natural period of the structure. Not a surprising conclusion, but an important one considering how easy it is to calculate the critical time and natural period of the structure.

It is clear from the left plot in Figure 6.6 that the maximum force of the coupled calculation is in almost all cases higher than for the uncoupled calculation. As mentioned before, this is attributed to the structure first moving along with the impact, but after some time coming back, that is when the maximum force is

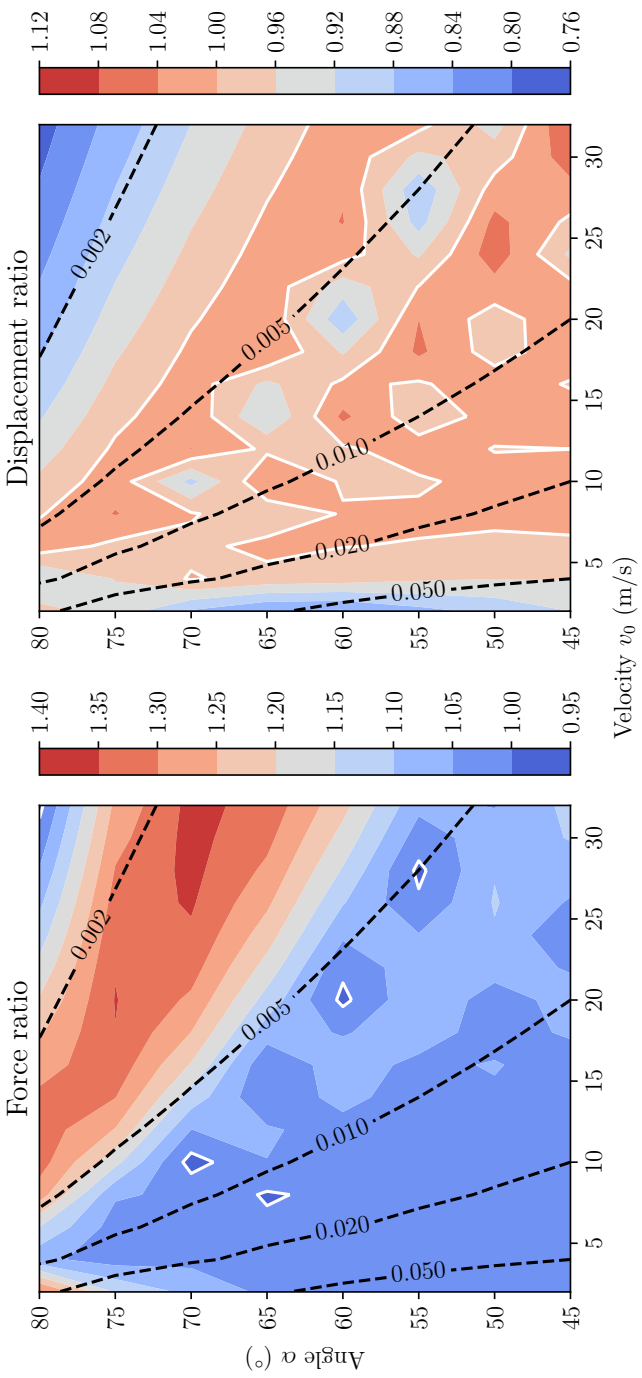

Figure 6.6: Contour plot of the ratio between coupled and uncoupled force on the wall and displacement of the wall. If the value is larger than unity the force or displacement in the coupled case is higher than for the uncoupled case. Unity is marked with the white contour lines. The black dashed lines are the critical times from Equation 6.30. The initial height is kept constant at $h_0 = 0.2$ m.

reached. According to this figure this mostly happens when the critical time is between the wet and dry natural period.

The right graph is much harder to generalize. It looks like higher angles or velocities might show more that the FSI coupling decreases the response. But, for the other combinations of angle and velocity there is no clear trend, which means that whether the structure is sensitive to FSI depends on the specific impact parameters.

6.4 Conclusions

Wave impacts onto the wall of an LNG tank are limiting for the design. The interaction between the wave and the wall could increase or decrease the response of the structure. High fidelity models for fluid-structure interaction are typically computationally expensive, which is why we propose a reduced order model for the fluid. The reduced order model is coupled to a reduced order model for the structure, being an order of magnitude faster than the high fidelity model. This reduced order model makes it possible to estimate quickly the effect of hydroelasticity during a wave impact.

We consider as impact case a cut off wedge, as a model for the wave crest hitting the wall. The reduced order model predicts the same total impulse and added mass as the calculations with EVA, which is an in-house developed CFD code. It shows lower force than EVA, yet it is usable to quantify the sensitivity of the structure response to fluid-structure interaction. This is possible because the total impulse and added mass are almost the same, leading to almost the same final excitation. The difference can be explained by the kinematic assumption used to arrive at the reduced order model and its influence on the maximum force.

An example of a sensitivity study is given, where impact velocity and angle are varied for the same structure. From these results it seems like the force in the coupled calculations is generally higher than for the uncoupled calculations. However, there is not such a clear trend for the displacement of the wall. The main conclusion is that there is no quick way estimate of the importance of fluid-structure interaction, as it depends strongly on the impact shape and velocity.

For future studies it is recommended to generalize the sensitivity analysis in the sense of dimensionless numbers, for instance the ratio of critical time to vibration period. Maybe in such cases it is easier to draw general conclusions, and look for areas where FSI is never important. Additionally, there are many improvements possible to the code used in this paper, such as better boundary conditions for the moving wall. In using this code it would be interesting to try different incoming wave shapes, to see if there are shapes which are less sensitive to variations.

Chapter 7

Conclusions and recommendations

Liquefied natural gas (LNG) an liquefied hydrogen are viable long term solutions to make the maritime industry less polluting. LNG being a cryogenic liquid is currently safely transported in specially insulated cargo tanks, owing their safety to the experience that exists with these tanks. The insulation is a sandwich structure called a cargo containment system (CCS). A different size of tank will be used for LNG as fuel. It is however not straightforward to scale all the loads and the response, as well as the existing safety factors, to a tank of a completely different size. One of the projected difficulties is in scaling of the interaction between fluid and structure (FSI). To alleviate this issue, this thesis presents a set of reduced order models that can help to better understand the scaling issues.

The interaction between fluid and structure goes as follows. First the structure is hit by a wave, then there is a submerged response, and the structure becomes dry again. Then there is free vibration until the structure is hit by another wave. During each phase different physics play a key role, meaning that different parts of the structure play a role. The research presented in this thesis focusses on two tracks: first to understand the fundamentals of the interaction, and second to create and apply reduced order models for the specific challenges within sloshing and CCS design.

In the following the conclusions and recommendations are discussed in three parts. The first is about the experiments that have been performed. Second are the reduced order models for the CCS and the interaction with an impacting wave. Finally there are conclusions stemming from an overall perspective on the work in this thesis.

7.1 Experiments

The first experiment uses monochromatic waves to excite a pendulum several times in a row. Regardless of the wave length investigated, the monochromatic waves can be generated with good repeatability. Hanging a pendulum in these waves gives an easy and reproducible experiment that serves as a basic maritime related FSI case. Only the periodic part of the response was investigated, after start-up and before reflections. It was found that the experiments are very repeatable, and that most of the energy transfer takes place during the submerged part of the interaction. A reduced order model was developed to predict and explain the experimental results, using a pendulum, Morison equation for the loads and a wetness function for the submergence. The simple wetness function introduced in this thesis suffices to capture the nonlinear effects of changing wetness. It should be noted that no additional forces for water entry or exit were taken into account and good agreement was reached between experiment and model.

The second experiment was with focussed waves, keeping the rest of the setup the same. The waves were focussed by sending small packets of three wave periods towards the pendulum. While there was little variation in wave height before the focussed waves broke, there was a significantly larger variation after breaking. The variability of the response depended on the breaking point with respect to the pendulum, causing a different impact every time although the focal point was the same. It is likely that there is a large influence of aeration on the variability because the experiments with more aeration gave more variability.

With the monochromatic wave and the focussed wave there was additional variability in the response of the pendulum compared to the variability of the wave. Also, even though wave impacts and the resulting response are notoriously difficult to model numerically, simple models were presented that give a decent estimate for the response. These models have tuning parameters, which were kept the same for both reduced order models, producing similarly accurate results. Water entry and exit were not modelled, but were present in the experiment. Because the reduced order model does not need these loads to predict accurately the response, the hypothesis is posed that the submerged behaviour is relatively the most important. This conclusion is reinforced by a lack of correlation between impact angle or velocity and maximum response in the focussed wave experiment.

It is recommended to repeat the experiments with more repetitions, especially for the aerated waves. Then also the free surface should be measured more accurately and at more places to perform a more detailed analysis of the nonlinear interactions, and quantify the loss of energy due to dissipation. Furthermore, the aeration of the wave should be measured and linked to the wetness function. Additionally, all the experiments should be done with scaled properties, as well as a variety of mass and stiffness properties. With this a scaling law could be found that gives insight how to set up these experiments effectively. Because the driving phenomenon is a wave impact, the assumption would be to use Froude scaling

for the waves, with correct modal mass ratio's, as well as the same ratio between forcing period and natural response period. For a single degree of freedom system such as the pendulum this should be possible, but for more complex structures this will be challenging. However, for another wave shape the compressibility or surface tension could be more important, requiring similar Mach or Weber numbers.

Also, other types of experiments can be defined. For instance, instead of hanging the tube as part of a pendulum, the tube can be held by a tensioned string, both from the top and bottom. This decreases the vibration period as well as the expected motion, bringing the characteristics closer to that of a wall.

7.2 Reduced order models

A reduced order model for the CCS is devised, based on a beam-foundation model. In this model the foundation reflects an elastic material with a deformation model over the height. The first vibration mode of the CCS is the top plywood moving up and down. Its displacement field and natural frequency was determined taking into account the temperature dependent elastic modulus and a uniform mass distribution, with point masses for the top plywood. It was then assumed that the displacement field over the height can be described with this first vibration mode, with a different magnitude at every point. Hence, this vibration mode is the only one that is correctly modelled, but a small error is introduced for the higher vibration modes.

A realistic sloshing impact load is applied to the structure, and the response compared with the response from a FEM analysis. The main advantage of the reduced order model is that it gives a conservative estimate for the stress inside the structure. Hence, this reduced order model can be used for screening the loads. While the model is conservative on stress, it underestimates the deformations compared to the finite element model. In other words the structure in the reduced order model is too stiff compared to the FEM analysis.

An additional analysis is performed to investigate the sensitivity of this model with respect to impact loads that are at an angle with respect to the horizontal relaxation grooves. It was found that there is a small influence of the angle on the indentation of the CCS subpanel. The influence of the angle on the stress is larger, the oblique load for some load cases giving more than 50% higher stress compared to the straight load.

It is recommended to look closer at the stress concentrations at the top and bottom in order to capture more failure modes with this model. When all critical failure modes are included the CCS model can be used not only to screen the loads, but also find an optimal design. Another model could be constructed for the effects of the direct impact, which is far more localized than the model used here. Finally, it is recommended to take into account the stiffness of the part of

the ship structure behind the CCS. This will have a large influence on the natural frequencies, as well couple different physics that happen at different positions along the tank wall. For instance the wave impact at a high point with added mass due to the still water level at a low point.

Another reduced order model is devised for the wave impact on a wall, based on the shallow water equations. Here a velocity field over the fluid height is assumed, and the rest of the equations are derived from that. The model does not predict the maximum impact force correctly, but does predict the transferred momentum from the fluid to the wall. Also the wet natural frequency is predicted well.

This model is compared with an in-house CFD code, in which the same assumptions for FSI are used. In general, no relation was found that can predict when the interaction is important or not. It was however observed that impacts in which the interaction is taken into account do not always have a lower or higher response. Instead of focussing on a general rule of thumb, the interaction should always be investigated on a case by case basis.

A big improvement to the analytical wave impact model would be to use more basis functions over the height, in order to better approximate the real velocity field over the height. The impact shape is now a cut off wedge, a more rounded shape is probably more realistic to look at. Also, the initial shape of the model is now chosen to show the different responses of the system, but should be linked to actual wave impacts.

7.3 Fluid-structure interaction and sloshing wave impacts

Now the question is how to interpret the importance of FSI for wave impacts in sloshing? For many cases it would make sense to start at the time and length scales of the load and response. This is however only part of the story, since the presented problems have significant added mass. Hence, the natural frequencies can also significantly change, so that the response with FSI is higher than without, making loads more relevant than they were.

One important conclusion from this thesis is that the interaction adds variability, meaning the response of the structure has larger variability than that of the load enacted by the fluid. This was unexpected since the structure was assumed to integrate out the fluid behaviour in time and space.

In this study the propagation of variability is studied experimentally. It is recommended to perform similar studies numerically, with the same wave input and a perturbed free surface, for instance due to a slightly different incoming wave. This will give a better impression of where the variability in the experiments comes from.

For sloshing it is recommended to build reduced order models for the other loading and failure mechanisms, and see what the sensitivity is to taking the fluid-structure interaction into account. Then the models can be combined to see if the loading mechanisms influence each other. Reduced order models like the ones presented in this thesis can then be used to design safe tanks for transportation of LNG. However, more fundamentally, they give insight in the relevant parameters and relations that define the loading and response of the structure.

Finally, it should be noted that here only the (linear) elastic behaviour of the structure is investigated. A consequence of this modelling approach is that the structure is always able to withstand the loads, only limited by a maximum allowable stress or strain. However, in reality, at some point there will be failure and the structure will lose the capacity to withstand more loads. This means that the structure will deform much more than it did in the linear regime, leading to stability issues. If the wave has enough energy to push even further then the structural integrity can be lost, causing a leak of LNG.

References

[1] American Bureau of Shipping. Strength Assessment of Membrane-Type LNG Containment Systems Under Sloshing Loads. Technical report, February 2014. Guidance note.

[2] T. Andreeva, P. Alevras, A. Naess, and D. Yurchenko. Dynamics of a parametric rotating pendulum under a realistic wave profile. *International Journal of Dynamics and Control*, 4(2):233–238, 2016.

[3] ANSYS, Inc. Mechanical APDL Documentation, 2015. Academic Research, Release 16.2.

[4] K. Ariyarathne, K. Chang, and R. Mercier. Green water impact pressure on a three-dimensional model structure. *Exp Fluids*, 53, 2012.

[5] A. Arswendy and T. Moan. Sloshing Response of LNG Tank. In *Proceedings of the International Conference on Offshore Mechanics and Arctic Engineering*, 2006.

[6] R.A. Bagnold. Interim report on wave-pressure research. *Journal of the Institution of Civil Engineers*, 12:202–226, June 1939.

[7] S.S. Bennett, D.A. Hudson, and P. Temarel. The influence of forward speed on ship motions in abnormal waves : Experimental measurements and numerical predictions. *Journal of Fluids and Structures*, 39:154–172, 2013.

[8] H. Bogaert. *An Experimental Investigation of Sloshing Impact Physics in Membrane LNG Tanks on Floating Structures*. PhD thesis, Delft University of Technology, 2018.

[9] H. Bogaert, M.L. Kaminski, and L. Brosset. Full and Large Scale Wave Impact Tests for a Better Understanding of Sloshing - Results of the Sloshel Project. In *Proceedings of the International Conference on Ocean, Offshore and Arctic Engineering*, 2011.

[10] H. Bogaert, S. Léonard, M. Marhem, G. Leclère, and M. Kaminski. Hydrostructural behaviour of lng membrane containment systems under breaking wave impacts: Findings from the sloshel project. In *Proceedings of the International Offshore and Polar Engineering Conference*, volume 3, pages 98–108, 2010.

[11] R.W. Bos, J.H. den Besten, and M.L. Kaminski. A reduced order model for structural response of the Mark III LNG Cargo Containment System. *International Shipbuilding Progress*, 66:295–313, 2020.

[12] R.W. Bos and M.L. Kaminski. Comparing 2D and 3D linear response of a simplified LNG membrane cargo containment system. In *Proceedings of the International Offshore and Polar Engineering Conference*, pages 780–787, 2018.

[13] R.W. Bos and P.R. Wellens. Fluid structure interaction between a pendulum and monochromatic waves. *Journal of Fluids and Structures*, 2020.

[14] R.W. Bos and P.R. Wellens. Fluid structure interaction between a pendulum and focused breaking waves. *Physics of Fluids*, 33, 2021.

[15] E. Botia-Vera, A. Souto-Iglesias, G. Bulian, and L. Lobovsky. Three sph novel benchmark test cases for free surface flows. In *5th ERCOFTAC SPHERIC workshop on SPH applications*, pages 146–153, 2010.

[16] L. Brosset, Z. Mravak, M. Kaminski, S. Collins, and T. Finnigan. Overview of sloshel project. In *Proceedings of the International Offshore and Polar Engineering Conference*, 2009.

[17] G.N. Bullock, C. Obhrai, D.H. Peregrine, and H. Bredmose. Violent breaking wave impacts. Part 1: Results from large-scale regular wave tests on vertical and sloping walls. *Coastal Engineering*, 54(8):602–617, aug 2007.

[18] Bureau Veritas. Design sloshing loads for LNG membrane tanks, May 2011. Guidance note NI 564 DT R00 E.

[19] L.A. Carlsson and G.A. Kardomateas. *Structural and Failure Mechanics of Sandwich Composites*. Springer, 2011.

[20] M. Castellino, P. Sammarco, A. Romano, L. Martinelli, P. Ruol, L. Franco, and P. De Girolamo. Large impulsive forces on recurved parapets under non-breaking waves. A numerical study. *Coastal Engineering*, 136:1–15, jun 2018.

[21] Y. Cheng and C. Ji. Numerical simulation of violent breaking wave impacts on a moored offshore wind turbine foundation over nonuniform topography. *Physics of Fluids*, 32(10), OCT 1 2020.

[22] W.-L. Chuang, K.-A. Chang, and R. Mercier. Impact pressure and void fraction due to plunging breaking wave impact on a 2d tlp structure. *Exp Fluids*, 58, 2017.

[23] D.T. Cox and J.A. Ortega. Laboratory observations of green water overtopping a fixed deck. *Ocean Engineering*, 29(14):1827 – 1840, 2002.

[24] E. Cumberbatch. The impact of a water wedge on a wall. *Fluid Mech.*, 7:353 – 374, 1959.

[25] V.S. Deshpande and N.A. Fleck. Isotropic Constitutive Models for Metallic Foams. *Journal of the Mechanics and Physics of Solids*, 2001.

[26] Det Norske Veritas. Sloshing Analysis of LNG Membrane Tanks. Technical report, August 2014. Classification Notes No. 30.9.

[27] F. Dias and J.-M. Ghidaglia. *Slamming: Recent Progress in the Evaluation of Impact Pressures*, volume 50 of *Annual Review of Fluid Mechanics*. 2018.

[28] DNV GL. Gas fueled ships for cleaner shipping. `https://marine-offshore.bureauveritas.com/gas-fueled-ships-cleaner-shipping`, 2018. Accessed 19-11-20.

[29] G. Dolfo, D. Castex, and J. Vigué. Damping mechanisms of a pendulum. *European Journal of Physics*, 37(6), 2016.

[30] S. Draycott, G. Payne, J. Steynor, A. Nambiar, B. Sellar, and V. Venugopal. An experimental investigation into non-linear wave loading on horizontal axis tidal turbines. *Journal of Fluids and Structures*, 84:199–217, 2019.

[31] S. Ehlers, M. Guiard, J. Kubiczek, A. Höderath, F. Sander, R. Sopper, P. Charbonnier, M. Marhem, I. Darie, H. von Selle, J. Peschmann, and P. Bendfeldt. Experimental and numerical analysis of a membrane cargo containment system for liquefied natural gas. *Ships and Offshore Structures*, 12:S257–S267, 2017.

[32] O.M. Faltinsen. The effect of hydroelasticity on ship slamming. *Phil. Trans. R. Soc. Lond. A*, 355:575–591, 1997.

[33] O.M. Faltinsen. *Hydrodynamics of High-Speed Marine Vehicles*. Cambridge University Press, 2006.

[34] P.Y. Feng, N. Ma, and X.C. Gu. Long-Term Prediction Of Speed Reduction Due To Waves And Fuel Consumption Of A Ship At Actual Seas. In *Proceedings of the ASME 2010 29th International Conference on Ocean, Offshore and Arctic Engineering*, pages 1–10, 2017.

[35] B.A. Finlayson. *The Method of Weighted Residuals and Variational Principles*, volume 87 of *Mathematics in Science and Engineering*. Academic Press, 1972.

[36] M. Frihat, M.R. Karimi, L. Brosset, and J.-M. Ghidaglia. Variability of impact pressures induced by sloshing investigated through the concept of "singularization". In *Proceedings of the International Offshore and Polar Engineering Conference*, pages 901–914, 2016.

[37] Y. Frostig, M. Baruch, O. Vilnay, and I. Sheinman. High-Order Theory for Sandwich-Beam Behavior with Transversly Flexible Core. *Journal of Engineering Mechanics*, 118, 1992.

[38] T. Gavory and P.-E. de Sèze. Sloshing in Membrane LNG Carriers and its Consequences from a Designer's Perspective. *International Journal of Offshore and Polar Engineering*, 19(4):13–20, 2009.

[39] E. E. Gdoutos, I. M. Daniel, and K. A. Wang. Indentation failure in composite sandwich structures. *Exp Mech*, 42(4):426–431, 2002.

[40] E. Gervaise, P.-E. De Sèze, and S. Maillard. Reliability-based methodology for sloshing assessment of membrane LNG vessels. In *Proceedings of the International Offshore and Polar Engineering Conference*, pages 254–263, 2009.

[41] A. Ghadirian and H. Bredmose. Pressure impulse theory for a slamming wave on a vertical circular cylinder. *Journal of Fluid Mechanics*, 867:R1, 2019.

[42] GTT — Mark III systems. https://www.gtt.fr/en/technologies/markiii-systems. Accessed 2021-03-30.

[43] P.M. Guilcher, Y. Jus, and Brosset. 2D simulations of breaking wave impacts on a flat rigid wall - Part 2: Influence of Scale. In *Proceedings of the International Offshore and Polar Engineering Conference*, pages 741–754, 2018.

[44] P.M. Guilcher, Y. Jus, N. Couty, L. Brosset, Y.M. Scolan, and D. Le Touze. 2D simulations of breaking wave impacts on a flat rigid wall - Part 1: Influence of the wave shape. In *Proceedings of the International Offshore and Polar Engineering Conference*, pages 232–245, 2014.

[45] M. Hayatdavoodi and R.C. Ertekin. Wave forces on a submerged horizontal plate - Part I : Theory and modelling. *Journal of Fluids and Structures*, 54:566–579, 2015.

[46] M. Hayatdavoodi, K. Treichel, and R.C. Ertekin. Parametric study of nonlinear wave loads on submerged decks in shallow water. *Journal of Fluids and Structures*, 86:266–289, 2019.

[47] B. Hofland, M.L. Kaminski, and G. Wolters. Large Scale Wave Impacts On A Vertical Wall. In *Proc. of the ICCE*, 2010.

[48] R.A. Ibrahim. Assessment of breaking waves and liquid sloshing impact. *Nonlinear Dynamics*, 100(3):1837–1925, 2020.

[49] J.A. Issa, L.O. Garza-Rios, R.P. Taylor, S.P. Lele, A.J. Rinehart, W.H. Bray, O.W. Tredennick, G. Canler, and K. Chapot. Structural capacities of LNG membrane containment systems. In *Proceedings of the International Offshore and Polar Engineering Conference*, pages 107–114, 2009.

[50] J.J. Jensen. *Load and Global Response of Ships*. Elsevier, 2001.

[51] H.K. Jeong and Y.S. Yang. Strength Analysis of Mark III Cargo Containment System using Anisotropic Failure Criteria. *Journal of Advanced Research in Ocean Engineering*, 1:211–226, 2015.

[52] A. Jeschke, G.K. Pedersen, S. Vater, and J. Behrens. Depth-averaged non-hydrostatic extension for shallow water equations with quadratic vertical pressure profile: equivalence to boussinesq-type equations. *International Journal for Numerical Methods in Fluids*, 84(10):569–583, 2017.

[53] M.L. Kaminski and H. Bogaert. Full-scale sloshing impact tests- part i. *International Journal of Offshore and Polar Engineering*, 20(1):24–33, 2010.

[54] M.M. Kamra, J. Al-Salami, M. Sueyoshi, and C. Hu. Experimental study of the interaction of dambreak with a vertical cylinder. *Journal of Fluids and Structures*, 86:185 – 199, 2019.

[55] P. Kaplan and M.N. Silbert. Impact forces on platform horizontal members in the splash zone. In *Proceedings of the Annual Offshore Technology Conference*, volume 1976-May, pages 749–758, 1976.

[56] B. Kayal, A. Benoit, M. Frihat, and T. Loysel. Introduction to a structural-based sloshing assessment for membrane containment system. In *Proceedings of the International Offshore and Polar Engineering Conference*, pages 1029–1035, 2016.

[57] M. Kim, O. Hizir, O. Turan, S. Day, and A. Incecik. Estimation of added resistance and ship speed loss in a seaway. *Ocean Engineering*, 141:465–476, sep 2017.

[58] M.H. Kim, S.M. Lee, J.M. Lee, B.J. Noh, and W.S. Kim. Fatigue strength assessment of mark-iii type lng cargo containment system. *Ocean Engineering*, 37:1243–1252, 2010.

[59] W. Lafeber, L. Brosset, and H. Bogaert. Elementary loading processes (ELP) involved in breaking wave impacts: Findings from the Sloshel project. In *Proceedings of the International Offshore and Polar Engineering Conference*, pages 265–276, 2012.

[60] S. Lenci, M. Brocchini, and C. Lorenzoni. Experimetnal rotations of a pendulum on water waves. *Journal of Computational and Nonlinear Dynamics*, 7, 2012.

[61] S. Lenci and G. Rega. Experimental versus theoretical robustness of rotating solutions in a parametrically excited pendulum: A dynamical integrity perspective. *Physica D*, 240:814–824, 2011.

[62] K. Liao, C. Hu, and M. Sueyoshi. Free surface flow impacting on an elastic structure: Experiment versus numerical simulation. *Applied Ocean Research*, 50:192 – 208, 2015.

[63] M.A. Losada and J. Merino. An Energy Approach to Non-breaking Wave-induced Motion of Bottom Sediment Particles. *Coastal Engineering*, 11:159–173, 1987.

[64] C. Lugni, A. Bardazzi, O. M. Faltinsen, and G. Graziani. Hydroelastic slamming response in the evolution of a flip-through event during shallow-liquid sloshing. *Physics of Fluids*, 26, 2014.

[65] C. Lugni, M. Brocchini, and O. M. Faltinsen. Wave impact loads: The role of the flip-through. *Physics of Fluids*, 18(12), DEC 2006.

[66] C. Lugni, M. Miozzi, M. Brocchini, and O. M. Faltinsen. Evolution of the air cavity during a depressurized wave impact. I. The kinematic flow field. *Physics of Fluids*, 22(5), MAY 2010.

[67] T. Mai, C. Mai, A. Raby, and D.M. Greaves. Hydroelasticity effects on water-structure impacts. *Experiments in Fluids*, 61(9), 2020.

[68] S. Malenica, I. Ten, T. Gazzola, Z. Mravak, J. De-Lauzon, A.A. Korobkin, and Y.M. Scolan. Combined Semi-analytical And Finite Element Approach For Hydro Structure Interactions During Sloshing Impacts - "Sloshel Project". In *Proceedings of the International Conference on Offshore Mechanics and Arctic Engineering*, 2009.

[69] Sime Malenica, Louis Diebold, Sun Hong Kwon, and Dae-Seung Cho. Sloshing assessment of the LNG floating units with membrane type containment system where we are? *Marine Structures*, 56:99–116, 2017.

[70] V. Mathai, R.N. Govardhan, and V.H. Arakeri. On the impact of a concave nosed axisymmetric body on a free surface. *Applied Physics Letters*, 106(6), 2015.

[71] V. Mathai, L.A.W.M. Loeffen, T.T.K. Chan, and S. Wildeman. Dynamics of heavy and buoyant underwater pendulums. *Journal of Fluid Mechanics*, 862:348–363, 2019.

[72] X. Mei, Y. Liu, and D.K.P. Yue. On the water impact of general two-dimensional sections. *Applied Ocean Research*, 21(1):1–15, 1999.

[73] C. Mittelstedt and W. Becker. Free-Edge Effects in Composite Laminates. *Appl. Mech. Rev.*, 60:217–245, 2007.

[74] J.R. Morison, J.W. Johnson, and S.A. Schaaf. The force exerted by surface waves on piles. *Journal of Petroleum Technology*, 2, 1950.

[75] P. Navarro, S. Abrate, J. Aubry, S. Marguet, and J.-F. Ferrero. Analytical modeling of indentation of composite sandwich beam. *Compos. Struct.*, 100:79–88, 2013.

[76] J.N. Newman. *Marine Hydrodynamics*. MIT Press, 1977.

[77] M.K. Ochi. *Ocean Waves - The Stochastic Approach*. Cambridge University Press, 1998.

[78] J. K. Paik, J. M. Sohn, Y. S. Shin, and Y. S. Suh. Nonlinear structural analysis of membrane-type lng carrier cargo containment system under cargo static pressure loads at the cryogenic condition with a temperature of -163°c. *Ships and Offshore Structures*, 6:311–322, 2011.

[79] Y. Parihar, K. Doshi, J.R. Saripilli, R. Joga, and S. Dhavalikar. Strength assessment of membrane type containment system of lng carrier. In *Proceedings of the International Offshore and Polar Engineering Conference*, pages 1043–1050, 2016.

[80] D.H. Peregrine. Water-wave impact on walls. *Annu. Rev. Fluid Mech.*, 35:23–43, 2003.

[81] B. Pillon, M. Marhem, G. Leclèrce, and G. Canler. Numerical Approach For Structural Assessment of LNG Containment Systems. In *Proceedings of the International Offshore and Polar Engineering Conference*, pages 175–182, 2009.

[82] R Porter. The coupling between ocean waves and rectangular ice sheets. *Journal of Fluids and Structures*, 84:171–181, 2019.

[83] M.M. Rienecker and J.D. Fenton. A fourier approximation method for steady water waves. *J. Fluid Mech.*, 104:119–137, 1981.

[84] W. Ritz. Theorie der Transversalschwingungen einer quadratischen Platte mit freien Rändern. *Annalen der Physik*, 333:737–786, 1909.

[85] J.E. Sader, J. Cosse, D. Kim, B. Fan, and M. Gharib. Large-amplitude flapping of an inverted flag in a uniform steady flow - a vortex-induced vibration. *Journal of Fluid Mechanics*, 793:524–555, 2016.

[86] T. Sarpkaya. Force on a circular cylinder in viscous oscillatory flow at low Keulegan-Carpenter numbers. *Journal of Fluid Mechanics*, 165:61–71, 1986.

[87] S. Schreier and B. Mehl. Experimental Investigation of 3D Sloshing Effects in Thin Rectangular Tanks. In *Proceedings of the International Offshore and Polar Engineering Conference*, pages 433–439, 2012.

[88] G. Stelling and M. Zijlema. An accurate and efficient finite-difference algorithm for non-hydrostatic free-surface flow with application to wave propagation. *International Journal for Numerical Methods in Fluids*, 43:1–23, 2003.

[89] O.T. Thomsen. Analysis of local bending effects in sandwich plates with orthotropic face layers subjected to localised loads. *Composite Structures*, 25(1-4):511–520, 1993.

[90] C.V. Girija Vallabhan and Y.C. Das. Parametric Study of Beams on Elastic Foundations. *Journal of Engineering Mechanics*, 115(12):2072–2082, 1988.

[91] E. van de Bunt, J. Dekker, J. Scharnke, and F. Jaouën. Applying force panels for wave impact measurements. *Ocean Engineering*, 232, 2021.

[92] M. van der Eijk and P.R. Wellens. A compressible two-phase flow model for pressure oscillations in air entrapments following green water impact events on ships. *International Shipbuilding Progress*, pages 1–29, 2019.

[93] M. van Meerkerk, C. Poelma, B. Hofland, and J. Westerweel. Experimental investigation of wave tip variability of impacting waves. *Physics of Fluids*, 32(8), 2020.

[94] D. Van Nuffel, K.S. Vepa, I. De Baere, P. Lava, M. Kersemans, J. Degrieck, J. De Rouck, and W. Van Paepegem. A comparison between the experimental and theoretical impact pressures acting on a horizontal quasi-rigid cylinder during vertical water entry. *Ocean Engineering*, 77:42 – 54, 2014.

[95] V.Z. Vlasov and N.N. Leont'ev. *Beams, Plates and Shells on Elastic Foundations*. Israel Program for Scientific Translations, 1960.

[96] H. Wagner. Über Stoß- und Gleitvorgänge an der Oberfläche von Flüssigkeiten. *Zeitschrift für Angewandte Mathematik und Mechanik*, 12, August 1932.

[97] B. Wang and Y. Shin. Full-scale test and fe analysis of lng mk iii containment system under sloshing loads. In *Proceedings of the International Offshore and Polar Engineering Conference*, pages 121–128, 2011.

[98] J. Wang, O. M. Faltinsen, and C. Lugni. Unsteady hydrodynamic forces of solid objects vertically entering the water surface. *Physics of Fluids*, 31(2), 2019.

[99] Y. Wei, T. Abadie, A. Henry, and F. Dias. Wave interaction with an oscillating wave surge converter. part ii: Slamming. *Ocean Engineering*, 113:319–334, 2016.

[100] Y. Wei, A. Rafiee, A. Henry, and F. Dias. Wave interaction with an oscillating wave surge converter, part i: Viscous effects. *Ocean Engineering*, 104:185–203, 2015.

[101] Michael Weidenfeld and Eran Arad. Mitigating the sound of a flapping airfoil using optimal structural properties distributions. *Journal of Sound and Vibration*, 432:235–248, 2018.

[102] P.R. Wellens and R.W. Bos. Experimental data for a wet-and-dry pendulum suspended in monochromatic waves. 4TU.ResearchData, 2020.

[103] P.R. Wellens and R.W. Bos. Experimental data for a wet-and-dry pendulum in breaking waves. 4TU.ResearchData, 2021.

[104] Y. Yamazaki, Z. Kowalik, and K.F. Cheung. Depth-integrated, non-hydrostatic model for wave breaking and run-up. *Int. J. Numer. Meth. Fluids*, 61:473 – 497, 2009.

[105] Y.L. Young, T. Wright, H. Yoon, and C.M. Harwood. Dynamic hydroelastic response of a surface-piercing strut in waves and ventilated flows. *Journal of Fluids and Structures*, 94:102899, 2020.

[106] Y. Zhang and D. Wan. Mps-fem coupled method for sloshing flows in an elastic tank. *Ocean Engineering*, 152:416 – 427, 2018.

[107] R. Zhao and O. Faltinsen. Water entry of two-dimensional bodies. *J. Fluid. Mech.*, 246:593–612, 1993.

[108] S. Zheng and Y. Zhang. Analysis for wave power capture capacity of two interconnected floats in regular waves. *Journal of Fluids and Structures*, 75:158–173, 2017.

Acknowledgements

For me, the success of this work has been for a large part due to the people I shared and share my work and life with. Their ongoing support, patience and trust gave me confidence and motivation that I needed to finish this work. I have many people to thank for many reasons, I apologize in advance for any omission.

First I want to thank my promotor Mirek, for working with me and giving me the opportunity to pursue a PhD at Delft University of Technology. You always let me try my own ideas and helped me defend my proposals when necessary, even though I was very stubborn at times. Henk, I learned a lot from you as copromotor and colleague. Seeing you working tirelessly and without losing track of any detail is something I admire in you. From office-roommate to copromotor, I literally worked closely with Peter. You gave your honest feedback on anything, at any time, even on the shortest notice, that helped me to make big steps.

The project SLING, of which this PhD is a part, was financed by NWO, the Dutch Organization for Scientific Research. Co-financing was done by many stakeholders in the LNG community, as mentioned on the title page, yet I want to highlight some of the project members that stood out to me. First Hannes, I am glad to have learned so much from you, first during my graduation at Marin and later during SLING. Second Laurent, Louis, Sime, thank you for many good discussions we had during and next to the SLING meetings. Finally I want to thank FEMTO for their kind cooperation.

And of course the other PhD candidates in SLING (the Sultans of SLING): Yous, Ronald, Rien, Utkarsh, Wout. Mike, I am glad to have had that much coffee together, and have someone in the same boat that understands the challenges and opportunities.

All ups and downs were first vented to my office-roommates. Joost, thanks for the philosophical discussions on mechanics, I hope we can pick that up again when dust settles down. Gabriele, lets keep up our diner tradition, together with good wine and Italian card games (that for some reason keep getting new rules just when I start winning).

Other colleagues I should not forget are Martin, Marco, Hugo, Pooria, Carey,

Henk, Bart, colleagues from the towing tank, secretaries, many more, thanks for great things: SHS colloquia, lunch breaks, rants about what is right and wrong in the university and the rest of the world. And I should also thank the students I worked with: Floriaan, Renée, Jochem, the BSc groups, I hope you learned as much from me as I learned from you. Also my 'new' colleagues Alex, Laura, Miranti, Robert, Roderik, thank you for your continued support. Lode, thanks for keeping me safe from bears and parasites, in and out of Japan.

Besides doing a PhD I also had (and have!) a personal life, and I was (am) happy to have great friends by my side. Tobias, Max, Martijn, John, Vincent, I'm always glad to meet you all and share thoughts, even though the intervals are sometimes too long.

I want to thank my parents Johan and Marjolijn, as well as my sister Alinda. You gave me a stable and loving family with an appetite for good food and great discussions. I cherish the memories of all holidays, hiking trips, museum visits, and riding the motorbike.

And, at the end of 2008, in my last year of secondary education, I met Tamara. Long story short, I am very grateful to have you in my life and feel welcome in your family. We complement each other, and I feel our love is still getting stronger by the day. I am also very thankful for Veerle and Karlijn, our two daughters, for all the joy you bring. Our family is the most important things in my world, all other things are small.